



A SEARCH FOR ULTRA HIGH ENERGY GAMMA
RAY EMISSION FROM BINARY
X-RAY SYSTEMS

*A Thesis submitted to The University of
Adelaide for the Degree of
Doctor of Philosophy*

by

Philip Gregory Edwards BSc (Hons)

March 1988

FOR MY PARENTS

This thesis contains neither material which has been accepted for the award of any other degree or diploma, nor, to the best of the author's knowledge and belief any material previously published or written by any other person, except where due reference is made.

Signed:

P.G. Edwards

ACKNOWLEDGEMENTS

iv

SUMMARY

v

CHAPTER 1

COSMIC RAYS AND GAMMA-RAYS

1.1	INTRODUCTION	1-1
1.2	COSMIC RAYS	1-2
1.2.1	HISTORY	1-2
1.2.2	ENERGY SPECTRUM	1-4
1.2.3	COMPOSITION	1-8
1.2.4	ANISOTROPY	1-11
1.3	GAMMA-RAY ASTRONOMY	1-13
1.3.1	HISTORY	1-13
1.3.2	ULTRA-HIGH-ENERGY GAMMA-RAY ASTRONOMY	1-17
1.4	OVERVIEW	1-19

CHAPTER 2

EXTENSIVE AIR SHOWERS

2.1	INTRODUCTION	2-1
2.1.1	THE HADRON COMPONENT	2-1
2.1.2	THE MUON COMPONENT	2-7
2.1.3	THE ELECTROMAGNETIC (EM) COMPONENT	2-9
2.2		
2.2.1	MUON CONTENT	2-12
2.2.2	SHOWER AGE	2-17
2.2.3	ANGULAR RESOLUTION	2-19
2.2.4	SOURCE PERIODICITY	2-23
2.3	SUMMARY	2-24

CHAPTER 3

THE BUCKLAND PARK AIR SHOWER ARRAY

3.1	THE AIR SHOWER ARRAY	3-1
3.1.1	THE DETECTORS	3-1
3.1.2	THE FAST-TIMING SYSTEM	3-4
3.1.3	THE DENSITY MEASURING SYSTEM	3-5
3.1.4	COLLECTION	3-8
3.2	DIRECTIONAL ANALYSIS	3-10
3.2.1	TIMING DIFFERENCES	3-11
3.2.2	UNPHYSICAL TIMES	3-15

CHAPTER 4

BEHAVIOUR OF THE BUCKLAND PARK ARRAY

4.1	INTRODUCTION	4-1
4.2	THE ZENITH ANGLE DISTRIBUTION	4-1
4.3	THE AZIMUTH ANGLE DISTRIBUTION	4-3
4.4	ARRAY EXPOSURE IN SIDEREAL TIME	4-4
4.5	THE NUMBER OF FAST-TIMING DETECTORS TRIGGERED	4-4
4.6	GOODNESS OF FIT DISTRIBUTION	4-7
4.7	TIMING OFFSET DISTRIBUTION	4-8
4.8	ANGULAR RESOLUTION	4-9

CHAPTER 5

SEARCH FOR ULTRA-HIGH-ENERGY GAMMA-RAY EMISSION FROM BINARY X-RAY SOURCES

5.1	BINARY X-RAY SYSTEMS	5-1
5.2	SEARCH FOR ULTRA-HIGH-ENERGY GAMMA-RAY EMISSION FROM BINARY X-RAY SYSTEMS	5-4
5.2.1	VELA X-1	5-4
5.2.2	LMC X-4	5-8
5.2.3	CIRCINUS X-1	5-10
5.2.4	CENTAURUS X-3	5-12
5.2.5	SCORPIUS X-1	5-14
5.2.6	1822-37.1	5-15
5.3	SUMMARY	5-17
6.1	CONCLUSION	6-1
7.1	APPENDIX A	7-1
8.1	REFERENCES	8-1

ACKNOWLEDGEMENTS

It is a pleasure to be able to acknowledge the many people who have helped to make my candidature as rewarding as it has been.

I wish to thank: my supervisor, Dr. John Patterson, for his encouragement and assistance; Dr. Roger Clay, who has provided invaluable help in the maintenance of the Buckland Park array, and provided supervision during the absence of Dr. Patterson; Dr. Ray Protheroe, whose guidance in the theoretical aspects of the project is gratefully acknowledged; Professor John Prescott and Dr. Alan Gregory for their encouragement; Dr. Bruce Dawson, who taught me how to drive the Buckland Park array and helped to keep it running; Claire Corani and Dominic Ciampa for their significant contributions in the development of the analysis programs, and particularly Dominic for helpful discussions regarding the timing differences; Stephen Elton for statistical advice and helpful references; Neville Wild and John Pezy for their technical assistance; Ruth Fazakerley for helping to organise my mass of computer printouts; and Christine Collins for her interest.

Roger Clay, Dominic Ciampa, Stephen Elton, John Patterson and Damian Murphy are all thanked for helping with the routine tape-changing at Buckland Park. The many friends I have made in the Physics Department will not be forgotten and are thanked for just being there. Members of the C.R.G.G.C. (Int.) are respectfully acknowledged for their assistance. Last, but by no means least, I wish to thank Jill Allen for typing this thesis, and to say "efkaristo" to Argyro Magoulianos for her Greek lessons.

SUMMARY

Cosmic rays have been studied for over seventy-five years, however the source of these high-energy particles until quite recently has remained a mystery. With the discovery of ultra-high-energy gamma-rays from the Binary X-ray source Cygnus X-3 in 1983, ultra-high-energy gamma-ray astronomy was born, and immediately provided a vital key to the puzzle of the origin of cosmic rays. Ultra-high-energy gamma-rays are vastly out-numbered by cosmic rays, and the extensive air showers they both produce in interactions with the earth's atmosphere appear to be quite similar. These facts conspire to make ultra-high-energy gamma-ray astronomy a difficult task.

In the introductory chapter of this thesis, the history and important properties of the cosmic-ray flux are reviewed, and the history of gamma-ray astronomy is outlined in Chapter 2. A detailed description of the components of a cosmic ray shower is given. This is followed by a discussion of the various proposed techniques for differentiating cosmic ray and ultra-high-energy gamma-ray-initiated showers, or at least to improve the "signal to noise" ratio. Chapter 3 describes the recently upgraded Buckland Park Air Shower Array. The components of the array and the data collection and analysis procedures are comprehensively described. The Buckland Park Array has been used to collect air shower data over a two year period. The recent additions to the array have lowered the energy threshold and, as a result, increased

the data collection rate. This allows cosmic rays and ultra-high-energy gamma-rays to be studied at lower energies, but has also made the data analysis a bottleneck in the system. The data have been analysed to find the arrival direction of the incident showers, so that showers from selected regions of the sky can be analysed in detail. The complete set of directions is checked in Chapter 4 to ensure it displays the expected characteristics.

Chapter 5 begins with a short description of binary X-ray sources. Six such sources, all potential sources of ultra-high-energy gamma-rays are then examined for statistically significant evidence of emission. No conclusive evidence is found for any of the six sources considered. Upper limits on the flux of ultra-high-energy gamma-rays are obtained for each source. The concluding chapter summarises and discusses the results, and makes suggestions for future work.

"RESEARCH: the process of going up alleys to see
if they're blind"

- Barstow Bates

"SCIENCE: is always wrong; it never solves a
problem without creating ten more".

- George Bernard Shaw

CHAPTER 1

COSMIC RAYS AND GAMMA-RAYS

1.1 INTRODUCTION

Ultra-high-energy (UHE) gamma-ray astronomy and cosmic ray physics are intimately linked. UHE gamma-rays are dwarfed in number by the isotropic cosmic ray background, and it is only with the judicious use of techniques discussed in Chapter 2 that they can be detected. However, the detection of UHE gamma-rays has provided the first direct evidence for the association of particular astronomical objects with the acceleration of charged cosmic ray particles to ultra high energies.

Cosmic rays have been successfully used in the past in the discovery and study of elementary particles. However, until recently, the origin and means by which nature accelerates these particles to such energies has been largely a matter for conjecture. Cosmic rays constitute almost one third of the energy density of the interstellar medium (ISM), and UHE gamma-rays therefore provide us with an unparalleled opportunity to gain a better understanding of this astrophysically important phenomenon.

In this chapter a brief history of the development of cosmic ray physics is given, and the current knowledge of the properties of the cosmic ray flux is reviewed. The same procedure is then adopted for gamma-ray astronomy, and in particular UHE gamma-ray astronomy.

1.2 COSMIC RAYS

1.2.1 HISTORY

On the 7th of August, 1912, Viktor Hess embarked upon a balloon flight to investigate the variation with height of the ionizing radiation found to be present in the atmosphere. After a decrease in intensity for the first 700 m increase in altitude, Hess found that the intensity of the radiation increased rapidly with height. He concluded there was an extraterrestrial source for this penetrating radiation coming through the atmosphere (Hess 1912). Such radiation was first termed "cosmic radiation" by Millikan in 1926.

Three types of ionizing radiation were known at the time; α , β and γ radiation, and the cosmic radiation was initially interpreted as consisting of highly penetrating gamma-rays. It was assumed that the (neutral) gamma-rays gave up most of their energy in elastic collisions with atomic electrons, resulting in the detected ionization. Following calculations by Störmer on the trajectories of charged particles in the Earth's magnetic

field, Clay (1927) observed a decrease in the cosmic ray intensity as he neared the equator. This was evidence that cosmic rays were charged particles. Further observations by Johnson (1933) and Alvarez and Compton (1933) showed an excess of cosmic rays from the west of the zenith compared to the east, a result showing that the majority of the cosmic rays were positively charged. This was in contrast to the particles observed in cloud chamber studies, which were predominantly negative.

Cloud chamber studies performed by Skobelzyn (1929) showed that cosmic ray particles occurred in individual swarms or showers. Further cloud chamber studies by Anderson (1933) and Blackett and Occhialini (1933) revealed that these showers contained both positive and negative electrons. Rossi (1933) confirmed the existence of showers by observing coincidences between three Geiger-Müller counters arranged in a triangle so that a single particle could not cause a coincidence.

In 1938 it was established by Auger et al. (1938) and by Kolhörster et al. (1938) and co-workers that there existed extensive air showers (EAS) at ground level with lateral extents of up to 300 m. This indicated a primary energy of the order of 10^{15} eV, which was considerably greater than had previously been considered possible. The energy spectrum of cosmic rays was later found to extend beyond 10^{20} eV with the observations of giant EAS by Linsley (1963).

REVIEW OF PROPERTIES OF THE COSMIC RAY FLUX

The three most fundamental measurements that can be made of the cosmic ray flux are those of its energy spectrum, mass composition and isotropy. Each of these is briefly reviewed. This section is based largely on recent reviews by Watson (1984), Hillas (1984b), Clay (1985a) and Watson (1985).

1.2.2 ENERGY SPECTRUM

The cosmic ray energy spectrum (illustrated in its integral form in Figure 1.1) is known to within $\pm 20\%$ from energies of $\sim 10^{12}$ eV up to $\sim 10^{19}$ eV (with the possible exception of the "knee"). The most prominent feature of the spectrum is a change of slope at $\sim 5 \times 10^{15}$ eV. Known as the "knee", this feature is well-established, but not yet well understood. For the purposes of this discussion, the spectrum will be divided into four regions:

(i) $10^{12} - 10^{14}$ eV

The spectrum is known most accurately at these energies. The high flux allows direct measurement of primary cosmic rays to be made by satellite, balloon and aircraft-borne detectors. For this reason the mass composition is also best defined in this energy range. The energy per nucleus spectrum at these energies has a differential slope of ~ -2.7 .

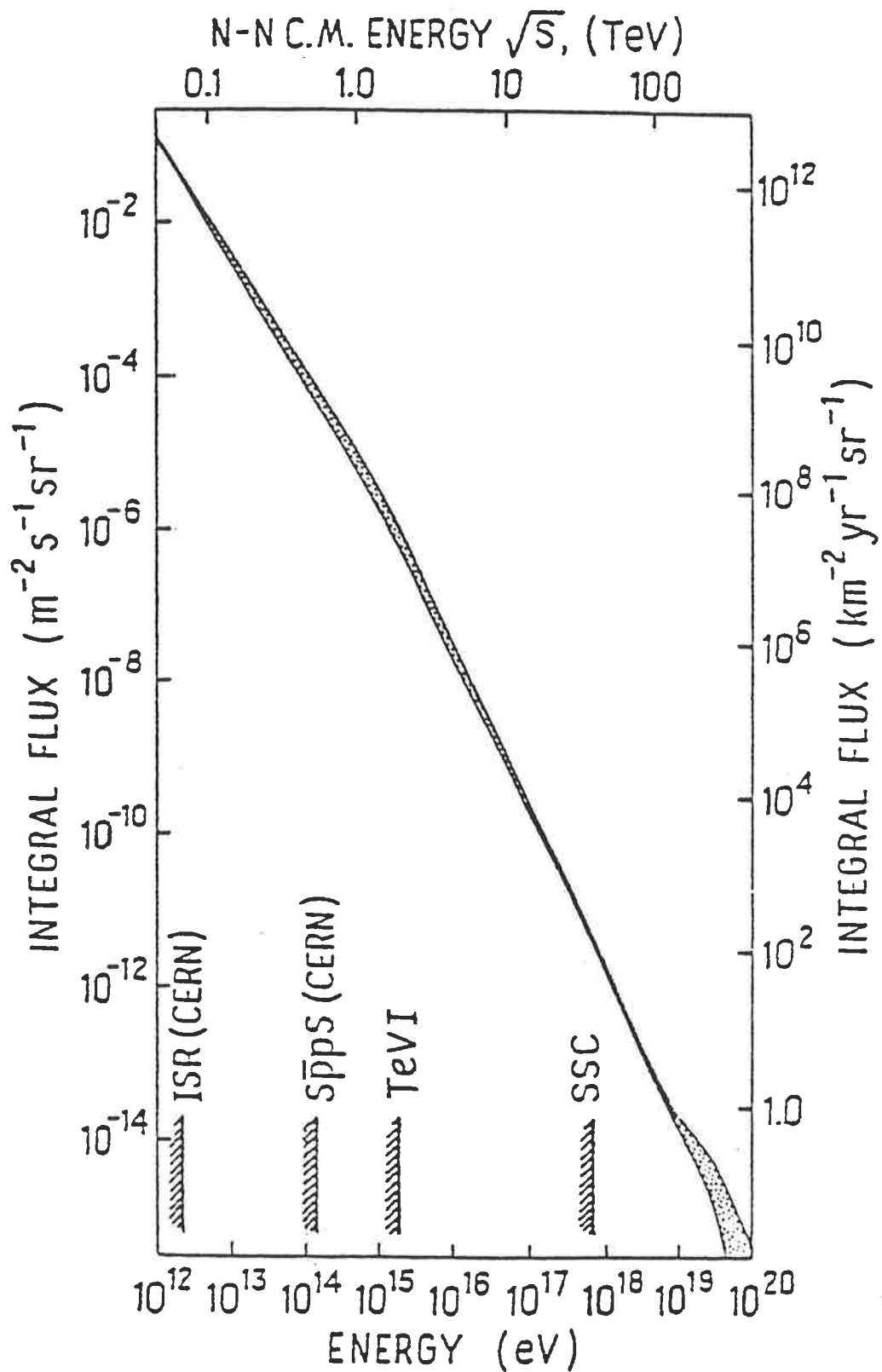


Figure 1.1

The flux of all primary cosmic rays at the top of the atmosphere, shown as an integral spectrum. The stippled regions indicate experimental uncertainties. The maximum attainable energies of existing and proposed accelerators are also indicated. (From Jones (1985))

(ii) $10^{14} - 10^{17}$ eV

Studies at these energies are performed by measuring the EAS produced by the primary cosmic rays. Fluctuations in shower development, particularly for lower energy primaries, make absolute measurements of the cosmic ray flux difficult. Downward fluctuating (i.e. later developing) showers are preferentially detected, and this bias must be taken into account when deriving the spectrum at these energies. Nevertheless, the "knee" in the spectrum is a well attested reality.

An early explanation for the knee was that it resulted from a rigidity dependent leakage from a local confinement region (Peters 1961). Magnetic rigidity, R , is defined:

$$R = \frac{pc}{Ze}$$

where p = momentum

c = velocity of light

Ze = charge on nucleus (Z = atomic number)

and is usually expressed in units of GV (Giga Volts). The local confinement region is assumed to be the galactic magnetic field. Cosmic rays spiral along galactic magnetic field lines with a radius of curvature proportional to their rigidity. With increasing rigidity, this "Larmor" radius increases until it is greater than the size of the confinement region and the particle escapes. These models are known as "leaky box" models. The assumed rigidity dependence for the knee implies a knee for each species at

the same rigidity, but at an energy $E \propto Z$. This is illustrated in Figure 1.2. Protons are lost first from the flux at an energy E_k , say, followed by progressively heavier elements with the iron knee at $26 E_k$. Such a gradual leakage does not appear to be observed in practice.

An alternative explanation for the origin of the knee was that it was caused by particles accelerated by pulsars. Early models proposed that pulsars may be able to accelerate particles with energies up to 10^{16} eV (e.g. Ostriker and Gunn 1969). It was postulated that the extrapolation of that flat pulsar energy spectrum at $E < 10^{14}$ eV may result in a dominance of particles accelerated by pulsars at the knee (Karakula et al. 1974, Strong et al. 1974). The status of this model is uncertain in the light of the detection of UHE gamma-rays with energies $\lesssim 10^{16}$ eV (and therefore the assumed acceleration by pulsars of particles up to energies of at least $\sim 10^{17}$ eV).

(iii) $10^{17} - 10^{19}$ eV

There is quite good agreement between the results of groups working with arrays able to measure fluxes at these energies with reasonable rates (e.g. Linsley 1983, Baltrusaitis et al. 1985, Winn et al. 1986). The spectrum in this range has a differential slope of ~ -3.1 , and appears to be featureless.

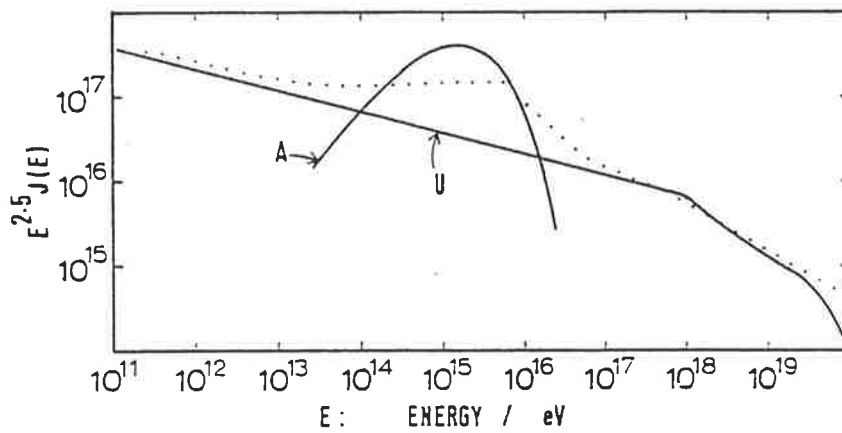
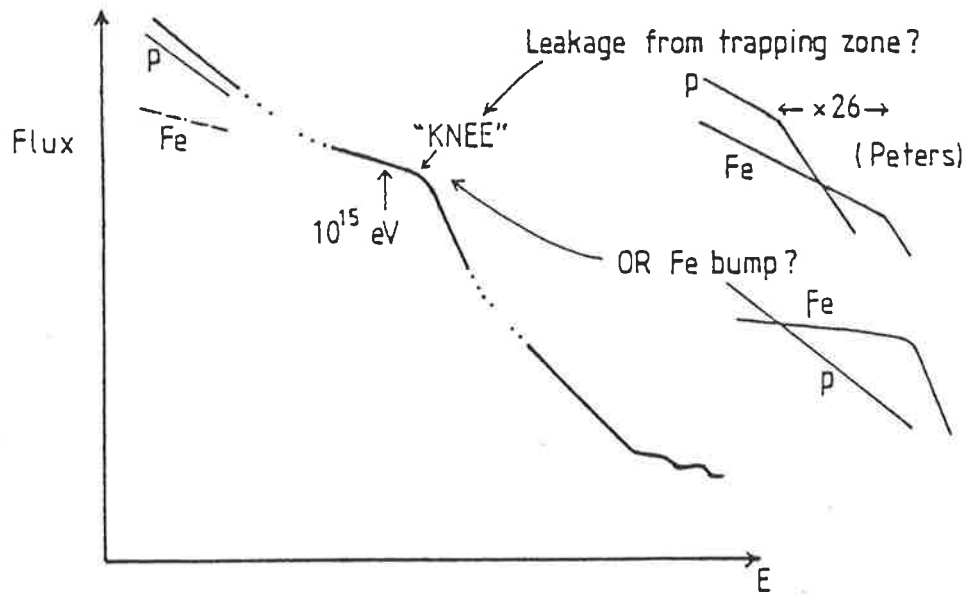


Figure 1.2. Various models for the knee in the cosmic ray spectrum. Upper diagram contrasts the rigidity dependent escape of Peters (1961) with an iron "bump" model. (From Hillas (1981)). Lower diagram illustrates the superposition of a pulsar accelerated component, labelled A, on the spectrum, labelled U. The dotted line is an experimentally determined spectrum. (From Hillas (1975)).

(iv) $> 10^{19}$ eV

This is a region of great interest. It was realised that the discovery of the 2.7 K microwave background (or relic) radiation would imply a cut-off in the cosmic ray spectrum if the sources of cosmic rays of these energies were at distances greater than ~ 50 Mpc (Greisen 1966, Zatsepin and Kuzmin 1966). The cut-off at $\sim 4 \times 10^{19}$ eV would arise from the interactions of particles greater than this with 2.7 K photons.

The Haverah Park, Sydney and Volcano Ranch groups claim that the spectrum is flatter above $\sim 2 \times 10^{19}$ eV than below, the "ankle" of the spectrum (Bower et al. 1981, Winn et al. 1986). This would imply that the sources of these cosmic rays lie within 50 Mpc. However, the Yakutsk group find some evidence for a steepening of the spectrum above $\sim 4 \times 10^{19}$ eV (Krasilnikov et al. 1983). The Fly's Eye group also find a cut-off, at 7×10^{19} eV (Baltrusaitis et al. 1985), although their evidence may not be as statistically significant as they claim (e.g. Linsley 1985).

Hill and Schramm (1984) predict a spectral enhancement at $\sim 6 \times 10^{19}$ eV preceded by a dip at $\sim 10^{19}$ eV. They find the dominant effects in the long range propagation and production of cosmic rays at these energies are photopion production, electron-positron pair production and

redshifting of energy. The enhancement at $\sim 6 \times 10^{19}$ eV results from the pile-up of energy-degraded nucleons while the dip at $\sim 10^{19}$ eV is due to the combined efforts of the pile-up and pair-production.

Hill and Schramm use Haverah Park data as supporting evidence, and, although the Fly's Eye group claim agreement with those data, the result requires further confirmation.

1.2.3 COMPOSITION

As mentioned in the previous section, the mass composition of cosmic rays is very well determined at low energies. Figure 1.3 shows the cosmic ray nuclear abundances compared to solar system abundances for elements with $Z < 28$. The mass composition extends beyond $Z = 90$ (Fowler et al. 1987) but nuclei with $Z > 30$ are $\geq 10^{-4}$ less abundant than iron.

As Figure 1.3 illustrates, the relative abundances agree well with the solar system abundances, with two exceptions. In particular, the relative stability of even as compared to odd numbered atomic nuclei with $Z > 30$ have abundances less than 10^{-4} of that of iron.

The first exception to this general agreement is that hydrogen and helium are relatively under-abundant in the cosmic ray beam. This feature is discussed in the review by Meyer (1985). The second exception to the general agreement are the light elements lithium, beryllium and boron, and also the group of elements just below iron, all of which are relatively over-

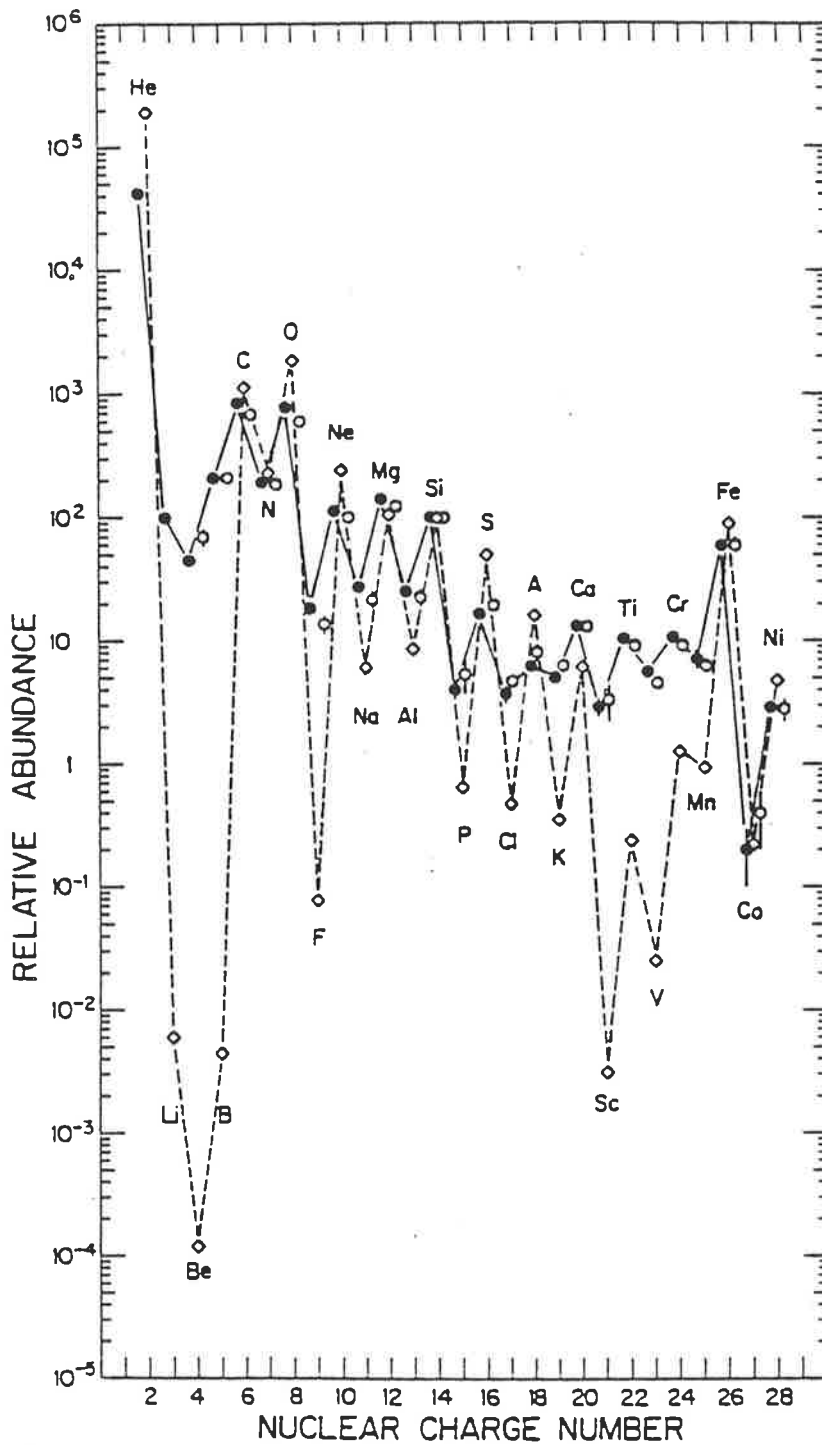


Figure 1.3. Cosmic ray nuclear abundances measured at the Earth compared to solar system abundances. All abundances are relative to Silicon, which is assigned a relative abundance of 100. Filled circles correspond to lower energy data (70-280 MeV/nucleon), open circles to a compilation of higher energy data (1-2 GeV/nucleon) and diamonds to solar system abundances. (From Simpson (1982)).

abundant. These over-abundances are believed to result from the spallation of elements of higher atomic number in interactions with the inter-stellar medium. This being the case, the relative abundances of these elements allow an estimate to be made of the amount of matter traversed by cosmic rays between their acceleration and their arrival at Earth. One estimate of this matter path length, λ , which is found to decrease with energy (and thus rigidity) is given by

$$\lambda = 7.9 \pm 0.7 \text{ g cm}^{-2} \quad 3 < R \leq 5.5 \text{ GV}$$

$$\lambda = (22 \pm 2)R^{-0.60 \pm 0.04} \text{ g cm}^{-2} \quad R > 5.5 \text{ GV}$$

(Engelman et al. 1985). This matter path length is equivalent to the escape length of leaky box models of cosmic ray propagation.

A knowledge of the path length enables the effects due to spallation to be removed from the observed abundances and a cosmic ray source abundance to be calculated (e.g. Meyer 1985). This can then be compared with local galactic or solar system abundances. As illustrated in Figure 1.4, the differences between the two show a strong correlation with first ionization potential. A similar trend is found for energetic solar particles, a result with important implications for models of cosmic ray acceleration.

The ratio of unstable nuclear isotopes to their stable counterparts allows the age of the cosmic ray flux to be determined. The ratio of ^{10}Be , which has a half life of 1.5×10^6 yr, to stable ^9Be has been used to derive a lower limit to this age of $10\text{--}20 \times 10^6$ yr (Simpson 1983). This age is analogous to the confinement time of leaky box models.

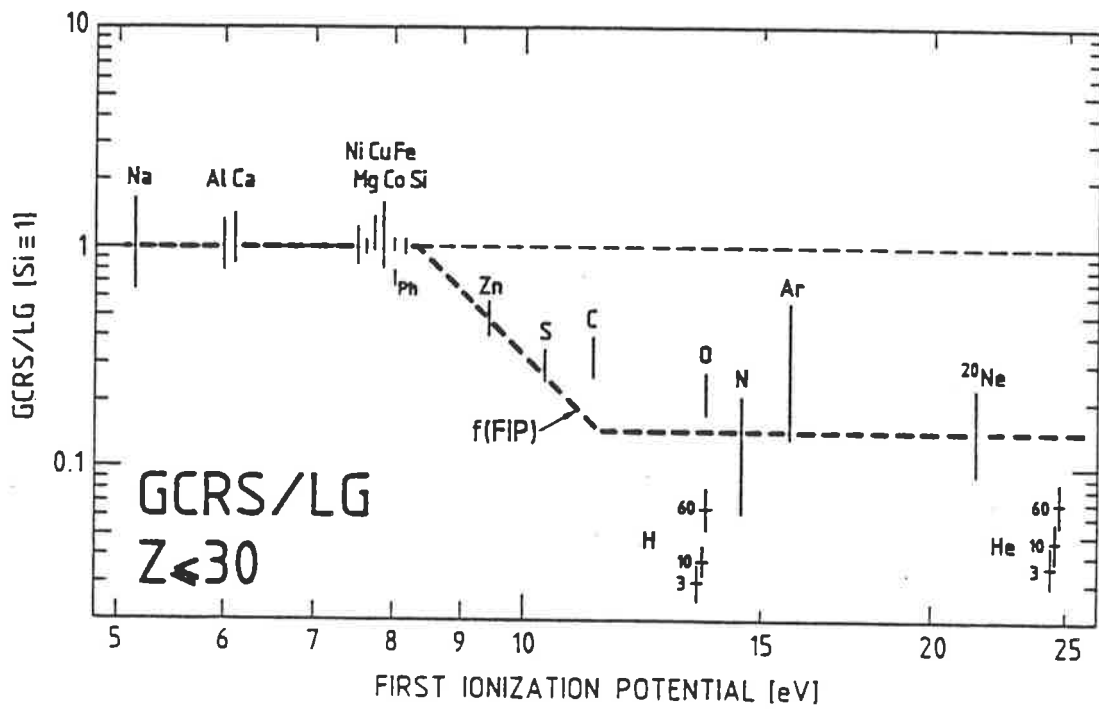


Figure 1.4. Galactic cosmic ray source (GCRS) to local galactic (LG) ratios plotted against the atomic first ionization potential. Hydrogen and Helium ratios are shown for measurements at 3, 10 and 60 GeV/nucleon. The bold dashed line corresponds to an adopted function of the correlation between the GCRS/LG ratio and the first ionization potential (From Meyer (1985)).

The composition at higher energies is probably the least well defined property of cosmic radiation. The composition in the region of the knee, in particular, is the subject of considerable debate. Leaky box models, which propose a rigidity dependent escape of cosmic rays from the galaxy, predict a proton knee at $\sim 2 \times 10^{14}$ eV and subsequent heavier element dominance, with an iron knee at $\sim 5 \times 10^{15}$ eV (see Figure 1.2). However, no early proton knee has been observed. Hillas finds that a best fit to shower size data is obtained if the iron knee occurs at $\sim 2 \times 10^{15}$ eV and the proton knee at a higher energy, $\sim 5 \times 10^{15}$ eV (see Watson 1985). If the proton knee is due to rigidity dependent leakage, this would then imply that the iron knee results from a different mechanism, or may be intrinsic to the source.

Measurements of the rate of change (and of fluctuations) in the depth of maximum of EAS, of muon multiplicities and lateral distributions, and of delayed hadrons in EAS have all been used to draw a variety of conclusions about the composition in the region near the knee. These conclusions range between the extremes of iron dominance at the knee, to proton dominance. They also include models of constant composition from 10^{12} eV to 10^{19} eV. However, there is general agreement that the composition beyond $\sim 10^{17}$ eV is not dominated by iron. Experimental results support a proton component of at least 40% at these energies (e.g. Watson 1985, Clay 1985a, Armitage et al. 1987).

1.2.4 ANISOTROPY

The Larmor radius, r_L , of a relativistic particle of charge Z in a magnetic field is

$$r_L = \frac{1.08 E}{Z B}$$

where E is the energy in units of 10^{15} eV

B is the magnetic field strength in microgauss

r_L is in parsecs

Measurements of the magnetic field in the galactic plane have been made using a variety of methods (e.g. Longair 1981 Chapter 17), which reveal a large scale longitudinal field of $\sim 2-3 \mu\text{G}$.

Superimposed upon this large scale field are irregularities with strengths of the same order and with dimensions of several hundred parsecs. The structure and extent of the magnetic field in the galactic halo is less well defined. It is clear, however, that over their long lifetime the trajectories of all but the highest energy cosmic rays will be severely distorted by magnetic fields, resulting in the almost isotropic arrival of cosmic rays at Earth.

The degree of anisotropy, δ , is defined by

$$\delta = \frac{I_{\max} - I_{\min}}{I_{\max} + I_{\min}}$$

where I_{\max} and I_{\min} are the maximum and minimum cosmic ray intensity across the sky. The conventional method of anisotropy analysis is to determine the first Fourier harmonic amplitude and

phase in right ascension. The amplitude is defined:

$$r = \sqrt{a^2 + b^2}$$

$$\text{where } a = \frac{2}{N} \sum_i^N \cos \psi_i$$

$$b = \frac{2}{N} \sum_i^N \sin \psi_i$$

where N is the number of directions considered.

The phase is defined

$$\psi = \arctan \left(\frac{b}{a} \right)$$

$$\text{where } \frac{3\pi}{2} < \psi < \frac{\pi}{2} \quad \text{if } a > 0$$

$$0 < \psi < \pi \quad \text{if } b > 0.$$

Figure 1.5 illustrates recent experimental results. At low energies the anisotropy is small and has constant phase. Both the amplitude and phase change at $E \sim 10^{14}$ eV, seemingly before the knee of the energy spectrum. Above 10^{17} eV the phase varies rapidly with energy, although with good agreement between experiments.

The seemingly good agreement in amplitude shown in Figure 1.5 is questioned by Clay (1987), who reviews results of cosmic ray anisotropy above 10^{15} eV. Clay finds there is no evidence for any clear anisotropy amplitude, but notes that the phase shows a surprising, although not compelling, consistency.

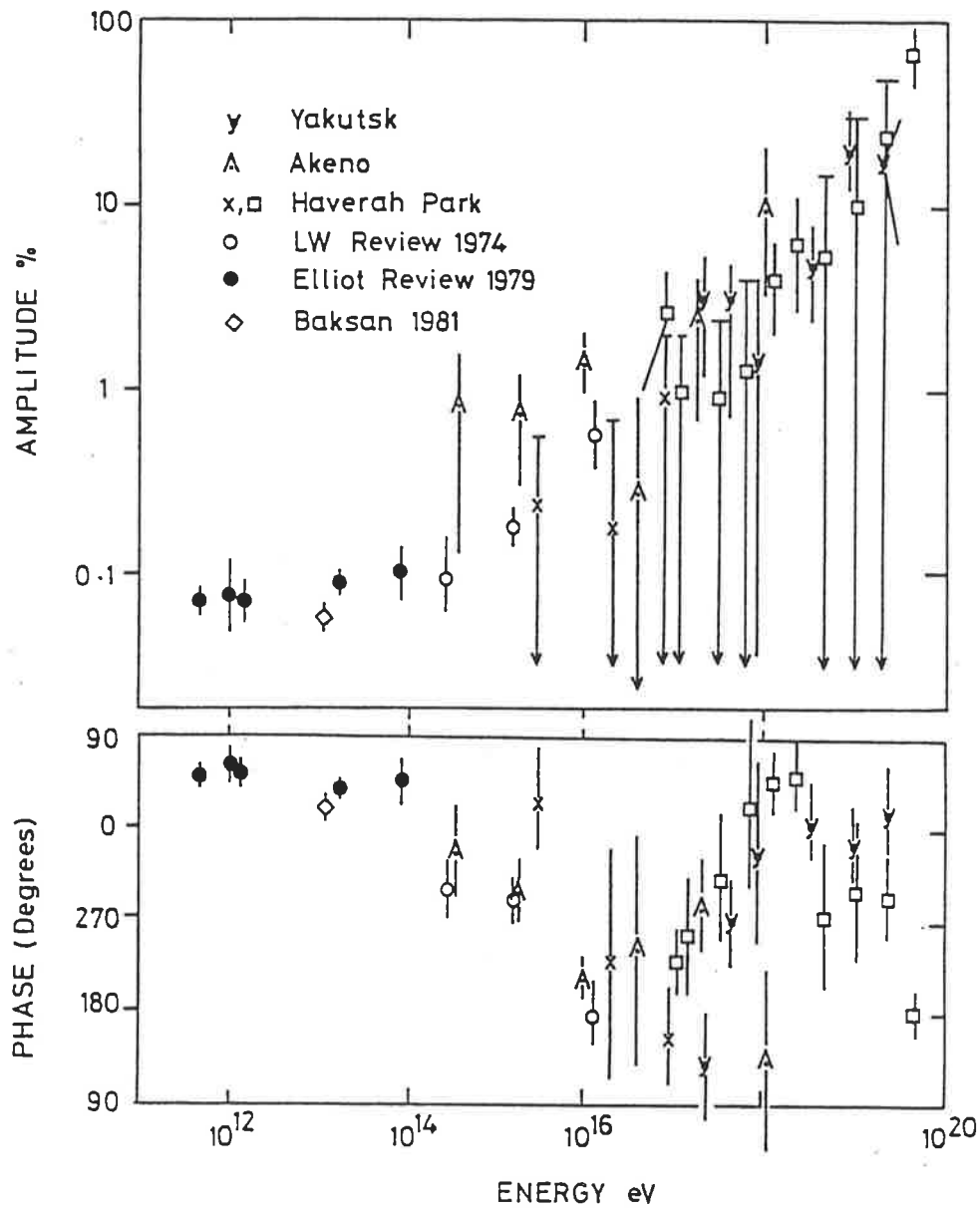


Figure 1.5. A summary of results from anisotropy analyses. The amplitude of the first Fourier component is small at low energies and increases with increasing energy. The variation of phase (i.e. the right ascension of the maximum of the first Fourier component) with energy is also shown. (From Watson (1984)).

Northern Hemisphere results for $E < 10^{19}$ eV appear to show a high-energy intensity gradient with a deficit of flux from northern galactic latitudes (Astley et al. 1981, Efimov et al. 1983). This has been questioned by Wdowczyk and Wolfendale (1984), who claim that there is evidence for an enhancement from the general direction of the galactic plane.

If, as the evidence suggests, protons do make a significant contribution to the flux at energies above 10^{19} eV they must be of extragalactic origin as their Larmor radii are much greater than the size of the galaxy (see Figure 1.6). Support for this conclusion is found in the observation that no clustering is seen at these energies in the region of the galactic plane (Cunningham et al. 1983). Some results suggest a possible rather broad excess in the general direction of the centre of the Virgo cluster 15 - 20 Mpc away (Efimov et al. 1983).

1.3 GAMMA-RAY ASTRONOMY

1.3.1 HISTORY

Prior to World War II, all astronomy had been conducted at optical wavelengths, and it was only after 1945 (and due mainly to technological advances made during that war) that other wavelength bands were opened. Radio and x-ray observations revealed energetic processes invisible at optical wavelengths. It was

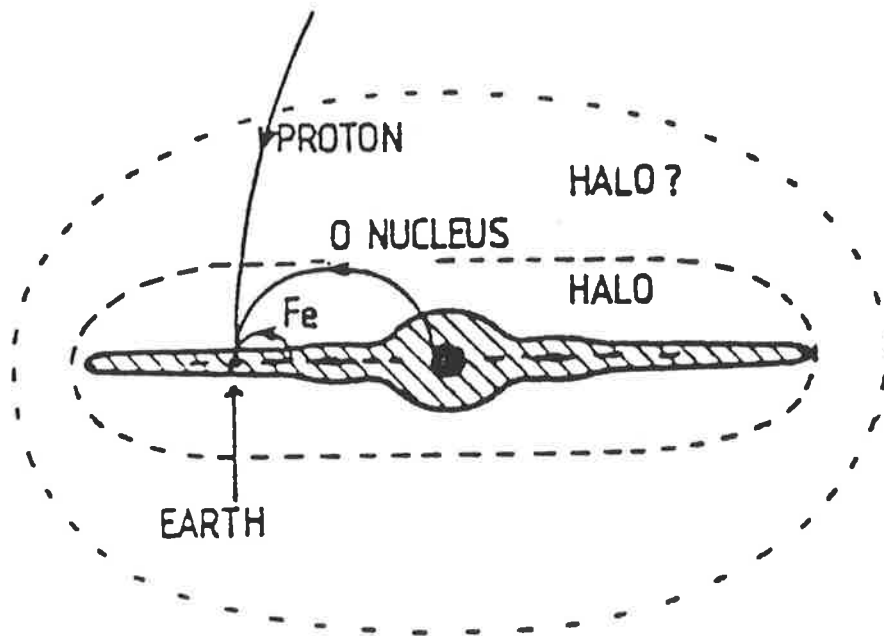


Figure 1.6. The paths of 7×10^{19} eV cosmic ray nuclei assuming a $2\mu\text{G}$ magnetic field. Only if the magnetic halo of the galaxy extended to several kiloparsecs and all particles at these energies were highly charged nuclei could a galactic origin be considered. (From Hillas (1984b)).

realised that gamma-rays could travel unscattered and unabsorbed over galactic distances and would thus allow the direct observation of energetic non-thermal processes. Early predictions of gamma-ray fluxes (e.g. Morrison 1958) proved to be optimistic however. This, coupled with the discovery of an extremely bright x-ray source, Sco X-1, resulted in x-ray astronomy developing more rapidly than gamma-ray astronomy.

Although able to travel large distances through the interstellar medium, gamma-rays are unable to penetrate the Earth's atmosphere. High energy (\sim MeV) gamma-rays were first detected by Kraushaar et al. (1965) using the Explorer II satellite, and there have been many satellite and balloon launches made since. The majority of results however have come from the SAS-II and COS-B satellite experiments.

The "small astronomical satellite", SAS-II, was launched on November 15, 1972 and was in operation for seven months. Over 8,000 photons with $E > 35$ MeV were recorded with an angular resolution of a few degrees. These data revealed the large-scale galactic gamma-ray distribution, and also several point sources, including the Vela pulsar, the Crab pulsar, Cyg X-3 and γ 195+5 (Geminga) (Hartman et al. 1979). A general concentration of flux in the galactic plane was observed, with a small diffuse flux at high galactic latitudes assumed to be due to an isotropic extragalactic component.

The COS-B satellite was launched on August 9, 1975 and remained operational until April 1982. Approximately 10^5 gamma-rays with $E > 50$ MeV were recorded over this 6½ year period. Long observation times for individual regions of sky provided good statistics, and allowed higher energy observations than SAS-II. The second COS-B catalogue (Swanenburg et al. 1981) reports the position and flux of 25 gamma-ray sources, and represents the most extensive catalogue at ~ MeV energies. It is interesting to note that Cyg X-3 was not seen by COS-B.

At higher energies, the flux of gamma-rays is too small to be measured at reasonable rates by satellite-borne detectors, necessitating the use of indirect techniques. The atmospheric Cerenkov technique has been successfully used in the energy range 10^{11} - 10^{14} eV. Cerenkov radiation is produced when a charged particle travels through a dielectric medium with a velocity greater than the speed of light in the medium. Cerenkov radiation is emitted in a well-defined cone centred on the direction of the emitting particle, and has a frequency distribution which peaks towards the UV. The visible and near-UV transparency of the atmosphere allows Cerenkov light from throughout the passage of an extensive air shower through the atmosphere to reach sea-level. This technique is therefore very useful in studying both the development of cosmic ray EAS, and also for gamma-ray astronomy. The Cerenkov technique is limited by the need for cloudless, moonless nights for observing. The technique was first applied to the detection of gamma-rays in 1962 (Chudakov et al. 1962).

As at air shower energies, Cerenkov experiments searching for Cerenkov light from gamma-ray showers must contend with the much larger background due to cosmic ray showers. The Cerenkov light from muons in EAS has been used as a veto (Grindlay 1971, Grindlay et al. 1975) and the imaging of the Cerenkov light pool may also allow cosmic ray air showers to be vetoed (Hillas 1985). Many experiments use the fact that the objects they observe are periodic and thus search for an excess due to gamma-rays over the non-periodic cosmic ray background.

Cygnus X-3 has been observed using the atmospheric Cerenkov technique for 15 years, beginning with the observations made at the Crimean Astrophysical Observatory after the 1972 radio outburst of Cyg X-3. A comprehensive review of atmospheric Cerenkov observations of Cyg X-3 up to 1984 was made by Weekes(1985). Weekes concluded that Cyg X-3 is not a steady emitter at TeV energies, and noted the difficulties in reconciling the pre-1980 USSR observations, showing strong emission at a phase of 0.2 and weak emission at a phase of 0.8, with post-1980 UK-USA observations which show strong emission at 0.6 and weak emission at 0.2.

Probably the most notable result at TeV energies has been the discovery of a 12.6 ms periodicity in events from the direction of Cyg X-3, ascribed to the pulsar period (Chadwick et al. 1985). This result was confirmed in both earlier and more recent data (Chadwick et al. 1987) and is in accord with previous

theoretical predictions (e.g. Eichler and Vestrand 1984). Four periods obtained from data sets spaced over four and a half years are consistent with a period derivative of 2.8×10^{-14} (Chadwick et al. 1987).

The atmospheric Cerenkov technique has been successfully used to observe a number of other sources, amongst them Cen A, Her X-1 and the Crab Nebula (e.g. Ramana Murthy 1987, Protheroe 1987b).

1.3.2 ULTRA-HIGH-ENERGY GAMMA-RAY ASTRONOMY

Several observations have been made of the Crab nebula at EAS energies. Dzikowski et al. (1983) found an excess from the general direction of the Crab Nebula. This experiment did not have any fast-timing capability and relied upon atmospheric attenuation to obtain directional information. Observations by Hayashida et al. (1981) and Craig et al. (1981) placed upper limits on the flux from the Crab Nebula. No conclusive evidence for UHE gamma-ray emission from the Crab Nebula has yet been found.

The viability of UHE gamma-ray astronomy was impressively demonstrated by the observation by Samorski and Stamm of Cyg X-3 (1983a). They used data collected with the Kiel scintillator array over the four years 1976-1979. Using an age cut (discussed further in Chapter 2), they found 31 events in a $\sim 4^\circ \times 3^\circ$ bin centred on Cyg X-3, when 14.4 were expected. More significantly,

when examined for the 4.8 hr periodicity of Cyg X-3, the phase bin centred on 0.35 (of phase width 0.1) contained 12 events, compared with an off-source average of 1.44 ± 0.04 . This is illustrated in Figure 1.7. This discovery was soon confirmed by Lloyd-Evans et al. (1983) with data from the Haverah Park array.

The unexpectedly high muon content of the EAS observed by Samorski and Stamm (1983b), coupled with claimed observations by underground detectors (both discussed further in section 2.2.1) cast doubts on the belief that the emissions from Cyg X-3 were UHE gamma-rays. However, no known particle could explain the observations. Only neutrons and neutrinos could possibly travel undeflected from Cyg X-3 to Earth. The neutron's half-life of 898 ± 16 s, implied energies $> 10^{18}$ eV for time dilation to prevent their decay en-route from Cyg X-3. Both Samorski and Stamm (1983a) and Lloyd-Evans et al. (1983) claimed detections of EAS with energies $< 10^{16}$ eV. The small neutrino interaction cross-section would require a prohibitively large neutrino flux from Cyg X-3, besides which, neutrino-initiated EAS would not be expected to produce the age distribution observed by Samorski and Stamm (1983).

Further aspects of these observations are discussed in Chapter 2. The significance of this discovery provided the motivation for many workers, and the detection of other sources followed. These are also discussed in later chapters.

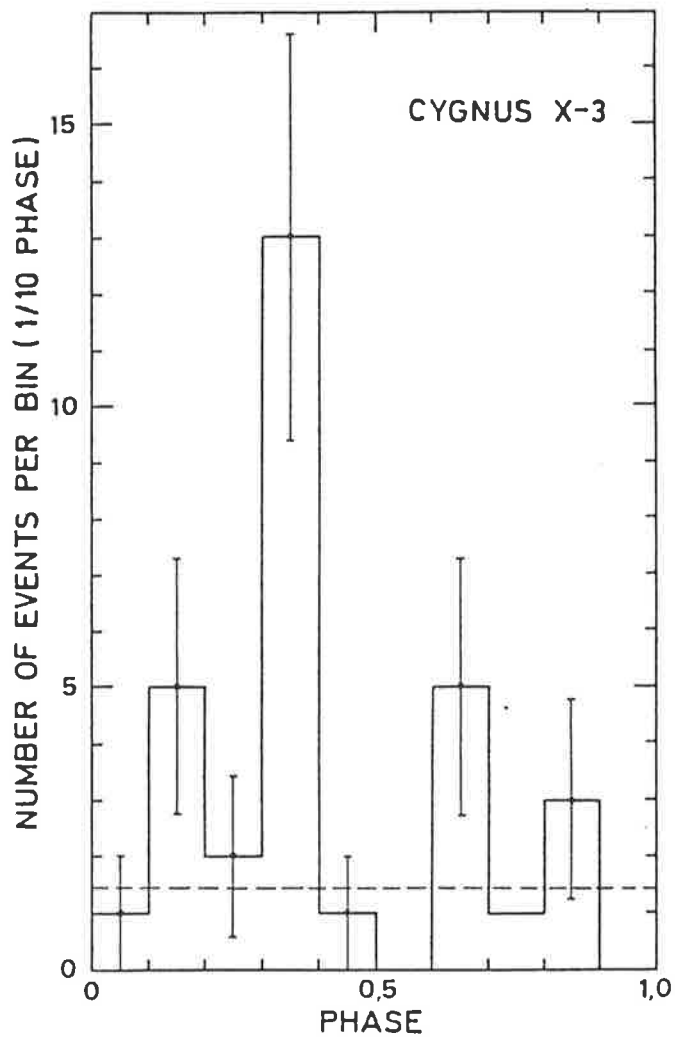


Figure 1.7

The phase histogram of the arrival times of EAS with $N_e \geq 10^5$ particles and $s \geq 1.1$ from the direction of Cygnus X-3 from Samorski and Stamm (1983a). The ephemeris of Parsignault et al. was used (see Samorski and Stamm (1983)). Error bars represent $\pm 1 \sigma$ statistical errors. The dashed-line corresponds to the average off-source rate.

The implications of the observations of Cyg X-3 are broad. Wdowczyk and Wolfendale (1983) noted that the apparently flatter exponent of gamma-ray spectra ($\gamma \sim -2$), would result in an increasing gamma-ray to cosmic ray ratio with increasing energy. They noted that this relative increase of gamma-rays may in some part explain the increasing anisotropy with energy. More intriguing is the suggestion by Hillas (1984a) that Cyg X-3 may be a mono-energetic accelerator of protons at $\sim 10^{17}$ eV. This would result in a luminosity of $\sim 10^{39}$ erg s^{-1} which is more than sufficient to provide the measured flux of cosmic-rays with $E > 10^{16}$ eV.

1.4 OVERVIEW

Recent models of the sources and acceleration mechanisms necessary to explain the observed cosmic ray energy spectrum are similar in form to that of Watson (1984), illustrated in Figure 1.8. It is generally acknowledged that shock acceleration of cosmic rays must occur in the inter-stellar medium. Lagage and Cesarsky (1983) have shown that particles in supernova shocks may be accelerated to a maximum energy of $\sim 10^4 Z$ GeV nucleus. Shocks generated at the boundary between the supersonic stellar

winds of young, bright stars and the surrounding medium (Cassé and Paul 1980) may extend this maximum energy to the region of the knee. Beyond the knee Cyg X-3 type objects may be the source of cosmic rays, as suggested by Hillas (1984a), until $\sim 10^{19}$ eV where anisotropy results show extragalactic sources seem to dominate. Although extragalactic, the absence of a Greisen-Zatsepin cut-off in the cosmic ray spectrum implies that these sources lie within ~ 50 Mpc.

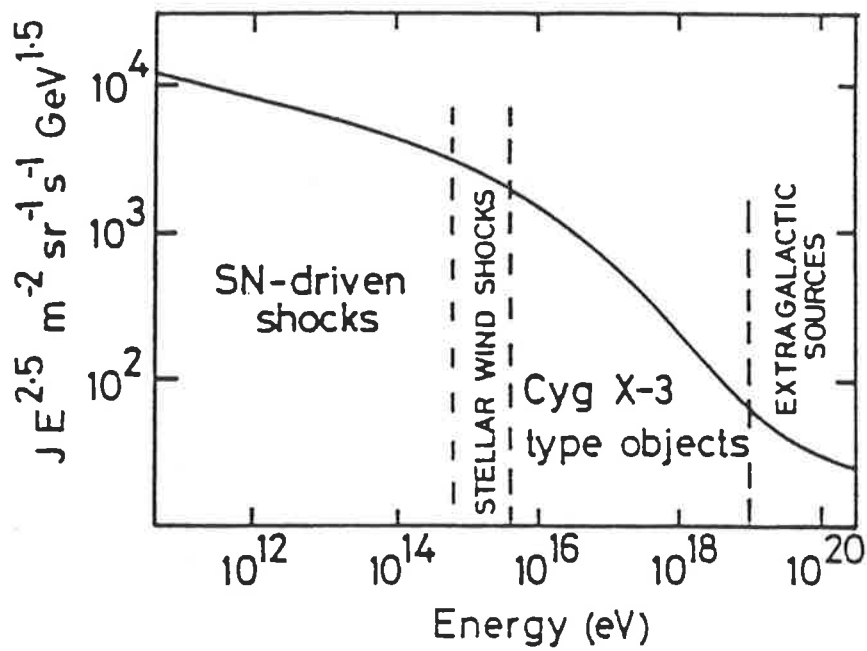


Figure 1.8

The energy spectrum of cosmic rays showing the possible sources and acceleration mechanisms for different energy ranges (From Watson (1984)).

CHAPTER 2

EXTENSIVE AIR SHOWERS

2.1 INTRODUCTION

In the first section of this chapter, the current understanding of the development of a cosmic ray initiated extensive air shower (EAS) is examined. The three main components of an extensive air shower - the hadron component, the muon component and the electromagnetic component - are discussed in turn.

In the second section, the conventional beliefs about the differences between cosmic ray initiated EAS and gamma-ray initiated EAS are examined in order to illustrate possible methods of vetoing cosmic ray initiated showers in ultra-high-energy gamma-ray astronomy. The questions raised by results from ultra-high-energy gamma-ray detections, and by recent calculations, will then be discussed.

2.1.1 THE HADRON COMPONENT

The energies of EAS-producing primary cosmic rays are still higher than the energies reached by man-made particle accelerators where $E_{\text{max}} \sim 2 \times 10^{14}$ eV (e.g. Eichten et al. 1984, see also Figure 1.1). Our understanding of hadronic interactions and the subsequent development of EAS is therefore based upon semi-empirical models formulated largely from extrapolations of accelerator results to cosmic ray energies.

An EAS is initiated when a primary cosmic ray enters the Earth's atmosphere with a velocity effectively that of the speed of light, and collides inelastically with the nucleus of an atmospheric atom or molecule. The primary passes through the nucleus colliding with one or two nucleons, which are ejected from the nucleus. The nucleus itself does not gain much energy from the collision. The fraction of energy lost by the initiating particle is termed the inelasticity. The energy lost in interactions is channelled into the creation of other particles. Particle production is usually separated into two momentum regions: the fragmentation (or projectile) region, and the central (or pionization) region. The former contains the remnant of the primary and other leading particles. The latter region corresponds to small momenta in the centre of mass (CM) reference frame and is where most new particle production occurs. The number of secondary particles produced in an interaction is termed the multiplicity, $\langle n \rangle$.

The majority of particles produced in hadronic interactions are pions, although kaons and other heavier hadrons may also be produced. Pions occur in positively charged, negatively charged and neutral forms and have masses $m_{\pi^+} = m_{\pi^-} = 140 \text{ MeV}/c^2$ and $m_{\pi^0} = 135 \text{ MeV}/c^2$. For sufficiently energetic primaries, pions are believed to be produced in equal numbers for each charge. Neutral pions have a half-life of $\sim 8 \times 10^{-17} \text{ s}$ and effectively decay immediately into two γ -rays (see section 2.1.3). Charged pions

have a half-life of 2.60×10^{-8} s and may themselves interact with atmospheric nuclei, or decay, depending on their altitude (i.e. on the atmospheric density at the height of their production). Kaons also occur in positively charged, negatively charged and neutral forms, and have masses $m_{K^+} = m_{K^-} = 494 \text{ MeV}/c^2$ and $m_{K^0} = 497 \text{ MeV}/c^2$. Both the neutral kaon, K^0 and its anti-particle, \bar{K}^0 , are produced in interactions. These two neutral kaons exist in quantum mechanically mixed states:

$$K_S^0 = \frac{1}{\sqrt{2}} (| K^0 \rangle + | \bar{K}^0 \rangle)$$

$$K_L^0 = \frac{1}{\sqrt{2}} (| K^0 \rangle - | \bar{K}^0 \rangle)$$

(e.g. Perkins 1972). Half of all neutral kaons produced are considered to be K_S^0 and the other half K_L^0 . Like pions, charged kaons may interact or decay. However, positive kaons are more likely to be produced in cosmic ray interactions than negative ones. The decay products of these hadrons fall into one of four categories:

- (i) pions, which themselves interact or decay
- (ii) muons (see section 2.1.2)
- (iii) electrons (see section 2.1.3)
- (iv) neutrinos and anti-neutrinos, which, due to their small interaction cross section, play no further part in shower development.

As the muon and electromagnetic components of EAS are both fed by the decays of pions and kaons, the rate of production of these particles determines the shower development. This rate of production depends on the inelasticity of the interacting particle, the multiplicity and the interaction cross-sections (often expressed in a reciprocal form as interaction mean-free-paths), all of which vary from model to model.

An early model for EAS was the CKP (Cocconi, Koester and Perkins) model (see de Beer et al. 1966). This model assumed an inelasticity of 0.5, and a nucleon interaction mean-free-path of 80 g cm^{-2} , independent of energy. The adopted multiplicity was

$$\langle n \rangle \propto E^{0.25},$$

similar to other "thermodynamic" models (e.g. Fermi 1951).

In order to facilitate extrapolation from accelerator data to the cosmic ray energies many orders of magnitude higher, "scaling" models were proposed. Specifically, three distinct forms of scaling can be distinguished:

- (i) Limiting fragmentation (Benecke et al. 1969)
- (ii) Feynman scaling (Feynman 1969)
- (iii) Radial scaling (Yen 1974).

Limiting fragmentation applies in the limit $S_{\frac{1}{2}} \rightarrow \infty$ and only to secondary particles with a significant fraction of the available CM momentum (where $S_{\frac{1}{2}}$ is the total energy in the CM frame). It follows from both Feynman and radial scaling.

The Lorentz invariant inclusive cross-section is expressed as a function of the CM energy, the transverse momentum and a dimensionless variable, x :

$$E \frac{d^3\sigma}{dp^3} = E_{CM} \frac{d^3\sigma}{dp^3} = f(x, p_T, S).$$

Scaling assumes this to be independent of energy, S :

$$E \frac{d^3\sigma}{dp^3} = f(x, p_T) \quad (2.1)$$

where $x = x_F = \frac{2 p_p^{CM}}{\sqrt{S}}$ for Feynman scaling

$$x = x_R = \frac{2 E_{CM}}{\sqrt{S}} = \sqrt{\frac{x_F^2 + 4(p_T^2 + m^2)}{S}}$$

for radial scaling

p_T = the transverse component of momentum

p_p = the parallel component of momentum

These two scaling models differ only in the central region, i.e. for relatively low energy particles, where radial scaling is a slightly superior model. These models predict multiplicities

$$\langle n \rangle \propto \ln(E).$$

Shortcomings of these models have become apparent, particularly with the advent of higher energy accelerators. It is now realised that the interaction mean free path is not independent of energy. This conclusion was first reached in studies of the development of cosmic ray showers (Yodh et al. 1972) and is

supported by accelerator results which show a clear increase in σ_{p-p} with energy. More recent results from cosmic ray experiments further support this (e.g. Baltrusaitis et al. 1984, Dawson et al. 1986).

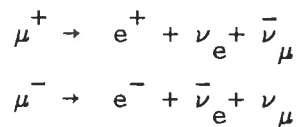
It has also become apparent that the scaling models have limitations. A model proposed by Gaisser et al. (1983) based on data from p-nucleus and π -nucleus interactions has a large violation of Feynman scaling in the central region, and a slower (logarithmic) violation in the fragmentation region. Although not universally accepted, violation of scaling in the fragmentation region is now commonly favoured (e.g. Wdowczyk and Wolfendale 1987). The model of Gaisser et al. finds an average inelasticity of ~ 0.63 .

For primary particles heavier than protons a superposition rule is commonly assumed, in which a primary of energy E and mass number A is considered to behave like A primary protons, each with energy E/A. The superposition rule ignores the shielding of nucleons in the nucleus, leading to an overestimation of the rapidity of the shower's development, and an underestimation of possible fluctuations in the development (Dixon et al. 1974). These become more significant with increasing primary energy. However, for calculations of the average characteristics of showers, the superposition rule is sufficient (Tomaszewski and Wdowczyk, 1975).

The large masses and relatively high energies result in little Coulomb scattering of the nuclear component during the development of the shower, and hence most of the particles in this component are found within a few metres lateral extent of the shower's core.

2.1.2 THE MUON COMPONENT

Muons are charged particles with a mass of $m_\mu = 106 \text{ MeV}/c^2$. They are produced in EAS by the decay of kaons and charged pions. Relativistic time dilation of the muon half-life of $2.2 \times 10^{-6} \text{ s}$ results in muons with Lorentz factors ≥ 20 being able to reach sea-level. Less energetic muons decay in flight, and contribute to the electromagnetic component:



Muons are leptons and thus do not interact with other particles, losing energy via ionisation at a rate of $\sim 2 \text{ MeV (g cm}^{-2}\text{)}^{-1}$. High energy muons ($E > 2 \text{ GeV}$) resulting from the decay of pions produced early in the life of the shower will, therefore, survive to sea level. The number and lateral distribution of these muons can be used to study early (i.e. high energy) interaction parameters (Elbert and Gaisser 1979). This in turn should reveal information on the composition of cosmic rays at energies well above satellite studies. Due to the small rate of

energy loss, the attenuation length of muons, λ_μ , defined by

$$N_\mu \sim \exp(-x/\lambda_\mu), \text{ is } \lambda_\mu \sim 1000 \text{ gcm}^{-2}.$$

This is approximately five times larger than the attenuation length of the electro-magnetic component. λ_μ is also energy dependent, increasing with increasing energy (Hara et al. 1983).

The lateral spread of the muon component is related to both the transverse momentum of the parent pions and kaons and to the height of their production. Although the average transverse momentum is small, the large height of production results in muons having a large lateral spread, with a median value of ~ 300 m (e.g. Allan 1971). The lateral distribution is flatter than that of the electromagnetic component and is of the form

$$\rho(N, r) \propto r^{-0.75} \left(1 + \frac{r}{k}\right)^{-2.5} \quad (2.2)$$

(Greisen 1960) where k is a function of the shower age and zenith angle (Hara et al. 1983). (Shower "age" is described in section 2.1.3)

Although muons are numerically smaller than the electromagnetic component, the average muon energy at sea level is ~ 5 GeV (with a median energy of ~ 1 GeV) (e.g. Allan 1971), compared to an average of ~ 20 MeV for the electromagnetic component. Thus the muons in a typical shower carry more total energy at sea level than the electromagnetic component.

As the muon component is more penetrating than the electromagnetic component, measurements of muon fluxes are made by covering detectors with large thicknesses of (dense) material to shield out the electromagnetic component. Detectors located in deep underground mines use the natural overburden of rock for the same purpose.

For low energy primary cosmic rays, the muon component is the only one to reach sea level. The most numerous component of the cosmic ray flux at sea level is due to these "unaccompanied" or "uncorrelated" muons. The total flux of muons ($p > 0.35$ GeV/c) at sea level is

$$J = (1.44 \pm 0.09) \times 10^{-2} \text{ cm}^{-2} \text{ s}^{-1},$$

or approximately $1 \text{ cm}^{-2} \text{ min}^{-1}$ (Allkofer et al. 1975). The zenith angle dependence is given by

$$J(\theta) \propto \cos^n \theta$$

where

$$n = 2.1 \pm 0.1 \quad (\text{Crookes and Rastin 1971}).$$

2.1.3 THE ELECTROMAGNETIC (EM) COMPONENT

The EM component arises from the cascading of electrons, positrons and photons and is numerically the largest component. As mentioned previously, the neutral pions produced in hadronic interactions effectively decay immediately into two gamma-rays. A gamma-ray of sufficient energy in the field of an atmospheric nucleus may undergo pair-production, creating an electron-positron

pair. Electrons and positrons accelerated in the field of a nucleus undergo bremsstrahlung ("braking radiation") producing further γ -rays. This cascading process continues and the EAS grows in size until it reaches "shower maximum" at which point particle losses become numerically greater than the particle creation. ("Electron" will be used from this point onwards to refer to both electrons and positrons.) For electrons, this occurs when the average energy per particle drops below the "critical energy" of

$$E_c = 84.2 \text{ MeV.}$$

Below this energy, ionisation loss becomes a more dominant process than bremsstrahlung. As the average photon energy decreases, Compton scattering and the photoelectric effect become more dominant loss mechanisms than pair-production. The shower maximum occurs deeper in the atmosphere with increasing primary energy, E_p , the two being related by

$$N_e (X_{\text{max}}) \approx \frac{E_p}{1.3 \times 10^9 \text{ eV}} \quad (2.3)$$

(e.g. Protheroe and Patterson 1984).

The behaviour of pure EM cascades is well understood (e.g. Rossi and Greisen 1941) and the EM component of EAS can be approximated by the summation of individual EM cascades initiated by photons from π^0 decay. One function describing the lateral distribution of EAS is the Moscow-M.I.T. function (Greisen 1960),

which approximates the lateral distribution with the function

$$\rho(N, r) = \frac{a N}{r} e^{-r/b} \quad 0.6 < r < 96 \text{ m} \quad (2.4)$$

$$\text{where } a = 2 \times 10^{-3}$$

$$b = 60 \text{ m}$$

(Refer to Greisen (1960) for the functions used for other radii.)

Another commonly used function is the NKG (Nishimura, Kamata, Greisen) function which is an approximation by Greisen (1956) to the theoretical expression for pure EM cascades of Nishimura and Kamata (1951). This includes an empirically derived term to make it fit EAS data. EM cascades can be characterised by an "age" parameter, s , (e.g. Rossi and Greisen 1941) which is zero at the start of the cascade, and increases monotonically with depth, being exactly one at shower maximum.

The NKG function is:

$$\phi(N, r) = \frac{N}{r_0^2} f_{\text{NKG}} \left(\frac{r}{r_0} \right) \quad (2.5)$$

$$\text{where } f_{\text{NKG}} \left(\frac{r}{r_0} \right) = C(s) \left(\frac{r}{r_0} \right)^{s-2} \left(\left(\frac{r}{r_0} \right) + 1 \right)^{s-4.5} \quad (2.6)$$

$$C(s) = \frac{\Gamma(4.5 - s)}{2\pi \Gamma(s) \Gamma(4.5 - 2s)} .$$

The Molière radius, r_0 , is altitude dependent, having the value of $r_0 \sim 79$ at sea level (Greisen 1960).

Calculations by Hillas and Lapikens and others (see Hillas and Lapikens (1977) and references therein) have revealed deficiencies in the NKG function. Hillas and Lapikens proposed a function similar to equation 2.6 with slightly varied exponents, and a considerably reduced value of r_0 of ~ 20 m. Another form

suggested by Hillas (Fenyves et al. 1983) is the use of equation 2.6 with $r_0 = 37$ m at sea level. Data on EAS lateral distributions also seem to indicate that the shower age is not independent of r , and the use of a local age parameter, $s(r)$, has been proposed (Capdevielle and Gawin 1982).

2.2.1 MUON CONTENT

Maze and Zawadski (1960) realised that gamma-ray initiated EAS should be deficient in muons. Muon progenitors, pions (and to a much smaller extent kaons), can only be created in the otherwise pure EM cascade by photo-pion production. The cross-section for photo-pion production is ~ 100 times smaller than that for production by protons i.e.

$$\frac{\sigma(\gamma + N \rightarrow \pi + \dots)}{\sigma(p + N \rightarrow \pi + \dots)} \sim 10^{-2}$$

An alternative method of muon production is pair-production, where a gamma-ray in the field of an air nucleus produces a $\mu^+ \mu^-$ pair. However, the cross-section for this process is inversely proportional to the square of the mass of the created particle, and so the ratio of muon to electron pair production is

$$\frac{\sigma(\gamma \rightarrow \mu^\pm)}{\sigma(\gamma \rightarrow e^\pm)} = \left[\frac{M_e}{M_\mu} \right]^2 \sim 2 \times 10^{-5}$$

Experimental investigation (e.g. Firkowski et al. 1961, Kamata et al. 1968, Gawin et al. 1968) confirmed the existence of μ -poor showers, which were initially attributed to gamma-rays. It was

later realised that other explanations could also be invoked (Maze et al. 1969), such as extreme upward fluctuations in π^0 multiplicities.

The Tien Shan group have recently confirmed these observations with the detection of μ -poor events (Nikolsky et al. 1987). They found that a muon content cut was not by itself sufficient to detect only primary gamma-rays, and required an additional deficiency in hadrons. The arrival directions of these events attributed to gamma-rays are not coincident with Cyg X-3 or the Crab Nebula, although this result is not in disagreement with quoted intensities for these sources. The directions appear to be localised in high galactic latitudes, although the low number of events makes drawing any conclusion difficult.

Early theoretical calculations by Karakula and Wdowczyk (1963), Wdowczyk (1965), and Braun and Sitte (1965) concluded that at energies of $10^{15} - 10^{16}$ eV, gamma-ray initiated EAS would have a muon content more than one order of magnitude lower than that of cosmic ray initiated EAS. Simulation of muons produced in the decay of photo-produced pions in cosmic ray showers (McComb et al. 1979) confirmed this conclusion.

More recent experimental results seem to contradict this, however. The Kiel observation of Cygnus X-3 and the detection of

an excess of air showers from the direction of the Crab Nebula both incorporated measurements of muon content. Samorski and Stamm (1983b) found a ratio of muon number in the events attributed to UHE gamma-ray to that of cosmic ray EAS to be 0.77. The Lodz group found the ratio to be -0.6 in their observation of the Crab Nebula (Dzikowski et al. 1983).

These observations prompted contemporary calculations to be made of the expected ratio. Edwards et al. (1985) adopted the hadronic interaction model of Gaisser et al. (1983) (see section 2.1). Photon-nucleus hadronic interactions were treated in the same way as pion-nucleus interactions (consistent with the similarity of γ -N and ρ^0 -N interactions (see Bauer et al. 1978)), with the exception that pions produced in the fragmentation region were taken to be neutral 75% of the time. The photon-air nucleus cross-section was derived by scaling the measured photon-nucleus cross-section with that for photon-carbon interactions, and assuming the same energy dependence as for the pion-nucleus cross-section. The energy spectra of muons in gamma-ray and proton-initiated EAS in the range $10^{15} - 10^{17}$ eV were calculated for an atmospheric depth appropriate for the Kiel observations of Cyg X-3. As primary energy cannot be directly measured, average muon number ($E_{\mu} > 1$ GeV) at fixed shower size was also calculated for gamma-ray and various cosmic ray initiated EAS. Results confirmed the earlier expectation that the ratio of the muon content of gamma-ray initiated EAS is ~.0.1 of proton-initiated showers. For a cosmic ray composition including a significant proportion of nuclei heavier than protons, the ratio at fixed shower size becomes even smaller (see Figure 2.1). Similar conclusions were reached by

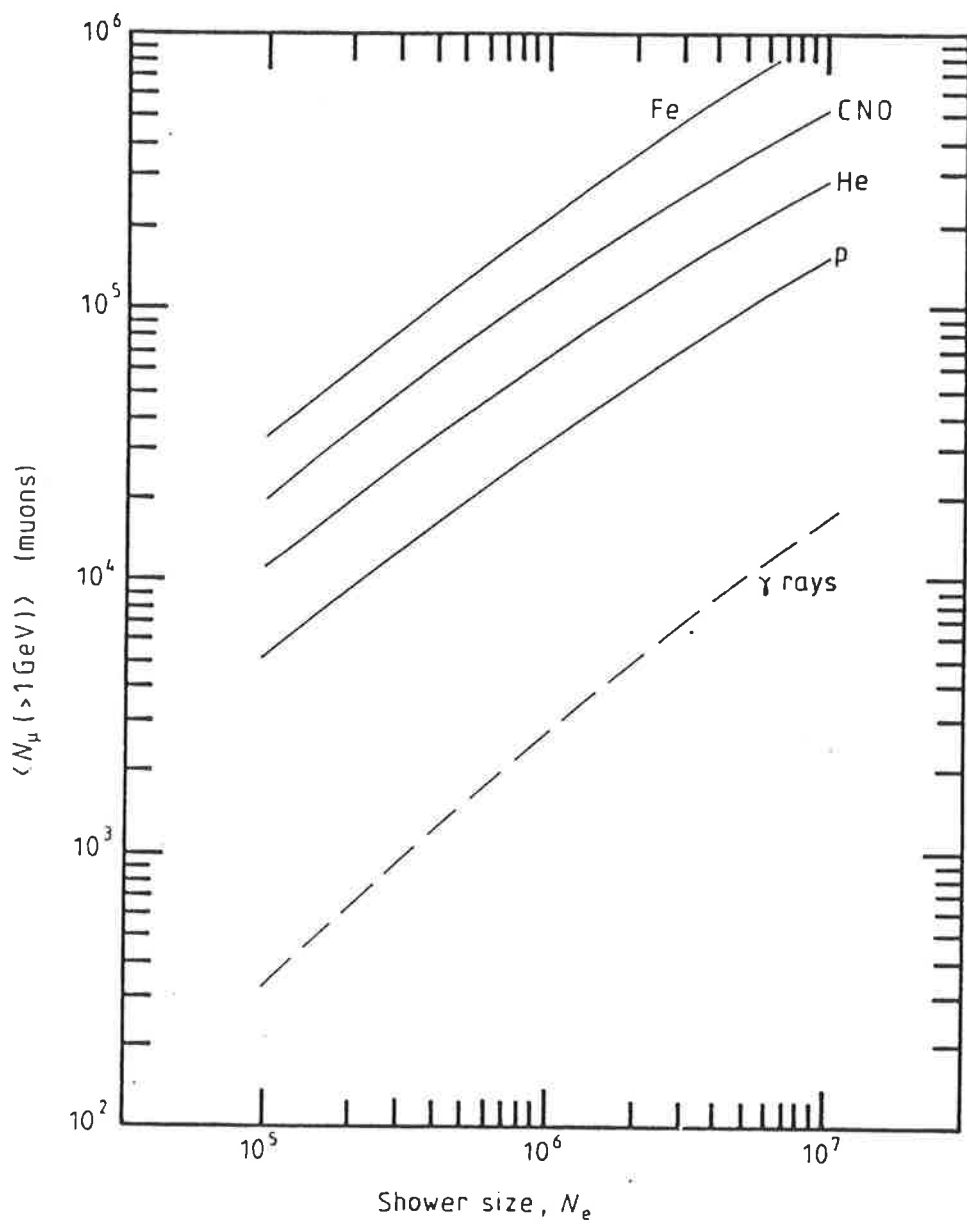


Figure 2.1. Average number of muons with $E > 1$ GeV at fixed, shower size at an atmospheric depth of 1130 g cm^{-2} in gamma-ray and various cosmic-ray-initiated EAS. (From Edwards et al. (1985)).

Stanev et al. (1985) who suggested that possibly one third of the observed muon density may be due to gamma-rays "punching through" the muon detector shielding and being registered as muons.

The Akeno observations of Cyg X-3 revealed a concentration of events near the phase 0.6, although only after employing a cut to ensure events were μ -poor (Kifune et al. 1986). A cut requiring the N_{μ}/N_{\circ} ratio to be one-thirtieth of the average N_{μ}/N_{\circ} ratio was used. Less severe cuts resulted in increasingly less significant phase enhancements. The resulting intensity was about the order of magnitude weaker than that obtained by Samorski and Stamm. The phase of the enhancement differed from that of Samorski and Stamm (1983) and Lloyd-Evans et al. (1983), although it is consistent with TeV and more recent PeV observations (e.g. Protheroe 1987b). The Akeno measurements of muon content were made at core distances > 50 m, significantly larger than those of Samorski and Stamm, which which were all made within 30 m.

The apparent disagreement between theory and experiment was intensified when two proton decay detectors separately reported an excess of muons from the general direction of Cyg X-3 and modulated with a 4.8 hour period. The Soudan 1 proton-decay detector recorded an excess of events between the phases 0.65 and 0.9 (Marshak et al. 1985a). Although the position of Cyg X-3 is $\alpha = 307.6^{\circ}$, $\delta = 40.8^{\circ}$, Marshak et al. found their signal strength was maximised by accepting events within 3° of $\alpha = 306.74^{\circ}$, $\delta = 43.5^{\circ}$. This offset from the direction of Cyg X-3 is significantly larger than the estimated uncertainty in the absolute orientation of the detector in the horizontal plane of $\sim 1.4^{\circ}$.

Using the real direction of Cyg X-3 reduces the signal strength to a value ~ 30% smaller (Marshak et al. 1985b). Marshak et al. noted that the phase enhancement is significantly broader than those seen in EAS work.

The Mt Blanc proton decay experiment recorded an excess between phases 0.7 and 0.8. The apparent signal from Cyg X-3 was a maximum in $10^\circ \times 10^\circ$ bin (Battistoni et al. 1985). This is significantly greater than the angular resolution of the detector of $\sim 1^\circ$.

Two other proton decay experiments found no evidence for any periodic enhancement in events from the direction of Cyg X-3 (Oyama et al. 1986, Berger et al. 1986).

The number of muons detected by the first two experiments were inconsistent with the particles from Cyg X-3 being gamma-rays (e.g. Marshak et al. 1985a). If neutrons were assumed (with implied $E > 10^{18}$ eV) the flux from Cyg X-3 would be greater than total cosmic-ray flux for $E > 10^{18}$ eV. Neutrinos could also be rejected on the grounds of the observed zenith angle distribution. A plethora of alternatives were proposed, including hadrons with strangeness, (Baym et al. 1985, Barnhill et al. 1985); photinos (Stenger 1985); gluinos (Auriemma et al. 1985) and glueballinos (Berenzinskii and Ioffe 1986). Severe constraints were placed upon all models.

2.2.2 SHOWER AGE

The conventional understanding of EAS development is that the energy in a pure EM cascade attenuates much faster than the EM component of a cosmic ray initiated by EAS as the latter is fed throughout the atmosphere by the interactions of the nuclear component. As a result, gamma-ray showers are expected to appear older than cosmic-ray EAS.

The muon poor showers observed by Gawin et al. (1968) had a mean age parameter of 1.4, whereas ordinary showers had a mean of 1.2. However, as discussed in the previous section, the origin of these showers cannot be attributed to gamma-rays with complete certainty. The belief that gamma-ray initiated EAS should appear older was supported by the observation of Cyg X-3 by Samorski and Stamm (1983b). They divided their data into two groups, steep (young) showers with $s < 1.1$, and flat (old) showers with $S \geq 1.1$. The D.C. excess of events from Cyg X-3 is only seen with the latter group. The confirming observation by Lloyd-Evans et al. 1983 was made without the use of an age cut. The Akeno group investigated the use of an age cut in their analysis of events from the direction of Cyg X-3 (Kifune et al. 1986). An age cut did not produce a significant result, although they note this may reflect a bias in their data collection trigger that may exclude older showers.

Protheroe et al. (1984) followed Samorski and Stamm by employing an age cut in the analysis of events from the direction of Vela X-1. A cut at the median value of $s = 1.3$ was adopted, and only events with larger age were accepted. A peak in the phase distribution was observed for events from within 2° of Vela X-1 in the phase bin centered on 0.63, and an examination of events of all ages revealed no events in this phase bin with $s < 1.3$. Van der Walt et al. (1987) analysed events from the direction of Vela X-1 as a function of shower age. The maximum signal was obtained for events with $s > 1.3$. Also, the claimed detections of ultra-high-energy gamma-ray emission from Vela X-1 and Cen X-3 by the BASJE collaboration (Suga et al. 1985) were made using both an age cut and a muon-content cut.

The observation of UHE gamma-rays from LMC X-4 by Protheroe and Clay (1985a) was made without an age cut. The shower age distribution was found to broaden significantly for events from declinations greatly different from the array latitude. The broadening of the cosmic ray age distribution and therefore presumably the gamma-ray initiated shower age distribution would have resulted in a greater overlap of the age distributions, rendering an age cut less useful.

However, calculations by Fenyves (1985) revealed that the age values of cosmic-ray and gamma-ray initiated EAS of the same sea level shower size were very similar, implying that an age cut did not provide the possibility of distinguishing between the two types of showers in the $10^{15} - 10^{16}$ eV energy range.

This result is confirmed by Hillas (1987b). Simulations of gamma-ray and cosmic ray-initiated showers showed that on average, gamma-ray showers were younger than cosmic ray showers.

In the light of these calculations, the detection of μ - and hadron-poor EAS attributed to gamma-rays by Nikolsky et al. (1987) is interesting. Their results agree with earlier observations on the flux of μ -poor showers, and they also observe an average age less than that for "ordinary" showers.

2.2.3 ANGULAR RESOLUTION

Gamma-ray sources appear as point sources convolved with the angular resolution of the array over the isotropic background of cosmic rays. The number of UHE gamma-rays emitted is very small, and in practice it is difficult to detect sources with great confidence by observing a D.C. excess alone. However, if the angular uncertainty in event arrival directions can be lessened, the signal to noise ratio will rapidly improve. A reduction in the angular resolution by a factor of two results in a reduction in the background by a factor of four, resulting in a greatly improved chance of observing a source. The angular resolution, Ω , is defined by

$$\Omega = \frac{\Delta t}{sc} \quad (2.7)$$

where Δt = uncertainty in relative arrival time between
detectors

s = distance between detectors

c = velocity of light.

For a given array, the angular resolution will depend on a number of factors:

(i) The accuracy in measuring the relative arrival times.

Factors affecting the measurement of the absolute arrival times are:

(a) The light detection electronics risetime.

The "fast" photomultipliers have risetimes of ~ 2-3 ns. The discriminators are triggered with a "jitter" due in part to the photomultiplier risetime and also to variations in pulse size and shape. This effect can be minimised with the use of a double discriminator (Clay and Ciampa 1986).

(b) The detector light collection risetime.

This also has a value of ~2-3 ns. Some groups paint the inside of their detectors black to eliminate internal reflections - however in both cases the first light to reach the photomultiplier will arrive at the same time. The light baffles used to maintain uniformity of light detection in the Buckland Park 2.25 m² detectors (see Chapter 3) are unfortunately not optimal for angular resolution as they impede the detection of direct light.

(c) The shower front thickness.

The shower front thickness is $\sim 1\text{m}$ at the core, i.e. $\sim 3\text{ ns}$, and increases with increasing core distance. It is obviously desirable to trigger off a particle at the leading edge of the shower front. This problem is directly related to the detector size.

These factors are the same in all detectors and result in an uncertainty in the relative arrival time between detectors of $\leq 3\text{ ns}$.

(ii) The spacing of detectors.

Equation 3.1 implies that an increased spacing results in an improved angular resolution. Whilst this is true, two factors act as constraints. With increasing separation, the curvature of the shower front (radius $\gtrsim 1\text{ km}$) becomes increasingly important. Also, at larger core distances, the number of particles decreases rapidly, which makes triggering from a leading particle much less likely. This can be overcome to some extent by some extent by placing a thickness of lead ($\sim 9\text{ mm}$ is optimal: Hillas 1987a, Bloomer et al. 1987) over the detector and making use of the Rossi transition effect to increase the number and size of signals close to the leading edge of the shower front (Clay 1985b, Linsley 1987).

(iii) The size of the detectors.

Although increasing the size of a detector results in a higher probability of triggering on a leading particle, in general the detector light collection rise-time also increases, resulting in no nett gain (Ciampa et al. 1986). Larger detectors also have the disadvantage that for showers with significant zenith angle, θ , they are elongated by $\sin\theta$, resulting in a spread in time of the light emission from the scintillator. Clay and Ciampa (1986) find that for a detector spacing of 20 m, a detector size of ~ 1 m results in acceptable angular resolution when these effects are considered.

(iv) The number of detectors triggered.

Obviously the more detectors triggered, the larger the overall array baseline. The angular resolution is thus a function of core position and shower size. Smaller showers, in general, trigger less detectors and with fewer leading particles and will, therefore, have a worse angular resolution. The question of detector thresholds is also important. Clay and Ciampa (1986) find that a density of ≥ 6 particles m^{-2} is required to obtain a reasonable assurance of sampling a particle within 1 ns of the true shower front.

2.2.4 SOURCE PERIODICITY

The most powerful technique in ultra-high-energy gamma-ray astronomy is to make use of any known periodicity displayed by the source being examined. In a binary system, such as those discussed in Chapter 5, gamma-ray emission may be modulated by any of three different physical processes - neutron star rotation, orbital motion or precession. The values of these vary from source to source, but in general the "pulse" period due to neutron star rotation ranges between several milliseconds and several minutes. The orbital period varies from ~ one hour to several weeks, and the precession period is generally greater than several weeks. Precession is not universally accepted as being the cause of this latter modulation. Other mechanisms, such as non-linear oscillations in the stellar companion (Kondo et al. 1983) have been postulated to explain this long term variation.

In any case, if a source is known to display periodic variations at other wavelengths, this known period can be used to examine air shower data for evidence of ultra-high-energy gamma-ray emission. A knowledge of the shape of the light-curve at other wavelengths is also useful in determining the appropriate statistical test to apply to the data (e.g. Protheroe 1987a).

In cases where an accurate period is not known, the data set can be tested over a range of possible periods. If the most significant trial period obtained in this way falls within the range of earlier period determinations, the evidence for emission is greatly enhanced.

There is evidence however that the pulse period may show significant variation in time. An example of this is Her X-1, which was recently detected by three different groups at a period $\sim 0.16\%$ lower than the accurately known x-ray period (Protheroe 1987b). The theoretical implications of these observations have yet to be fully understood.

2.3 SUMMARY

The characteristics of a cosmic ray initiated extensive air shower have been examined. Of the techniques to differentiate between cosmic-ray and gamma-ray initiated EAS, optimising the array angular resolution and using known source periodicities are both powerful and non-controversial. The situation for muon content and age cuts is not so clear however. Theory predicts that a muon cut can be used, though some experiments seem to refute this. In particular the observations by some underground detectors rule out a "conventional" muon content, although these observations have yet to be convincingly confirmed. Recent calculations deny the validity of an age cut, which has been used, seemingly successfully, in some experiments.

Clearly there is a long way to go before gamma-ray initiated extensive air showers are fully understood.

CHAPTER 3

THE BUCKLAND PARK AIR SHOWER ARRAY

3.1 THE AIR SHOWER ARRAY

3.1.1 THE DETECTORS

The Buckland Park Air Shower Array is situated slightly above sea-level on a coastal plain approximately 40 km north of the city of Adelaide, at longitude $138^{\circ} 28' E$ and latitude $34^{\circ} 38' S$. The array was established in 1971 with components from an array originally operated by the University of Calgary at Penticton, Canada.

The purpose of the array is to allow the determination of extensive air shower directions, sizes and core locations. To this end, detectors have a "slow", or amplitude measuring, photomultiplier for particle density measurements which enables the shower size and core position to be determined. A smaller, more central, subset of detectors also include "fast" photomultipliers to enable fast-timing measurements of the shower front for directional determination.

The earliest Buckland Park array consisted of 8 detectors, each a $1 \text{ m}^2 \times 50 \text{ mm}$ slab of NE102 plastic scintillator viewed from 530 mm below by a photomultiplier. These detectors were enclosed in light-tight boxes and housed in semi-permanent huts. Four detectors were situated at the corners of a square with 90 m sides, and the northern-most of these, together with the remaining four detectors formed the fast timing section of the array. Four of these fast-timing detectors were placed at the corners of a 30 m sided square, with the fifth at the centre of the square (see Figure 3.1). This array had a sea-level size threshold of $\sim 2 \times 10^5$ particles and an angular resolution of $\sim 1.25^\circ \text{ sec } \theta$.

The addition of three more detectors in 1977 increased the collecting area for large showers by a factor of ~ 4 (Crouch et al. 1981). These three detectors, labelled I, J and K, consisted of slabs of $1 \text{ m}^2 \times 10 \text{ mm}$ thick NE110 scintillator viewed from above at a distance of 500 mm by slow photomultipliers. These detectors were contained in pyramidal enclosures. This was the array configuration employed to give the 1979 - 1981 data set. (Gerhardy 1983, Gerhardy and Clay 1983). The angular resolution was unchanged but lateral distributions, previously fitted to a simple lateral distribution function, were now fitted with the NKG function to determine the shower age.

Following the work on anisotropy performed by Gerhardy and Clay (1983), it was decided to extend the array to allow the detection of smaller showers with primary energies below the "knee" in the spectrum. Infilling of the array with additional detectors

between 1981 - 1984 lowered the effective size threshold to $\sim 3 \times 10^4$ particles (Prescott et al. 1983, Clay et al. 1985). For the duration of this experiment, the array consisted of 27 "slow" detectors, 11 of which also contained a "fast" photomultiplier for directional analysis. The layout of the detectors is shown in Figure 3.1. The original C detector was moved to another site, R, and inverted (i.e. scintillator now viewed from above). The new C detector and the four new central fast-timing detectors used larger area, $2.25 \text{ m}^2 \times 50 \text{ mm}$, scintillators viewed from above. These were also housed in pyramidal detectors with a scintillator-photomultiplier separation of 700 mm and with a light baffle added between the scintillator and photomultiplier to improve the uniformity of response from the scintillator (Clay and Gregory 1978, Corani 1986). Of the $1 \text{ m}^2 \times 50 \text{ mm}$ "slow" density detectors, U and V were prototypes with scintillator-photomultiplier separations of 500 mm, while the remainder used a 600 mm separation. The plastic scintillator used in all the new detectors (after U and V) was manufactured by C.I. Industries (Tokyo, Japan). All faces of the scintillator slab not directed viewed by the photomultiplier, and all detector interiors, were painted with white NE560 scintillator paint or equivalent (Clay and Gregory 1978) to improve light collection. All huts were thermally insulated with sheets of glass wool and a covering of double-sided reflective thermal insulator (sisalation).

In addition to the work purely involving the scintillator array, studies have been undertaken of the lateral distributions (Kuhlmann and Clay 1981, Dawson 1985) and temporal structure of

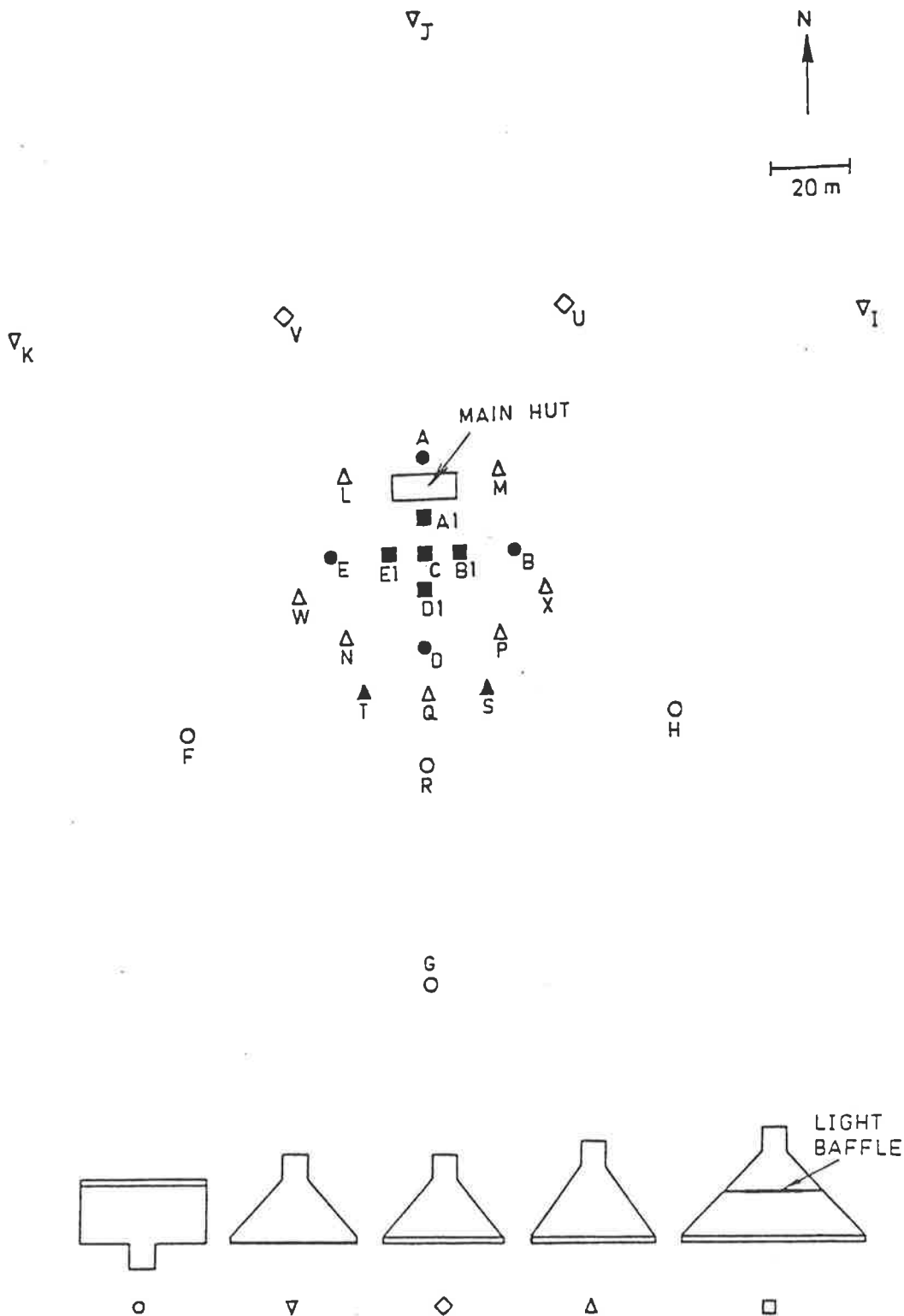


Figure 3.1. The layout of the Buckland Park array for this experiment. The main hut houses the electronics and recording system. Symbols represent various detector configurations. Filled shapes designate detectors used for both fast-timing and density analysis (Note that R detector is actually inverted from the form shown so that its photomultiplier is above the scintillator.)

the Cerenkov radiation associated with EAS (Liebing et al. 1981) . Cerenkov radiation has also been used to study the development of EAS (Thornton and Clay 1979, 1981). The detectors used for these studies will not be described here.

Scintillators generally are substances which emit light when a charged particle passes through them. They include inorganic crystals as well as organic crystals, liquids and plastics. The passage of a charged particle through an organic scintillator results in the excitation of molecular states which emit ultraviolet light upon de-excitation. This light is converted to visible wavelengths by the inclusion of suitable fluorescent dyes. The general-purpose plastic scintillator used in the Buckland Park array, NE102, has a density of 1.0 g cm^{-3} and a light yield of 13 photons/keV, with a wavelength of maximum emission of 423 nm (see Figure 3.2a). The NE110 scintillator used in I,J and K is very similar with a wavelength of maximum emission of 434 nm (Figure 3.2b), but is slightly slower, having a characteristic decay time of 3.3ns compared with 2.4ns for NE102. The C.I. Industries scintillator used in detectors added since 1981 has similar characteristics to the Nuclear Enterprises Scintillator. The light produced in the scintillator is detected by either a "fast" or "slow" photomultiplier.

3.1.2 THE FAST-TIMING SYSTEM

The aim of the fast-timing system is to record, as accurately as possible, the time of passage of a shower front through a scintillator. Philips model XP 2040 photomultipliers are used for

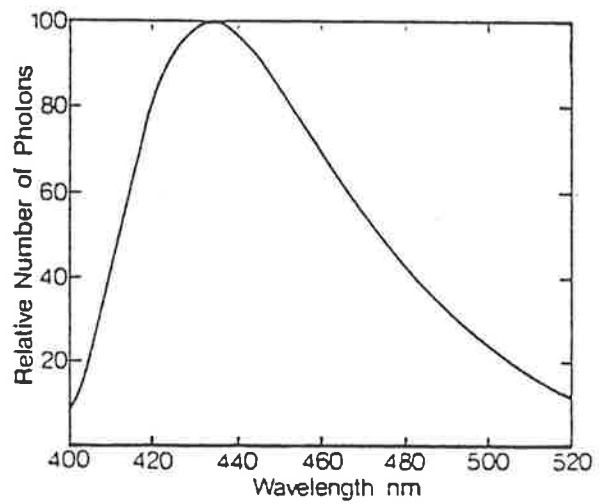
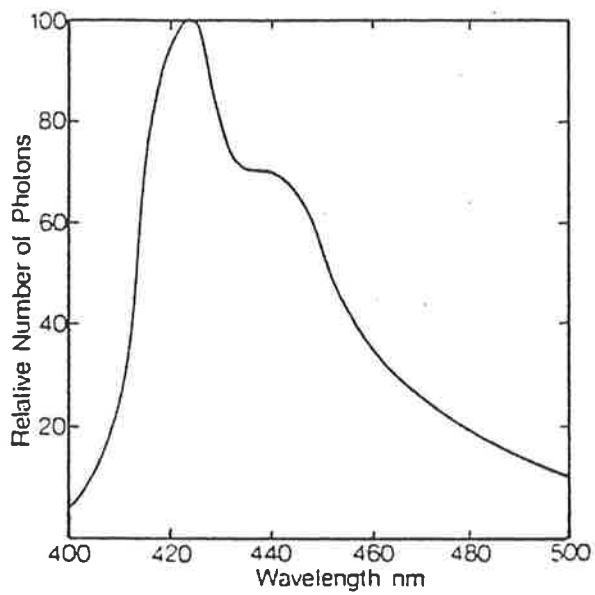


Figure 3.2. The relative number of photons produced as a function of wavelength for
 (a) NE 102 plastic scintillator
 (b) NE 110 plastic scintillator

this purpose as they have fast ($\sim 2\text{ns}$), consistent rise-times. These photomultipliers have a convex photocathode with a diameter of 110 mm, and are most sensitive to wavelengths of $420 \pm 30\text{nm}$, (see Figure 3.3a) which matches the maximum scintillator emission. The photomultipliers consist of 14 dynodes and are operated at about 2100 V, producing a gain in excess of 3×10^7 . Output pulses from the photomultipliers are taken through 50Ω cable to the recording system which is housed in an ATCO hut near the centre of the array (see Figure 3.1). Signals from the closer detectors are transmitted by RG58 cable, whereas wider bandwidth RG8 cable is used for the more distant fast-timing huts. The signals are taken to a discriminator set nominally at the two particle level, producing a discriminator output signal rate of $\sim 100 \text{ Hz}$. The discriminator outputs are then taken via an electronic delay to LeCroy 2228A TDC's (Time to Digital Converters) housed in a CAMAC crate. The TDC's measure pulse arrivals with $\sim 1 \text{ ns}$ resolution. The TDC's are calibrated (and the calibration checked at regular intervals) using a square wave pulse generator and a set of variable delays. The TDC is started by a direct pulse and stopped after a known delay. The linearity of the TDC's is found to be very good and to show negligible variation between calibration checks.

3.1.3 THE DENSITY MEASURING SYSTEM

The amount of light produced by the passage of the high-energy particles in EAS through a scintillator is almost

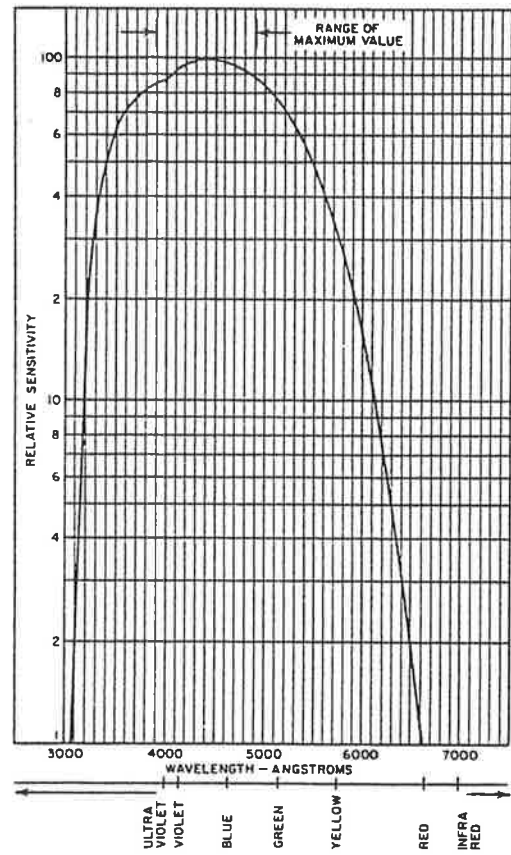
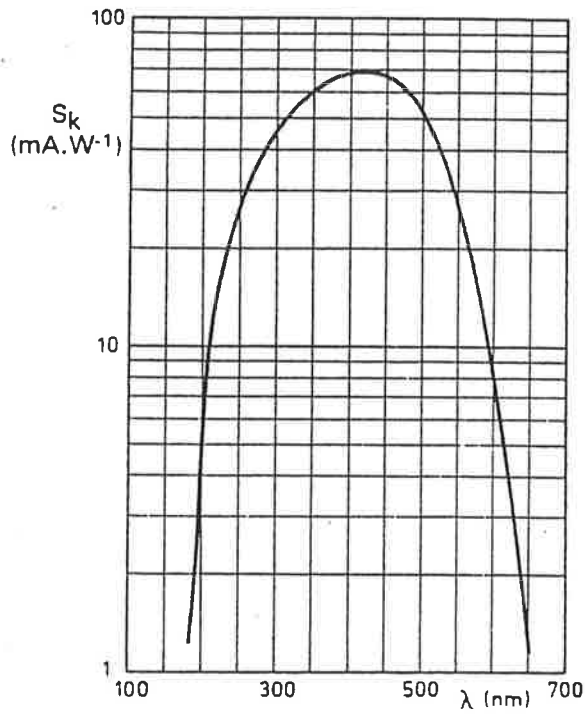


Figure 3.3. The sensitivity of the photomultiplier tubes as a function of wavelength for
 (a) the Philips XP 2040 photomultiplier tubes used for fast-timing
 (b) the RCA 8055 photomultiplier tubes used for density measurements.

independent of both particle type and energy. The light output is proportional to the energy deposited in the scintillator by the particles, $\sim 2 \text{ MeV (g cm}^{-2}\text{)}^{-1}$ (Hayakawa 1969). Thus, the amount of light produced by a scintillator is closely proportional to the number of particles passing through it. "Slow" photomultipliers (so-called because a fast rise-time is not necessary) are used to measure particle densities and are chosen to produce an output pulse proportional to the incident light. The RCA 8055 photomultipliers (or in some huts an equivalent replacement model) used were specifically intended for use with scintillation counters, and have a maximum response for wavelengths of $440 \pm 50 \text{ nm}$ (see Figure 3.3b). The photomultipliers have a flat, circular photocathode with a diameter of 110 mm, with a 10 stage dynode system, and are operated at 900 V. Output pulses are taken to nearby on-site charge-sensitive pre-amplifiers. These effectively integrate over the length of the output pulse and produce a pulse (rise-time $\sim 500 \text{ ns}$, decay $\sim 5 \mu\text{s}$) with an amplitude proportional to the integrated charge (in turn proportional to the light incident on the photocathode). These pulses are then taken to peak-sensing ADC's (Analogue to Digital Converters) in the recording hut via RG58 cable.

As stated in section 2.1.2, the most abundant component of EAS at sea-level is the unaccompanied muon flux. These muons are the "standard candle" of density measurements which are made in terms of "equivalent single vertical muons". The pulse height spectrum of a scintillator is almost entirely due to the passage of

single muons from all directions except for a tail due to EAS. The shape of this spectrum is due to

- (i) Landau fluctuations in the muons traversal. (i.e. statistical fluctuations in the number of interactions, and in the amount of energy lost per interaction.)
- (ii) Non-uniformity across a scintillator of light collection by the photomultiplier. (Generally speaking, the further the muon passes from the centre of the scintillator the less light collected by the photomultiplier.)
- (iii) Variation in the angle of incidence of the muon. (For larger zenith angles the muon passes through a greater thickness of scintillator, thus producing more light.)

The single ungated muon spectrum (sometimes approximated to a Landau distribution) contains a peak (provided the scintillator is thick enough), called the single particle peak (SPP), illustrated in Figure 3.4. At Buckland Park the SPP is routinely measured for each detector with an MCA (Multi-Channel Analyser).

The SPP (i.e. the mode of the pulse height spectrum) is a very good approximation to the mean pulse height for vertical single muons. This is because the ratio of the mean to the mode of a Landau distribution is 1.3 (White and Prescott 1968), and fortuitously, the SPP of (gated) vertical muons is a factor of ~ 1.3 less than the SPP for the (ungated) omni-directional muons (Clay and Gregory 1978).

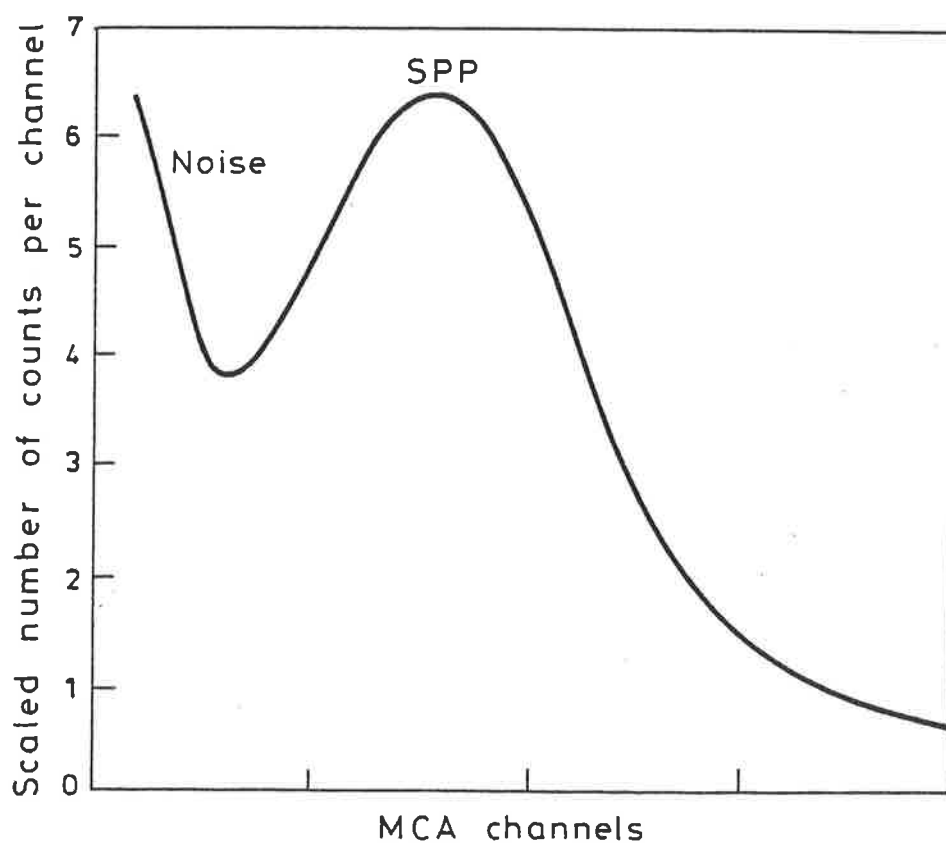


Figure 3.4. Typical single particle peak for density measuring detector signals.

Density measurements are recorded as ADC numbers, and so one must divide them by the effective ADC reading for the SPP in order to convert them to equivalent single vertical muons. SPP's are measured with an MCA, and so a two stage intercalibration is done. A tail-pulse generator (Berkeley Nucleonics Corporation) is used to simulate the preamplified slow pulses and thus calibrate the ADC in terms of pulse amplitude. This pulse generator is also used to calibrate the MCA channel number in terms of the pulse amplitude. These calibrations are routinely checked and found to show negligible variation with time.

3.1.4 DATA COLLECTION

Concurrent to the addition of detectors between 1981-1984, the measurement and control system was upgraded (Dawson 1985). The predominantly "home-built" electronics (including PAJAMAS-Phil (Crouch) And Jim (Kuhlmann's) Amazing Measurer of Air Showers) were replaced by a CAMAC (Computer Automated Measurement and Control) based module system and a Data General Nova 4S mini-computer. The Kinetic System CAMAC crate can accommodate up to 25 plug-in modules, and is interfaced with the computer by a Nuclear Enterprises 9030 CAMAC controller containing a NE9039 Nova interface board. For this experiment, the CAMAC crate contained three 12-channel peak-sensing LeCroy 2259A ADC's, two 8 channel LeCroy 2228A TDC's, a LeCroy 2251 12 channel Scaler (used to monitor selected fast and slow detector rates) and a home-built data logger to input data from the clock, thermometers and barometer.

The array trigger criterion (i.e. the requirement for an event to be recorded) is that 2 of the 11 fast-timing detectors must trigger above their ~ 2 particle discrimination level and also two of the inner 19 slow-detectors must trigger above their ~ 6 particle discrimination level. Only the inner 19 detectors (i.e. not F, G, H, I, J, K, U, V) are used. This ensures that shower cores are most likely to fall within the enclosed area of the array. As the individual fast rates are ~ 100 Hz and slow rates ~ 1 Hz, the latter effectively controls the array trigger rate of ~ 0.1 Hz. (For a short period (while a fault was repaired) the array trigger was the slow trigger only. However, from the above arguments, this should have made no significant difference to the events selected).

The 2 from 11 fast coincidence also acts to start the TDCs. All fast timing pulses are delayed by stable electronic delays of ~ 200 ns between the discriminator and before the TDC stop to overcome problems that otherwise arise due to the variation in cable lengths between detectors and the main hut and delays due to the angle of incidence. Following an array trigger all TDC's and ADC's and data from the data logger are read by the computer and this information written onto 2400 ft magnetic tape. Selected detector rates are written to tape every 15 minutes. Tapes require changing every ~ 4 days and are brought back to the university for analysis on a VAX 11/785 computer. A schematic diagram of the array electronics is shown in Figure 3.5.

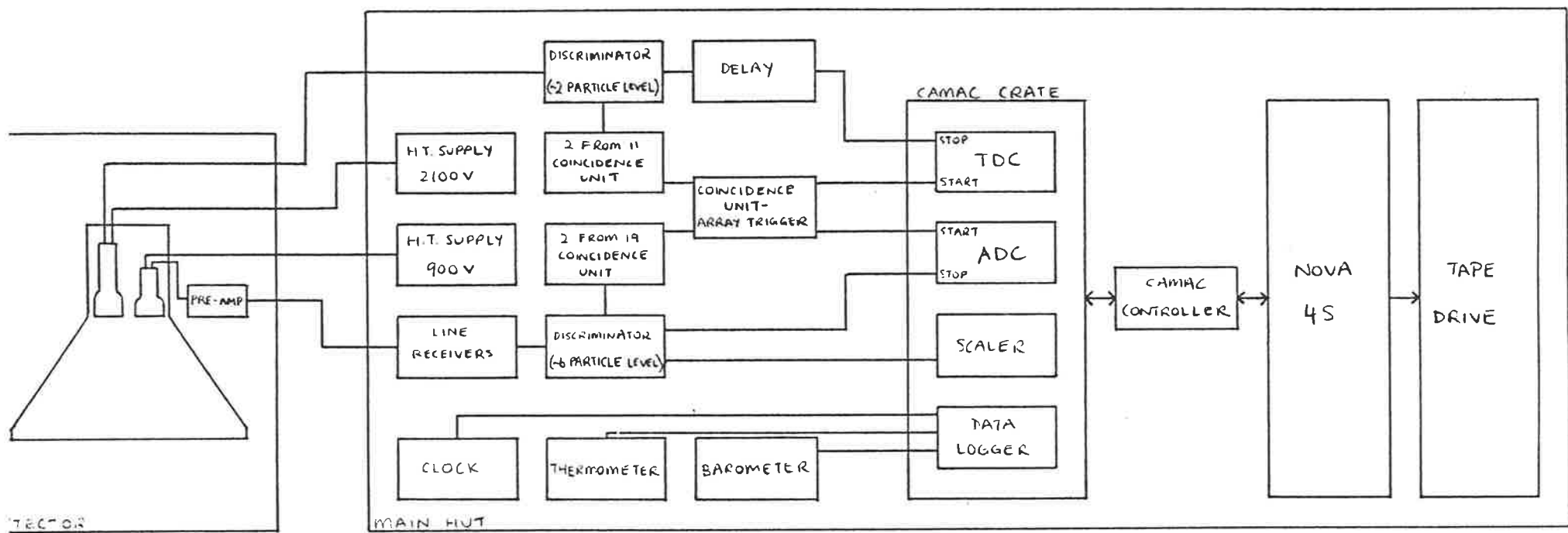


Figure 3.5. Schematic diagram of the Buckland Park Array.

3.2 DIRECTIONAL ANALYSIS

3.2.1 TIMING DIFFERENCES

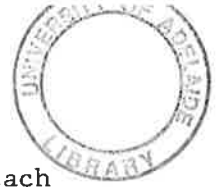
To calculate the arrival direction of an EAS, the relative arrival time of the shower front at each detector triggered by the passage of the shower must be accurately known. For each analysable event, a "reference" detector is chosen, and all other times made relative to this. This involves subtracting the time delays due to light collection, cable lengths and electronic delays between discriminator and TDC stop.

Rather than explicitly measuring these delays, we use the fact that EAS are expected to arrive, on average, preferentially from the zenith (with no azimuth angle dependence). The mean timing difference between a pair of detectors

$$\overline{t_i - t_j} = \overline{\Delta t_{ij}} = \frac{1}{N} \sum_{k=1}^N \left[t_i(k) - t_j(k) \right] w_i(k) w_j(k)$$

$w_i(k) = 1$ if the i th detector was triggered by the k th event
 $= 0$ otherwise

will, particularly for large N , be an excellent approximation to the time difference between the pair of detectors for vertical showers. Subtracting this amount from individual timing detectors removes the effects of the delays to give one time relative to the other. Thus for an individual shower, the relative arrival time at hut j with respect to hut i is



$$t_j = t_i - \overline{t_i - t_j}$$

For every tape the mean timing difference is calculated for each detector with respect to all 10 other detectors. These are stored in the 11 x 11 skew symmetric array defined in Table 3.1.

Calculating the time differences this way process assumes that all detectors triggered in an event were triggered by the shower front of the same EAS. Whilst this is true in the vast majority of cases, it is not always necessarily true. The effect of detectors being triggered by unconnected particles is to add-in spurious time differences, distorting the mean. To ensure that this distortion is kept to a minimum, the calculated mean timing differences are re-calculated with the additional proviso that unphysical time differences are disregarded. An unphysical time difference for a given pair of detectors is a time difference that is greater than the light travel time between the two detectors, i.e.

$$(t_i - t_j)_{\max} = \frac{\sqrt{(x_i - x_j)^2 + (y_i - y_j)^2}}{c}$$

In practice, this iterative "feed-back" process (using previously calculated timing differences to calculate a better set of timing differences) is repeated until two consecutive sets of differences are the same. Thus a better estimate of the mean-timing difference between each pair of detectors is obtained. (Despite the removal of unphysical time differences, there still remains the (smaller) contribution of physically feasible differences:

$$t_i - t_j < (t_i - t_j)_{\max}$$

where one of the times is unrelated to the passage of the EAS shower front. This is a "second order" effect, and is discussed further in section 4.6.)

Obtaining the mean-timing difference for all eleven detectors with respect to each other results in fifty-five individual differences. It was found, however, that a better estimate of the mean-timing differences, was obtained by defining ten "fundamental" timing differences, and generating the other forty-five from combinations of these ten. The ten fundamental timing differences are chosen to be the timing differences between each detector and its closest neighbouring detector. This method is also employed by the Kolar Gold Field group (Bhat et al. 1985)

The distributions of time differences, $t_i - t_j$, are found to have standard deviations that are, to a good approximation, linearly proportional to the distance between the two huts i and j . The means obtained for the ten fundamental timing differences will be the best defined, as they will have the smallest standard deviations, and are also calculated from larger numbers of events. The latter results from the fact that (particularly smaller) showers are more likely to trigger adjacent detectors than pairs of detectors with larger separations. The fundamental timing differences are highlighted in Table 3.1, and illustrated in Figure 3.6. (Note that as the array is skew-symmetric, each of the 10

Table 3.1.

0	B-A	C-A	D-A	E-A	A1-A	B1-A	D1-A	E1-A	S-A	T-A
A-B	0	C-B	D-B	E-B	A1-B	B1-B	D1-B	E1-B	S-B	T-B
A-C	B-C	0	D-C	E-C	A1-C	B1-C	D1-C	E1-C	S-C	T-C
A-D	B-D	C-D	0	E-D	A1-D	B1-D	D1-D	E1-D	S-D	T-D
A-E	B-E	C-E	D-E	0	A1-E	B1-E	D1-E	E1-E	S-E	T-E
A-A1	B-A1	C-A1	D-A1	E-A1	0	B1-A1	D1-A1	E1-A1	S-A1	T-A1
A-B1	B-B1	C-B1	D-B1	E-B1	A1-B1	0	D1-B1	E1-B1	S-B1	T-B1
A-D1	B-D1	C-D1	D-D1	E-D1	A1-D1	B1-D1	0	E1-D1	S-D1	T-D1
A-E1	B-E1	C-E1	D-E1	E-E1	A1-E1	B1-E1	D1-E1	0	S-E1	T-E1
A-S	B-S	C-S	D-S	E-S	A1-S	B1-S	D1-S	E1-S	0	T-S
A-T	B-T	C-T	D-T	E-T	A1-T	B1-T	D1-T	E1-T	S-T	0

The 11 x 11 skew symmetric timing difference array. In the upper right-hand side $\frac{1}{2}$, the ten fundamental timing differences (see text) are

highlighted B-A represents $\overline{t_B - t_A}$ etc, where these mean values are obtained using equation 3.1.

Table 3.2.

0.0	0.4	0.1	-0.2	-0.6	0.1	-0.3	0.4	-0.1	0.2	-1.3
-0.4	0.0	-0.3	-0.5	-0.6	0.0	0.1	-0.2	-0.5	0.1	-0.9
-0.1	0.3	0.0	-0.2	-0.7	0.2	0.3	0.0	-0.2	0.3	0.0
0.2	0.5	0.2	0.0	-0.5	0.4	0.4	0.2	0.0	0.4	0.0
0.6	0.6	0.7	0.5	0.0	0.5	0.2	0.3	0.2	1.0	-0.2
-0.1	0.0	-0.2	-0.4	-0.5	0.0	-0.1	-0.1	-0.4	0.1	-0.6
0.3	-0.1	-0.3	-0.4	-0.2	0.1	0.0	-0.2	-0.3	0.0	1.1
-0.4	0.2	0.0	-0.2	-0.3	0.1	0.2	0.0	-0.4	0.5	-0.5
0.1	0.5	0.2	0.0	-0.2	0.4	0.3	0.4	0.0	0.9	-0.8
-0.2	-0.1	-0.3	-0.4	-1.0	-0.1	0.0	-0.5	-0.9	0.0	-0.5
1.3	0.9	0.0	0.0	0.2	0.6	1.1	0.5	0.8	0.5	0.0

Timing differences for consecutive tapes (30 December 1985 - 27 December 1985) illustrating consistency between tapes. The pairs of huts with the largest variation between tapes are those with the largest separations, as expected.

Table 3.3.

0.0	-0.4	2.2	-0.8	0.0	-0.2	-0.4	0.0	0.0	0.2	0.1
0.4	0.0	2.0	-0.6	0.3	-0.4	-0.2	-0.1	-0.2	-0.4	-0.2
-2.2	-2.0	0.0	-2.1	-2.1	-2.6	-2.0	-2.0	-2.3	-2.0	-2.2
0.8	0.6	2.1	0.0	-0.3	0.0	0.2	-0.1	0.1	0.4	-0.4
0.0	-0.3	2.1	0.3	0.0	-0.3	-0.5	-0.1	-0.2	-0.7	-0.6
0.2	0.4	2.6	0.0	0.3	0.0	0.3	0.4	0.2	0.2	0.4
0.4	0.2	2.0	-0.2	0.5	-0.3	0.0	-0.1	-0.1	-0.3	-0.7
0.0	0.1	2.0	0.1	0.1	-0.4	0.1	0.0	0.0	0.1	0.0
0.0	0.2	2.3	-0.1	0.2	-0.2	0.1	0.0	0.0	-0.3	-0.3
-0.2	0.4	2.0	-0.4	0.7	-0.2	0.3	-0.1	0.3	0.0	-0.9
-0.1	0.2	2.2	0.4	0.6	-0.4	0.7	0.0	0.3	0.9	0.0

A comparison of timing differences of consecutive tapes (2nd August 1984 - 30 July 1984) where the delay of one detector has changed with respect to all other detectors.

Table 3.4.

0.0	0.0	0.1	-1.5	0.1	0.2	-0.1	-0.4	-3.0	-3.9	-5.0
0.0	0.0	-0.1	-0.3	0.4	0.1	-0.1	0.1	-2.6	-2.9	-3.2
-0.1	0.1	0.0	-0.6	0.0	0.3	0.1	-0.2	-3.1	-3.0	-4.0
1.5	0.3	0.6	0.0	0.1	0.8	0.6	0.4	-2.5	-3.0	-3.6
-0.1	-0.4	0.0	-0.1	0.0	0.2	-0.2	-0.2	-3.1	-3.2	-4.1
-0.2	-0.1	-0.3	-0.8	-0.2	0.0	-0.4	-0.4	-3.4	-3.4	-4.3
0.1	0.1	-0.1	-0.6	0.2	0.4	0.0	-0.2	-2.8	-3.8	-3.8
0.4	-0.1	0.2	-0.4	0.2	0.4	0.2	0.0	-2.9	-3.3	-3.7
3.0	2.6	3.1	2.5	3.1	3.4	2.8	2.9	0.0	-0.6	-0.9
3.9	2.9	3.0	3.0	3.2	3.4	3.8	3.3	0.6	0.0	-0.2
5.0	3.2	4.0	3.6	4.1	4.3	3.8	3.7	0.9	0.2	0.0

Variations between two consecutive tapes (18 April 1986 - 11th April 1986) illustrating the three huts of the second TDC all varying with respect to the first TDC.

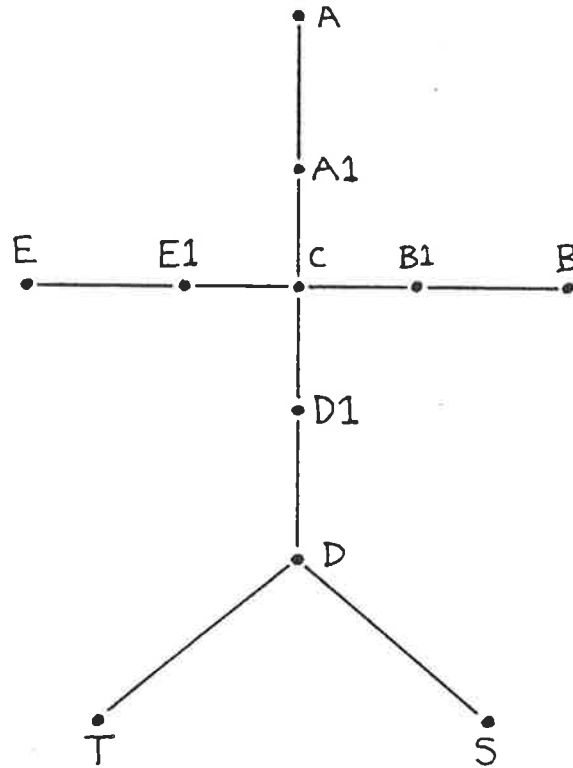


Figure 3.6. The ten "fundamental" timing differences. All other timing differences can be generated from combinations of these

fundamental timing differences appears twice: only the top right hand side will be used for the purposes of this discussion.) The mean timing difference between any pair of detectors can be found by adding appropriate fundamental differences.

Use of this technique also eliminates the problem of choosing a reference detector for each event. If the fundamental timing differences were not used, the calculated direction would vary (albeit slightly) depending on the choice of the reference hut. By generating the mean-timing difference array from the ten fundamental timing differences, an internally consistent set of differences is obtained, and the calculated direction is independent of the choice of reference hut.

If no alterations are made to the array, one would expect that the mean timing differences would show only small statistical fluctuations between consecutive tapes. This is found to be the case, as is illustrated in Table 3.2, where the mean timing difference array for one tape is subtracted from the array for the following tape to facilitate inspection for variation. The average variation between the two tapes is less than 1 ns. In general it is the detectors with the largest separations that show the largest variations between tapes, as expected. In particular, the variation between tapes of the ten highlighted fundamental timing differences are all small.

A second example, shown in table 3.3, displays a comparison of differences where the delay of the C detector has been altered by ~ 2 ns between the two tapes. All differences have changed by ~ 2 ns with respect to C, with statistical fluctuations resulting in the spread of the actual values.

The few occasions such as the one illustrated in Table 3.4 are somewhat puzzling. In this case the three fast-timing detectors in the second TDC have all changed by ~ 3 ns with respect to the detectors in the first TDC. This was observed to happen on several occasions, only to reverse itself after two or three tapes. The reason for this is not known, but careful monitoring of the variation of the timing differences between consecutive tapes allows such instances to be isolated and individually treated.

The relative stability of the timing differences allows them to be averaged over several tapes to obtain a better estimate of the mean. Checking for variations between tapes is of paramount importance then, so that no large variation in any timing difference is unwittingly used, resulting in an inaccurate mean time difference. In instances such as the one described above, the timing differences for the 8 detectors in the first TDC could still be averaged over several tapes, but the three detectors of the second TDC could only be averaged over the few tapes they maintain the ~ 3 ns alteration.

In conclusion, time differences are averaged over each tape and, where their consistency allows, over consecutive tapes. The 10 fundamental time differences are used to generate a self-consistent set of accurate timing differences. These are finally altered to take into account the small, but significant variations from a horizontal plane of the detectors. The procedure of obtaining the set of timing differences used in directional analysis is outlined in Figure 3.7.

3.2.2 UNPHYSICAL TIMES

As mentioned in the previous section it was found that a small but significant proportion of events included one or more detectors triggered by particles unconnected with the passage of the shower front triggering the remaining detectors. Obviously these detectors must be excluded before a directional analysis is attempted.

Figure 3.8a illustrates the relative arrival times of an event with no unphysical times. The time differences between detectors are feasible and consistent. In contrast figure 3.8b shows an event where the relative time recorded at hut T is unphysical and obviously unconnected with the other six huts. An algorithm was incorporated into the direction finding program to deal with such events. Five classes of unphysical times were treated:

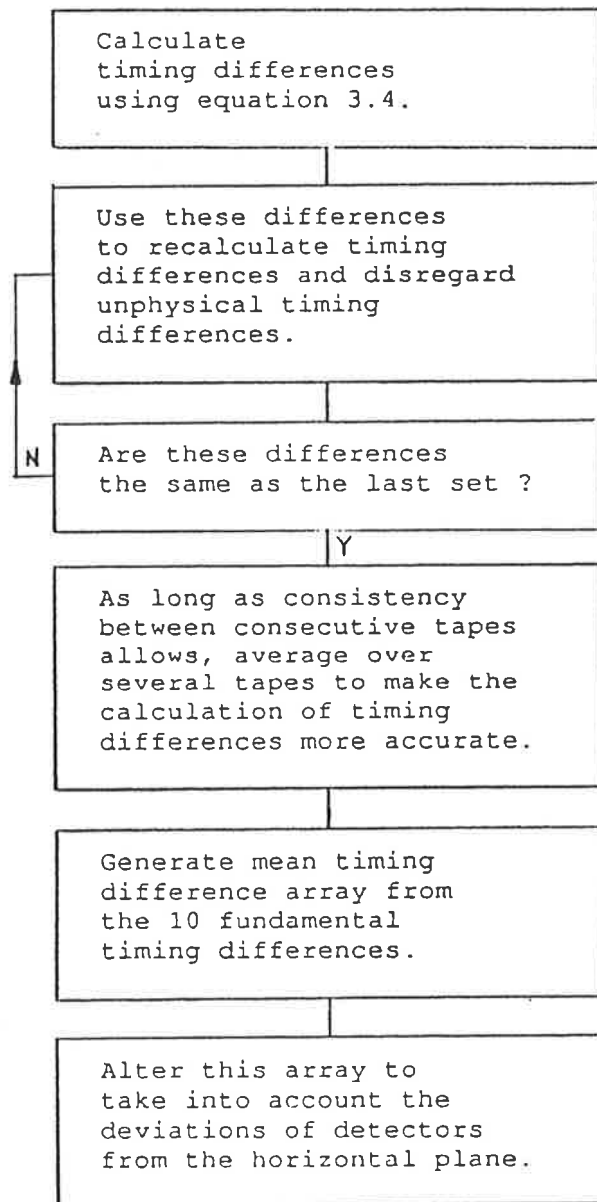


Figure 3.7 Flowchart indicating the stages in obtaining the final timing difference array used in directional analysis.

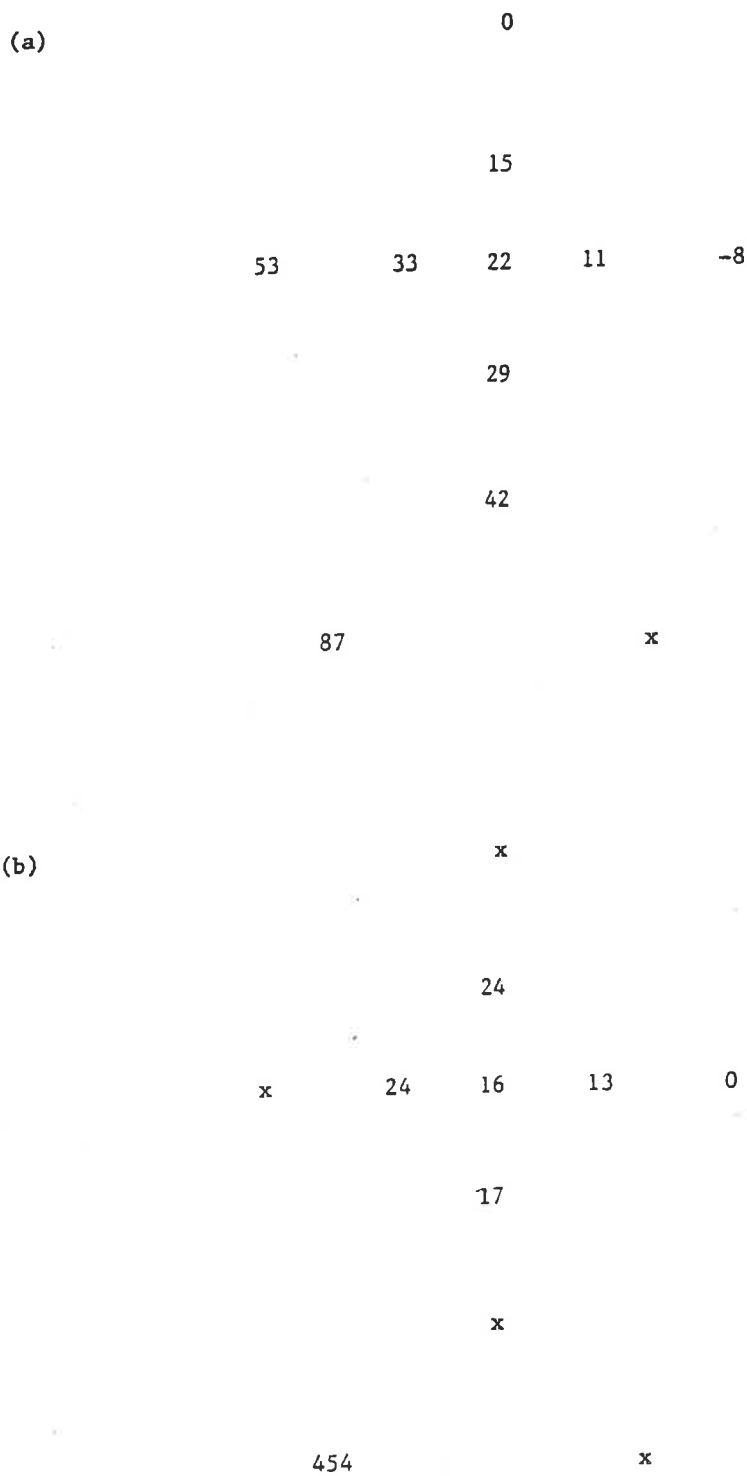


Figure 3.8

(a) An example of an event with no unphysical times. All times are relative to A Hut. S was not triggered by this event.

(b) An example of an event with an unphysical time. All times are relative to B. The time for hut T is not connected with the passage of the shower that triggered the other six detectors. An x denotes the hut was not triggered.

- (a) One detector has a time that is unphysical with respect to several other detectors. Figure 3.8b is an example of this. These events were treated by disregarding the unrelated time. A total of 2.98% of all analysed events fell into this category.
- (b) Two events have times that are unphysical with respect to several other detectors. An example of this would be if detector S had triggered with a relative time similar to that of T in Figure 3.8b. This category contained only 0.04% of all analysed events.
- (c) The relative time between only one pair of detectors was unphysical. Close inspection of each individual event would usually reveal which time should be disregarded, but this is obviously impractical, as although only 2.26% of all analysed events fell into this class, this corresponds to 87,000 events. The algorithm considered two trial events and, depending on the results of each trial event analysis, selected one time for deletion.
- (d) In the event that neither of the trial events in case (c) resulted in an analysable event - both times were discarded. This was also done if the deletion of both times gave a significantly better fit than the better of two trial events. Both times were deleted in only 0.10% of all events assigned directions.

(e) The last type of event was made up of events not fitting into any of the categories above. As only 0.08% of events fell into this category, they were treated simply by deleting every pair of detectors with an unphysical time difference - regardless of whether or not this action created an unanalysable event. The algorithm used to sort events with unphysical times and treat them accordingly is illustrated in Figure 3.9.

The directional analysis was performed by fitting a plane to the shower front, and iterating to take into account the offset of each detector from a horizontal plane. This procedure is described in Appendix A.

The results of checks made on the calculated directions to test their integrity are described in the following chapter.

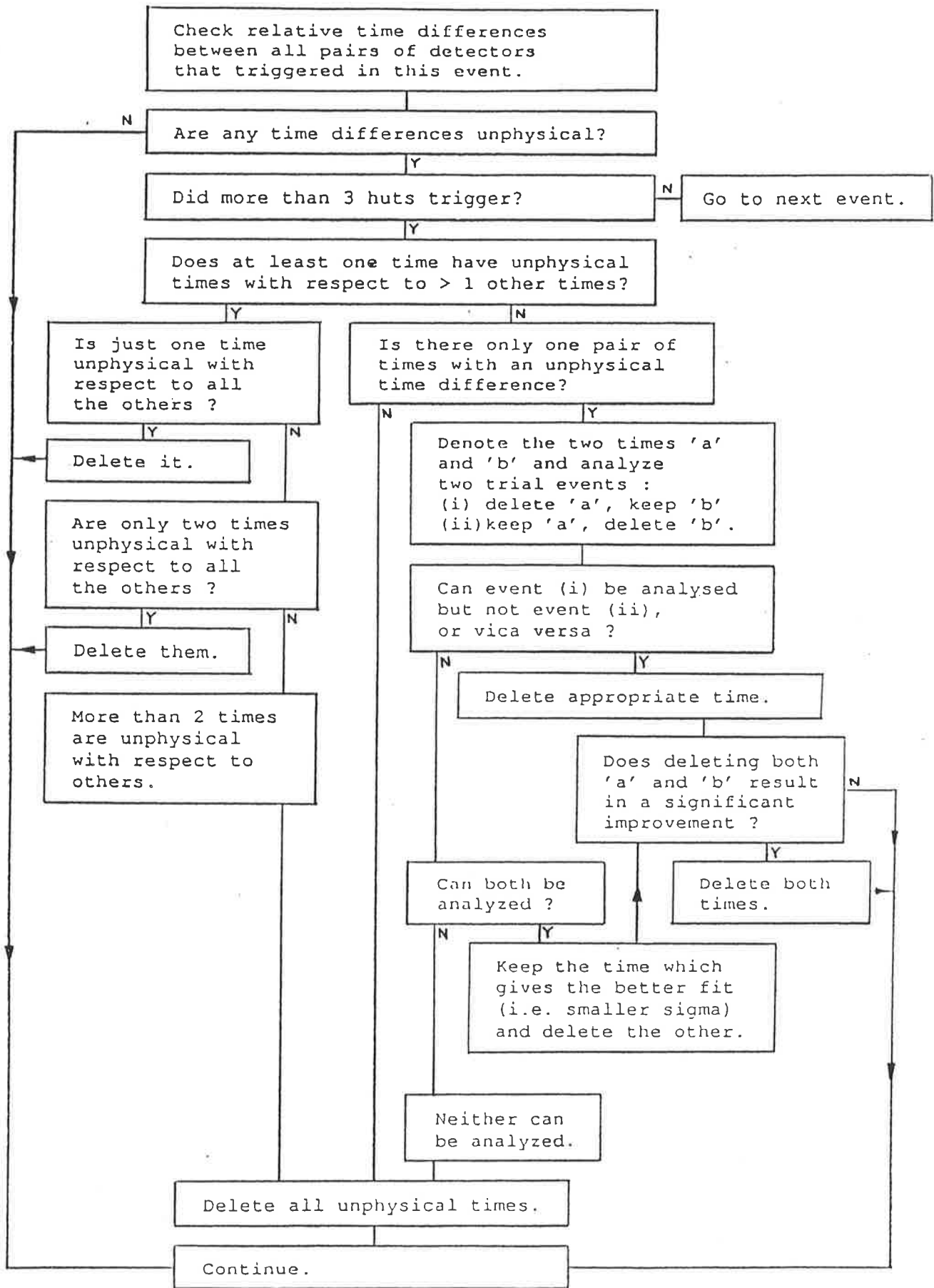


Figure 3.9 Flowchart indicating the algorithm used in classifying and treating events with unphysical times.

CHAPTER 4

BEHAVIOUR OF THE BUCKLAND PARK ARRAY

4.1 INTRODUCTION

In this chapter the behaviour of the array is considered. The quantities graphed not only provide a check that the array (and analysis programs) are behaving as expected, but also can be used to obtain information about the cosmic ray flux.

A total of 4.38×10^6 events were recorded between June 21, 1984 (JD 244 5872.6) and June 23, 1986 (JD 244 6604.6). Directions could be assigned to 3.87×10^6 events, corresponding to 88% of the total. Of those events that could not be assigned a direction, 60% (7% of the total) triggered only two fast-timing detectors, 25% (3%) triggered a collinear set of detectors and 15% (2%) were impossible to analyse.

4.2 THE ZENITH ANGLE DISTRIBUTION

The atmospheric thickness traversed by an EAS increases with zenith angle. The zenith angle distribution therefore reflects the way in which EAS are attenuated by the atmosphere. A plot of the number of events versus zenith angle is initially dominated by the increasing solid angle with zenith angle, as illustrated in Figure 4.1. The number of events per steradian is conventionally described by

$$\Phi(\theta) = \frac{dN(\theta)}{d\Omega} \propto \cos^n \theta \quad (4.1)$$

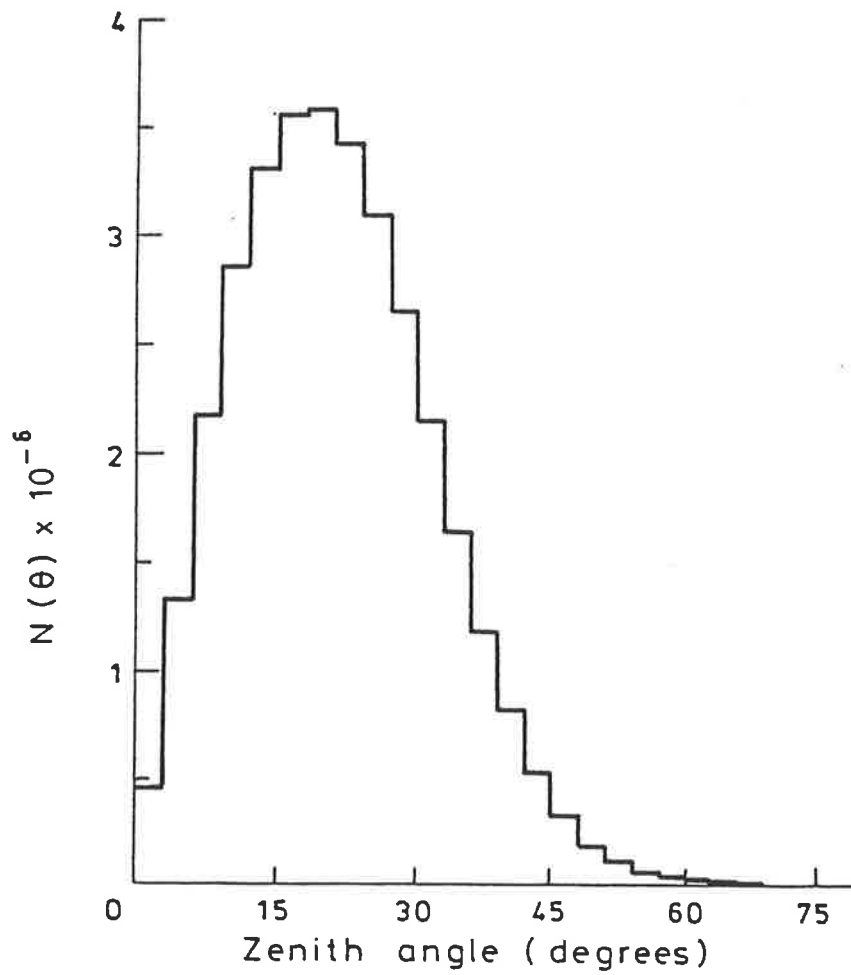


Figure 4.1.

The number of events per unit solid angle.

The value of n is dependent on the altitude of the observer, and also displays some zenith angle dependence. At sea level, n varies from 7.4 at 10° to 9.1 at 45° , but can be approximated by a constant value of 8.3 (Greisen 1956). Assuming this constant value we can convolve the decreasing flux with zenith angle with the increasing solid angle to find the theoretical mode of the zenith angle distribution.

$$\begin{aligned} \frac{d}{d\theta} (\cos^{8.3}\theta \ 2\pi \sin\theta) &= 0 \\ \Rightarrow \tan^2\theta &= \frac{1}{8.3} \\ \Rightarrow \theta &= 19.1^\circ \end{aligned}$$

Comparison with figure 4.1 shows that the agreement with the observed value of 18° is good.

Figure 4.2 shows the number per steradian as a function of zenith angle, with curves of $\text{Cos}^8\theta$ and $\text{Cos}^9\theta$ plotted for comparison. Behaviour similar to that described by Greisen (1956) is observed, as $\text{Cos}^8\theta$ provides a better fit at small zenith angles, whereas $\text{Cos}^9\theta$ gives a better fit at larger zenith angles.

An alternative representation is to plot $\log_{10}(\Phi(\theta))$ versus $\sec\theta$ (e.g. Kalmykov et al. 1973). Ciampa and Clay (1987) use this technique to obtain information on composition and shower development parameters. They performed Monte Carlo simulations of EAS detection with the Buckland Park array, and found the relationship between $\log_{10}(\Phi(\theta))$ and $\sec\theta$ was close to linear, but with a slope that varied as a function of primary composition,

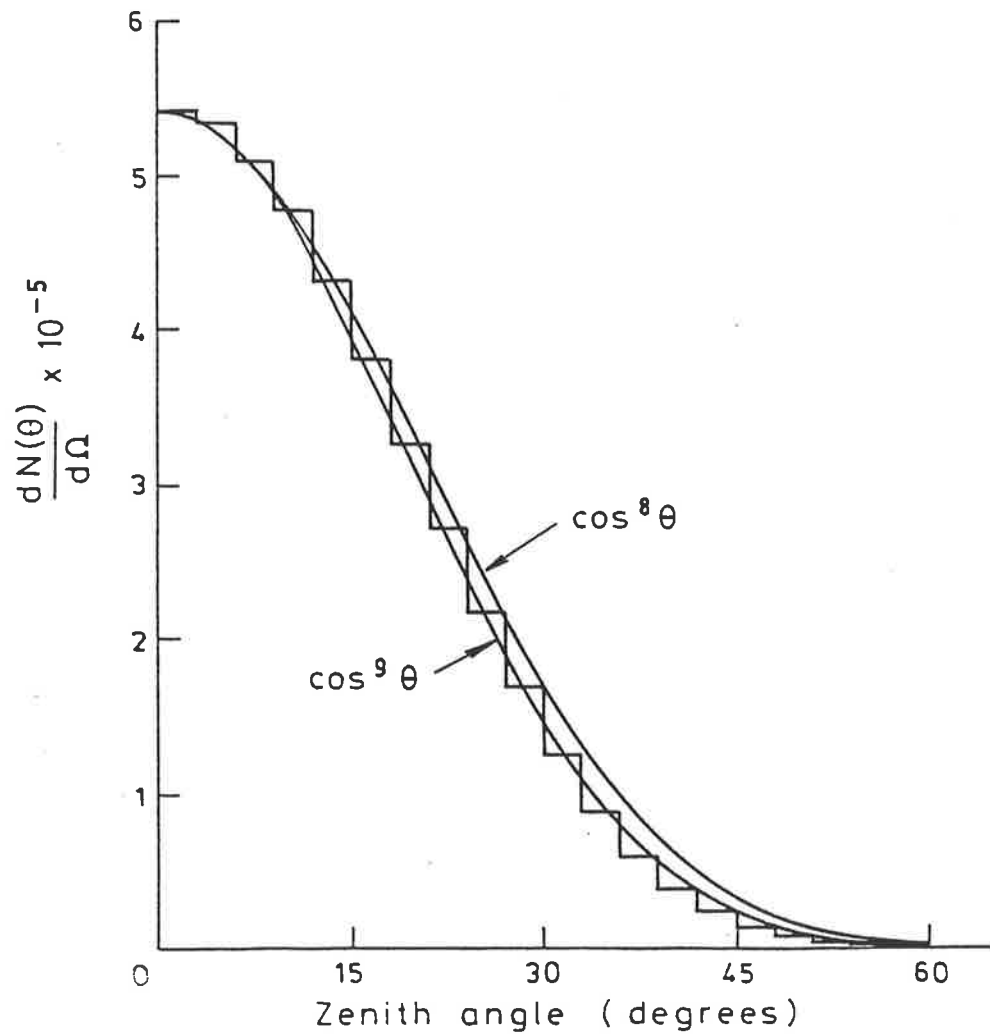


Figure 4.2 The zenith angle distribution of events triggering more than three fast-timing detectors. Curves of $\cos^8 \theta$ and $\cos^9 \theta$ are plotted for comparison (see text).

differential spectral index and EAS attenuation length. With an assumed spectral index of -2.5 and an attenuation length of 185 g cm^{-2} (Clay and Gerhardy 1982), proton initiated EAS resulted in a slope of -3.6 . Iron primaries produced a slope of -4.0 . Figure 4.3 illustrates the $\log_{10}(\Phi(\theta))$ versus $\sec\theta$ variation for the data collected in this experiment. The relationship can be fitted by a straight line until $\sec\theta \sim 1.3$. (corresponding to a zenith angle of $\sim 40^\circ$). The slope of the line is 3.73 ± 0.03 . This is interpreted as indicating a light (but not purely proton) composition at $\sim 10^{15}$ eV. This supports the conclusion of Ciampa and Clay (1987) and is in accordance with other composition studies (see section 1.2.3).

4.3 THE AZIMUTH ANGLE DISTRIBUTION

The azimuth angle distribution is shown in Figure 4.4. It is apparent that the distribution has a second-harmonic modulation, with an amplitude $\sim 3\%$ of the D.C. level. The maxima of the distribution correspond to a slight predominance of showers from the north and south over showers incident from the east and west. A similar effect was noted in the 1979-1981 data set with an amplitude of $\sim 4\%$ (Gerhardy 1983), suggesting the effect is due to the asymmetry of the array. The array is symmetric about a north-south line, and it is also noted that the both fast-system and slow-system triggering detectors extend slightly further in the north-south direction than the east-west direction (see Figure 3.1).

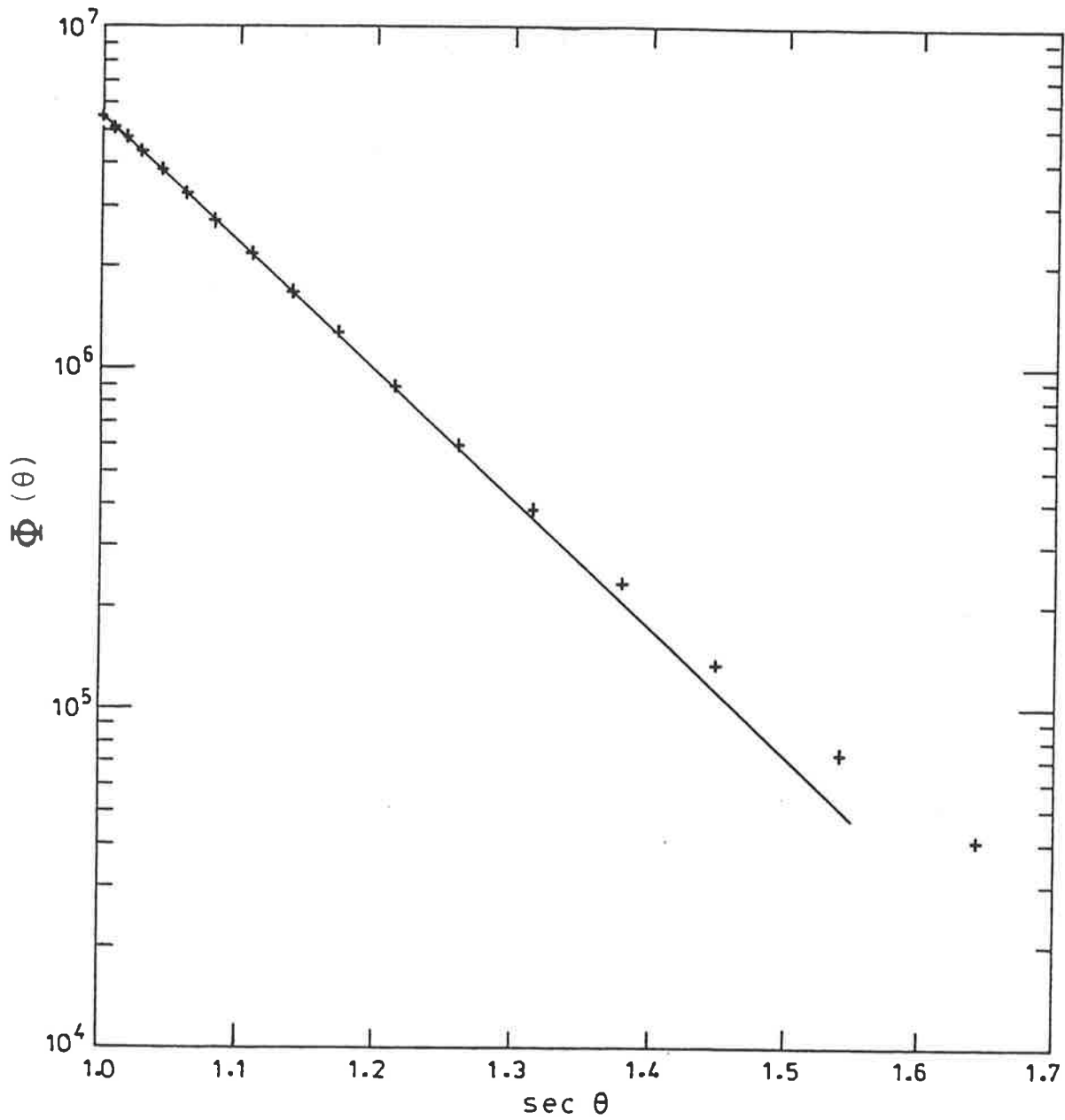


Figure 4.3 The logarithm of $\Phi(\theta)$ as a function of $\sec(\theta)$. The relationship is linear until $\sec \theta \sim 1.3$.

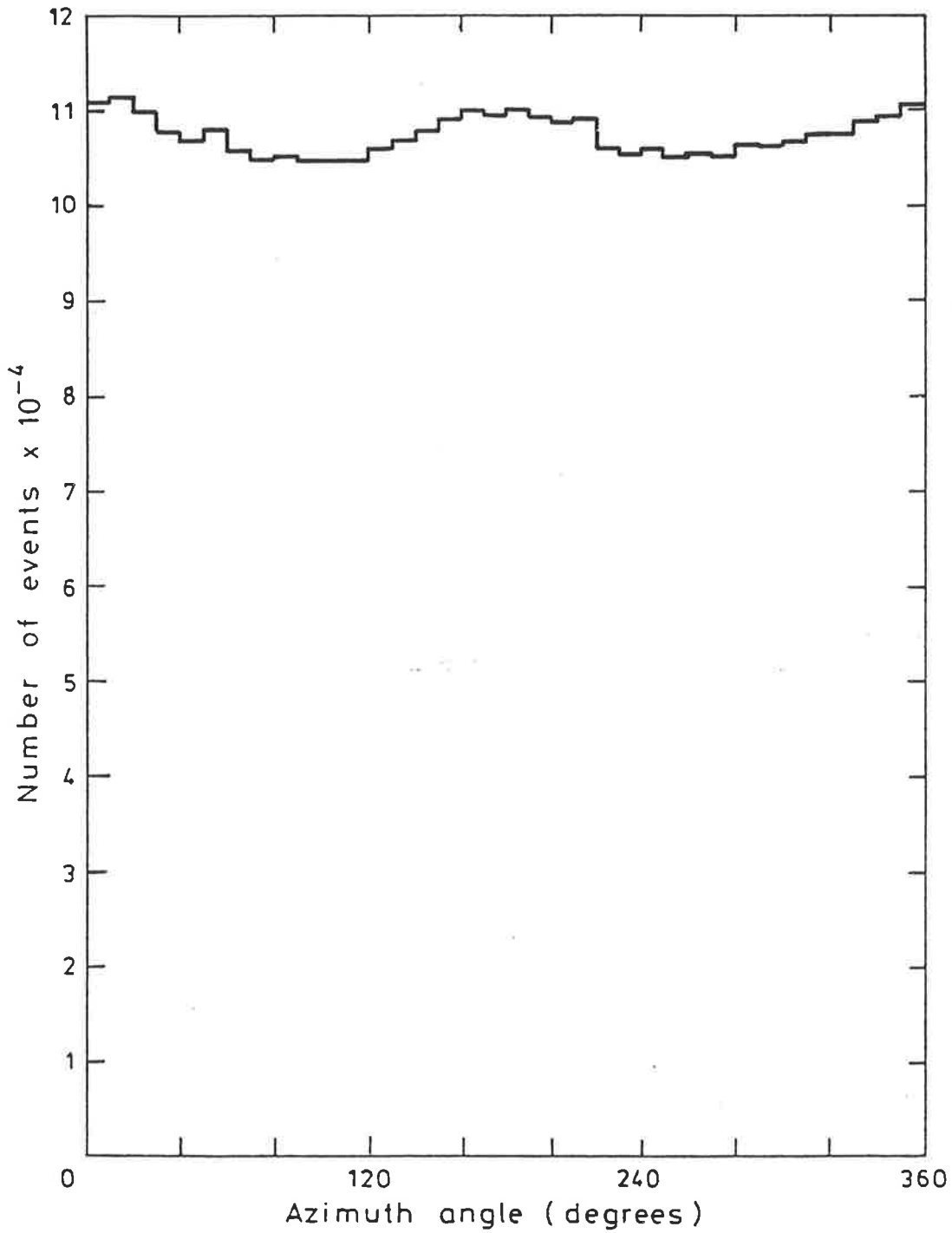


figure 4.4 The azimuth angle distribution. See text for a discussion of the second harmonic evident in the distribution.

4.4 ARRAY EXPOSURE IN SIDEREAL TIME

Over the two year period, data was collected for 555.6 days, which corresponds to an efficiency of 76%. The largest contribution to the off-time was due to interruptions to the power supply at Buckland Park. These required a trip to Buckland Park, usually a day or two later, to reset and restart the array. Equipment breakdown added to the off-time, as did several instances where the array was shut off while modifications and improvements were made. The cumulative effect on the sidereal time exposure of the array over a two year period is expected to be small, and this is found to be the case. Figure 4.5 shows the array exposure in sidereal time, with only small departures from the mean value.

4.5 THE NUMBER OF FAST-TIMING DETECTORS TRIGGERED

In the analysis of data collected over the two year period no size, age or core position determinations have been attempted. This is partly due to unresolved problems in core-fitting, particularly for smaller showers, which are discussed by Corani (1986). The main reason, however, is simply that with the forty-fold increase in the data collection rate over the 1979-1981 data set, computer analysis has become a bottleneck. A delay of several months was enforced when the University replaced its existing CYBER computer with the current VAX. This, coupled with unavoidable memory space and analysis-time limitations, has meant a complete analysis for every event is impractical during the author's candidature.

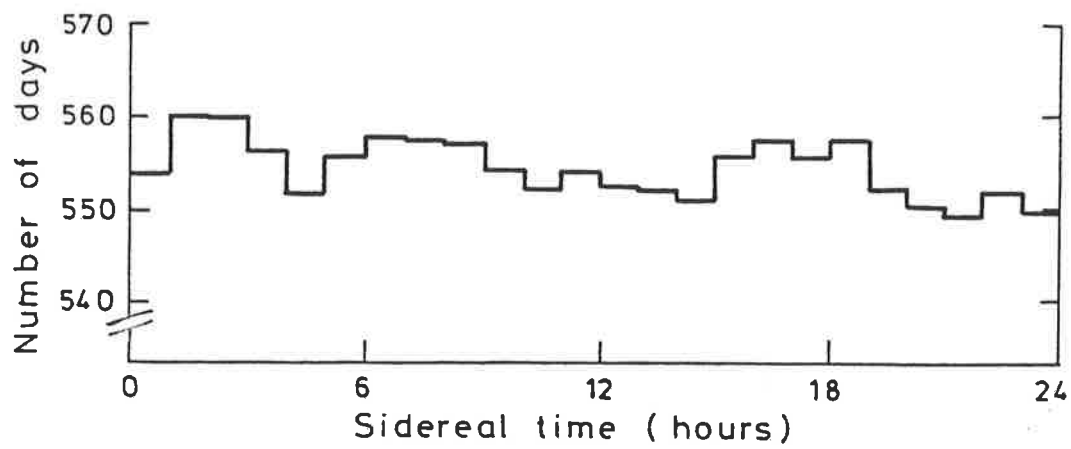


Figure 4.5. Array exposure in sidereal time.

As a result, no energy or shower size cuts were able to be made to the data. As a cut of this nature is desirable, to allow a more direct comparison with the results of other experiments, an approximate shower size cut using the number of fast-timing detectors triggered in each event was used. This distribution is illustrated in Figure 4.6, and is of the form expected. Small showers with limited lateral extent, will trigger a small number of detectors. As primary energy, and therefore shower size, increase, so does the lateral extent of the shower, and therefore the effective collecting area of the array. Also, at low shower energies near the array threshold, showers developing later in the atmosphere are preferentially detected. Thus whilst these showers are more frequent at the top of the atmosphere, a smaller percentage of them are detected by the array in comparison to higher energy showers.

The steeply falling cosmic-ray energy spectrum results in less events triggering higher numbers of fast-timing detectors, and the subsequent falling off of the distribution. The approximate energy corresponding to these cuts was calculated by comparing the shower rate with that of the 1979-1981 data set, and assuming the array collecting area is the same.

This assumption requires further examination. As a full analysis of each event was performed for the 1979-1981 data set, events with core locations outside the boundary of the array were discarded. As no core fitting has been possible with the present data, this has obviously not been possible. This is of particular

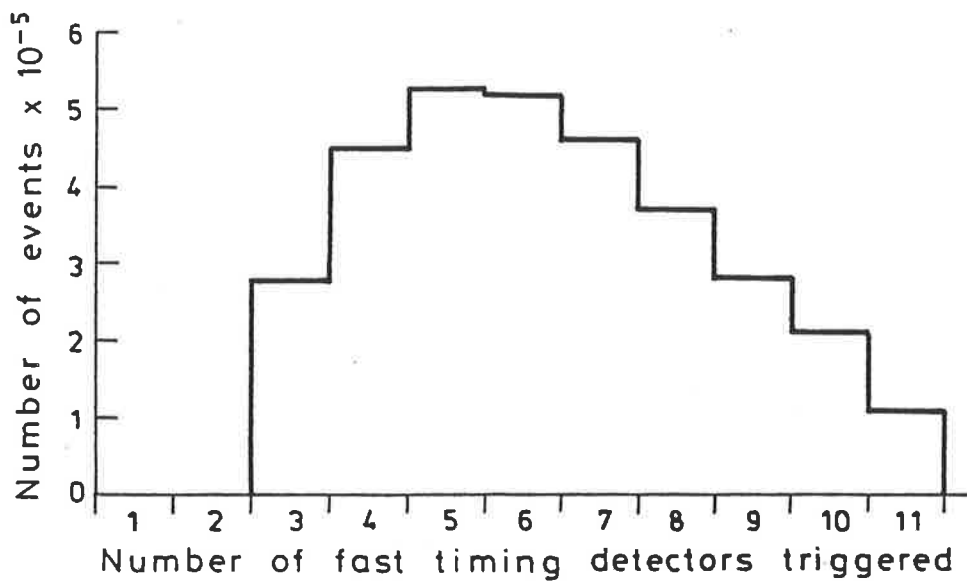


Figure 4.6. The distribution of the number of fast-timing detectors triggered for events that could be assigned a direction.

significance for higher energy events, as the increased lateral extent of these showers allow a shower with a core position outside the array boundary to trigger the array. However, as the cosmic-ray energy-spectrum falls steeply with energy (and more steeply at energies above the knee than for lower energies) the overall contribution to the event rate from these showers is believed to be small.

The analysis described in Chapter 5 makes use of three cuts in this distribution. The corresponding energy thresholds given below can only be considered as approximate, although sufficient for the purposes of this experiment. The three cuts are

- (a) Events triggering 9, 10 or 11 fast-timing detectors. This corresponds to 19% of all events assigned a direction, and an approximate energy threshold of 9×10^{14} eV. From the arguments above, this threshold may err by being slightly low.
- (b) Events triggering 7 or 8 fast-timing detectors. This group contains 26% of events assigned directions, and corresponds to an approximate energy threshold of 5×10^{15} eV.
- (c) Events triggering 4, 5 or 6 fast-timing detectors. Forty-six percent of analysed events fell into this category, and the corresponding energy threshold is considered to be approximately 3×10^{14} eV. This figure is probably slightly high. As these are

lower energy showers, the effective array collecting area for these events is probably less than the collecting area of the 1979-1981 data set. However, the energy threshold for this cut is not required in any further calculations, and is given here only as an indication of the array's capacity.

Events triggering only three detectors were not used in the current analysis. As there is no redundant timing information, no indication of the accuracy of the fit is available (see section 4.6). The cuts in the distribution of fast-timing detectors triggered are discussed further in section 4.8.

4.6 GOODNESS OF FIT DISTRIBUTION

The planar fit to the shower front is characterised by a goodness of fit parameter, σ , defined by

$$\sigma = \sqrt{\frac{\sum_{i=1}^N (T_o - T_f)^2}{N - 3}} \quad (4.2)$$

where T_o = observed time

T_f = fitted time

N = number of detectors triggered.

This is effectively the standard deviation of the observed times and is measured in nanoseconds. Obviously N must be greater than three for σ to be defined. A plane is uniquely defined by three non-collinear points and a fourth is required before a standard deviation has any meaning. Figure 4.7 illustrates the goodness of fit distribution. The distribution has a mode of ~ 2.75 and a mean

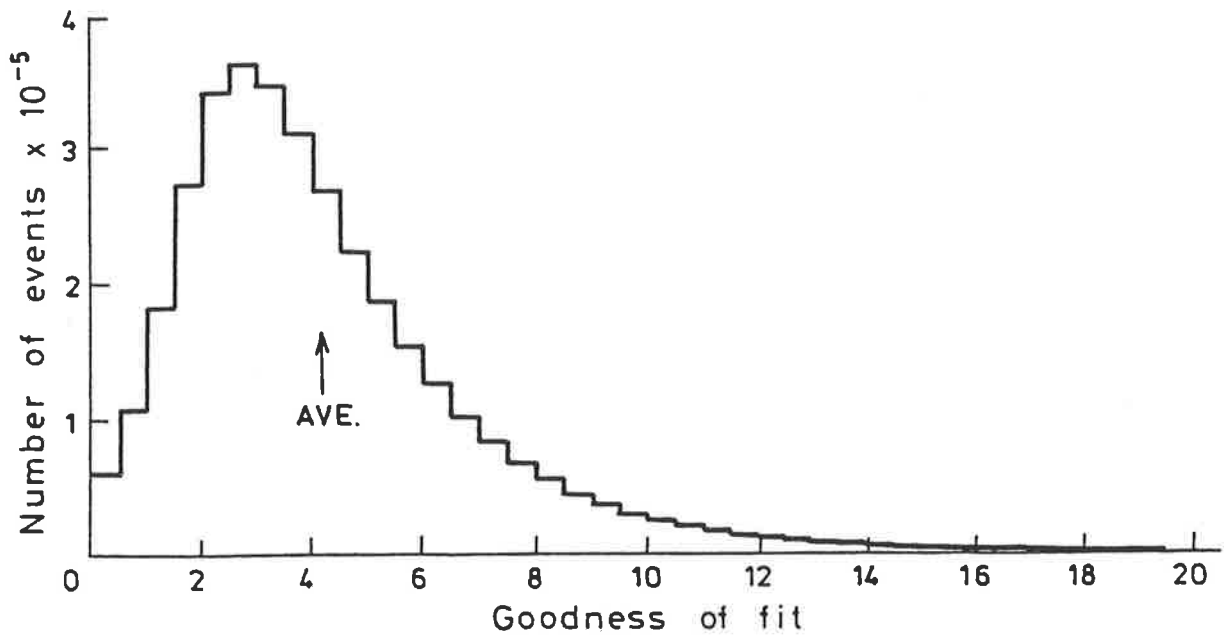


Figure 4.7 The distribution of the goodness of fit parameter from directional analysis.

of ~ 4.2 . The mean is significantly greater than the mode due to the long tail of the distribution. Although all unphysical times are deleted before directional analysis, there remains the possibility that an uncorrelated, but physically feasible, time (or times) will occur in a smaller proportion of events. The presence of such a time will increase the standard deviation of the observed times about the fitted plane, resulting in a larger value of σ . Such events are undoubtedly the main cause of the long tail of the distribution. As directions assigned to these events will be incorrect, the use of a σ -cut when selecting showers from potential gamma-ray sources is imperative. The adopted selection of only events with $\sigma < 6$ resulted in $\sim 20\%$ of events with more than three fast-timing detectors triggered being discarded. Gerhardy (1983) found that events with $\sigma \sim 6$ had angular uncertainties of the order of 2° , i.e. of the same order as the acceptance angle used in Chapter 5.

4.7 TIMING OFFSET DISTRIBUTION

As mentioned previously, a free variable, t_0 , is used in fitting the planar shower front to the observed times. This is used so that the shower front is not constrained to pass through the "reference" detector, i.e. the detector relative to which all other times are made. The distribution is shown in Figure 4.8. A tendency for negative values of t_0 is apparent. Forty percent of events have $t_0 < 0.5$, whereas 31% have $t_0 > 0.5$. The negative value of t_0 means that the reference detector triggered after the plane of best fit. This implies that the "reference" detector, which varies depending on which huts are triggered, is more likely

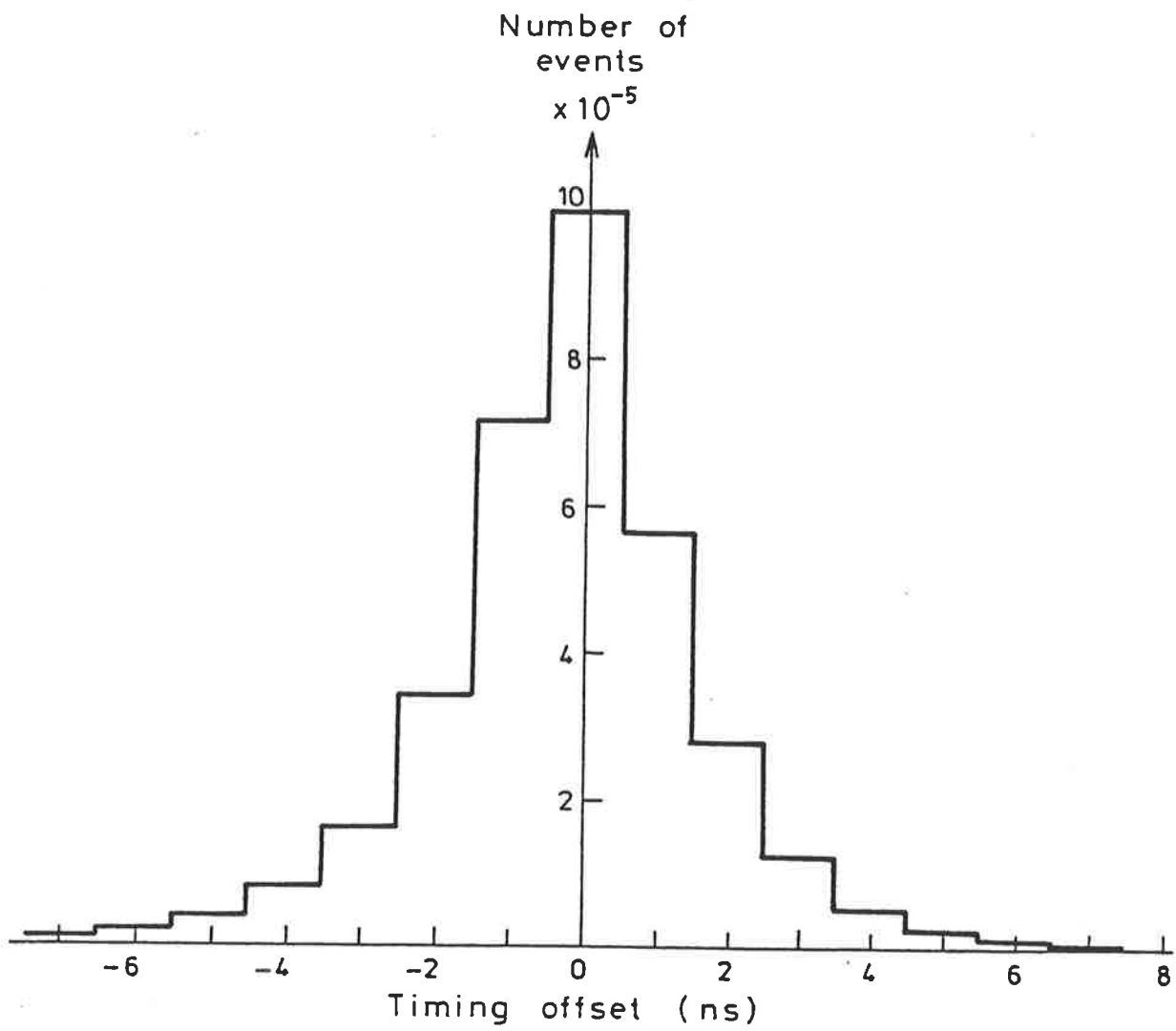


Figure 4.8. The distribution of the timing offset. A slight bias towards negative values is present.

to be triggered by a particle slightly behind the shower front. The large tail on the distribution is (as for the goodness of fit distribution) presumably caused by those events with physical but uncorrelated times, causing a distortion to the fitted plane and a larger timing offset from the reference detector. This was checked by plotting the average value of the goodness of fit for each timing offset. Figure 4.9 confirms that the two are closely correlated and appear linearly dependent. It is interesting to note that the constant of proportionality is larger for positive values of the timing offset than it is for negative values. The reason for this is not known.

4.8 ANGULAR RESOLUTION

The angular resolution of the Buckland Park array during 1979-1981 was well-defined. Only five timing detectors were used (A, B, C, D and E) and for an event to be recorded all five detectors were required to trigger. Thus the baseline of the array was fixed and constant. Protheroe and Clay (1984) used the redundant timing information available from three equally spaced collinear detectors to derive an rms timing uncertainty for each detector of ~ 2.2 ns. This allowed the angular resolution to be calculated as a function of zenith angle. Knowing the angular resolution, the optimum resolution angle for a gamma-ray source was calculated. The maximum signal to noise was found for a resolution angle in which 72% of gamma-rays would be expected to arrive.

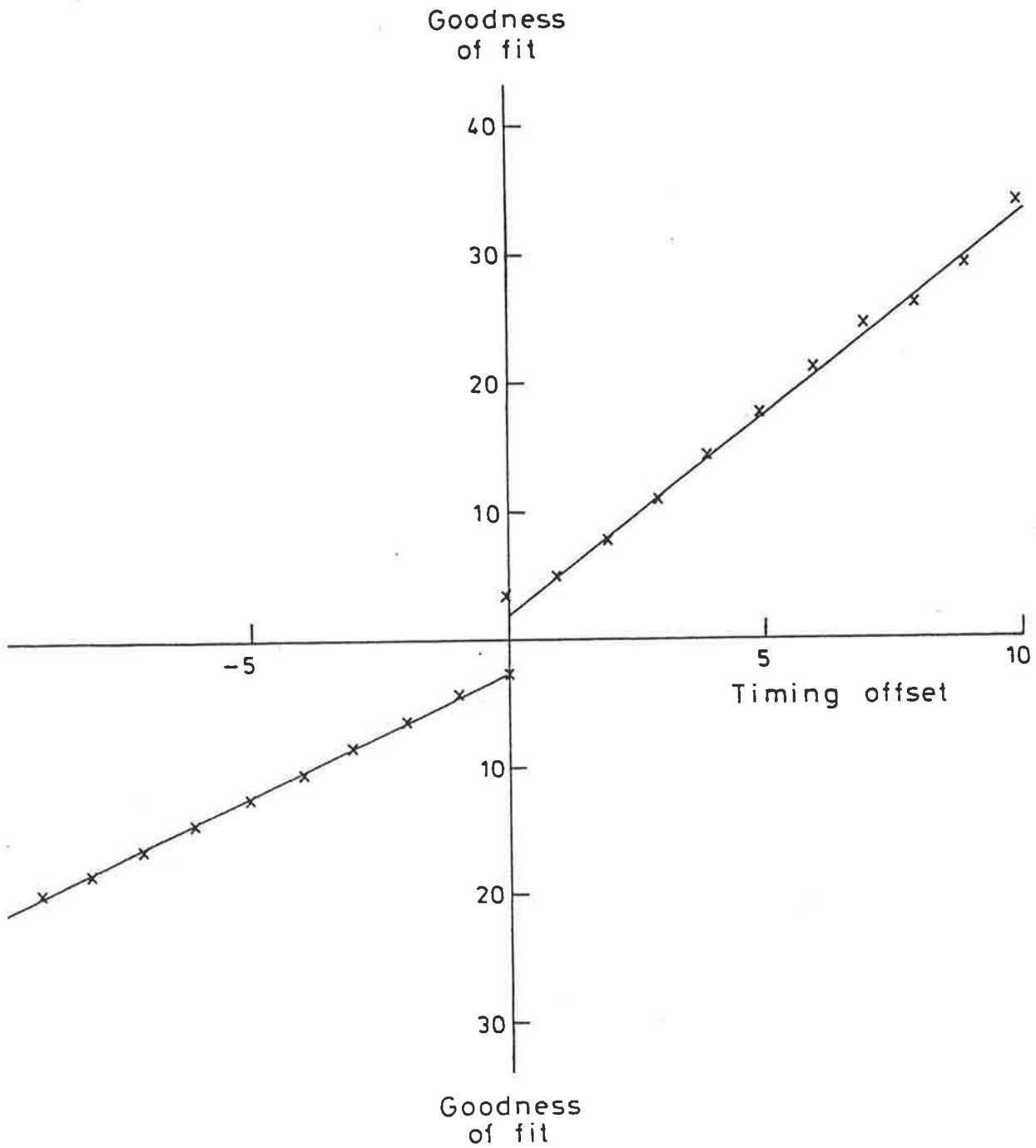


figure 4.9 The average goodness of fit as a function of the timing offset. There is a well-defined relationship between the two, as expected, although the gradient differs for positive and negative timing offset values.

A similar procedure was adopted for the new array by Ciampa et al. (1986). The angular resolution for events triggering all eleven (fast-timing) detectors is marginally better than for the 1979-1981 array. For events only triggering the five central 2.25 m² detectors (A1, B1, C, D1, E1) the angular resolution is markedly worse (see Figure 4.10). This is due mainly to the substantially reduced baseline.

With the much looser triggering criterion of the new array, an analysable event may have as few as three or as many as eleven fast-timing detectors triggered. Thus, the maximum baseline (i.e. distance between detectors furthest apart) will range from 12m to 58m. The angular resolution, and hence resolution angle, will depend on the configuration of triggered detectors. Whilst it would be possible to calculate the optimum resolution angle for every possible configuration of triggered detectors it was decided to adopt a more pragmatic approach.

In the initial search for gamma-ray emission from various sources only events triggering nine, ten or eleven detectors were used. The reasons for this are threefold.

Firstly, events triggering nine or more detectors will have angular resolutions closest to the angular resolution of the 1979 array. The two fast-timing detectors most distant from the centre of the array, S and T are observed to trigger less frequently than the central nine. Secondly, events triggering nine or more

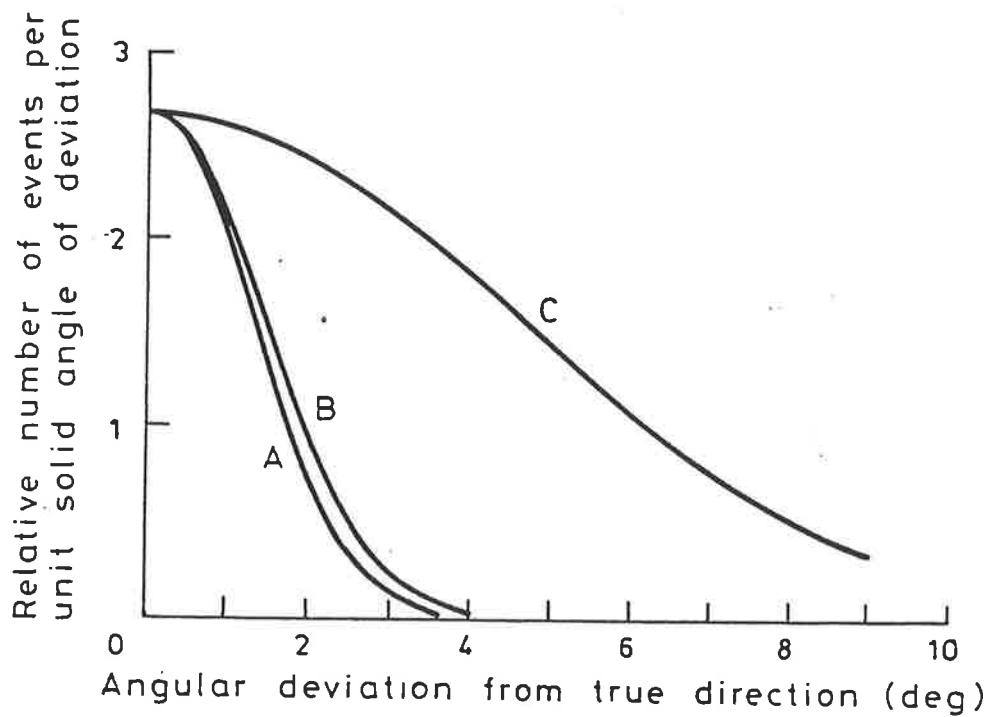


Figure 4.10 (a) The angular resolution of the 1978-1981 array configuration (b) compared to the angular resolution for events triggering all eleven detectors of the current array (c) and events triggering only the five central 2.25 m^2 detectors. The much smaller baseline and use of light baffles in the detectors for the last case contribute to the significantly worse angular resolution. (From Ciampa et al. 1986)

detectors will, in general, be events with larger sea-level sizes, and therefore higher primary energies. This allows a closer comparison with previous results. Finally, the rate of events triggering nine or more detectors will be relatively unaltered during the periods where one (or very occasionally, two) fast-timing detectors were not functioning.

CHAPTER 5

SEARCH FOR ULTRA-HIGH-ENERGY GAMMA-RAY EMISSION FROM BINARY X-RAY SOURCES

The properties of binary x-ray sources will be briefly reviewed, and the results for searches for UHE emission from six such sources presented.

5.1 BINARY X-RAY SYSTEMS

Binary x-ray systems consist of a compact object (generally a neutron star) and a stellar companion (sometimes referred to as the primary) in orbit about the centre of mass of the system. These systems are commonly divided into two classifications depending on the mass of the stellar companion (e.g. Bradt and McClintock 1983).

The stellar companions of massive systems are generally bright, young (O or B type) stars, with masses $> 1M_{\odot}$ where M_{\odot} is the solar mass. Low mass systems are designated as those with the mass of the stellar companion $< 1M_{\odot}$. In both systems, matter is accreted from the primary by the neutron star.

In "wind driven" systems, matter is accreted from the radiation driven stellar wind of the primary, which has a large

velocity compared with the orbital velocity. In this case a small fraction of the mass of the stellar wind is gravitationally attracted by the neutron star. The x-rays produced by the infall of this plasma have a significant effect on the stellar wind of the primary. Ho and Arons (1987) find this x-ray "feedback" on the stellar wind can result in a variety of luminosity solutions for the binary system. Their success in modelling both high luminosity sources such as Cen X-3 ($L_x \sim 1.5 \times 10^4 L_o$), and low luminosity sources such as Vela X-1 ($L_x \sim 2.3 \times 10^2 L_o$), lead them to conclude that the ionization feedback of x-rays on the stellar wind is the dominant effect controlling mass transfer in these systems.

In other systems the companion star approximately fills its Roche lobe allowing gas to escape near the inner Lagrangian point (or saddle point) and flow toward the neutron star. The angular momentum of the gas causes it to orbit the neutron star. The gas loses energy in collisions and slowly spirals inward, forming a large optically thick disk, known as the accretion disk.

In massive systems, the optical appearance of the system is dominated by the intrinsic light of the companion. The ratio of x-ray to optical luminosities is generally in the range

$$10^{-5} < \frac{L_x}{L_{opt}} < 10.$$

In contrast, low mass systems are characterised by luminosity ratios

$$10 < \frac{L_x}{L_{opt}} < 10^4.$$

Many optical counterparts of low mass binary systems were discovered by their ultraviolet excess relative to normal stars.

The optical spectra of low mass systems are found to contain high excitation emission lines superimposed on a predominantly blue optical continuum, suggesting that the optical emission is dominated by reprocessed x-rays (e.g. Bradt and McClintock 1983). Thus the accretion disk is probably the dominant source of light in most low mass systems. It is inferred from this that, in this case, the companion is a low mass, optically faint, dwarf star. A comparison of a high mass and a low mass binary system is made in Figure 5.1.

In the following sections, six sources are examined for evidence of periodic emission UHE gamma-rays. Three of the sources are massive systems, and three are low mass systems. Figure 5.2 illustrates the relative size of the systems, with the exception of Cir X-1.

In searching for UHE gamma-ray emission, the Z_{10}^2 test (Buccheri 1985) is used. Like the Protheroe test (Protheroe 1985), it is a powerful test for narrow peaks in the light curve. The advantage of the Z_{10}^2 test in the present case is that its behaviour for large numbers of events is well-known, whereas the Protheroe test is documented for data sets with less than two hundred events. For this reason the Protheroe test is only used in this thesis in the analysis of data from the smaller 1979-1981 data set.

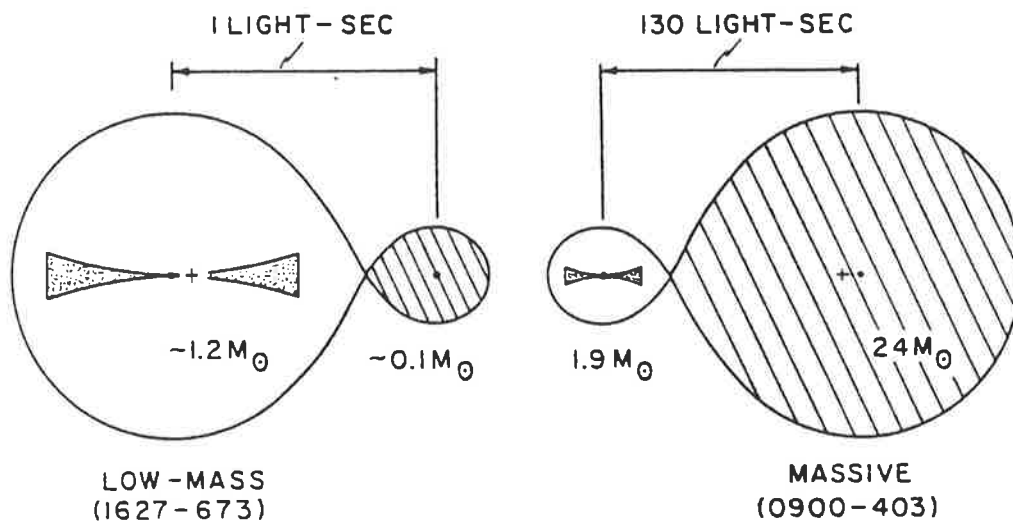


Figure 5.1. Comparison of a low-mass and a massive x-ray binary system. In both cases the (cross-hatched) optical companion, or primary, is shown filling its critical Roche equipotential lobe. The accretion disks of the neutron stars are shown as stippled regions, although the detailed geometries of the disks are not known. A dot marks the centre of mass of each star, and a cross marks the centre of mass of each system. (From Bradt and McClintock (1983)).

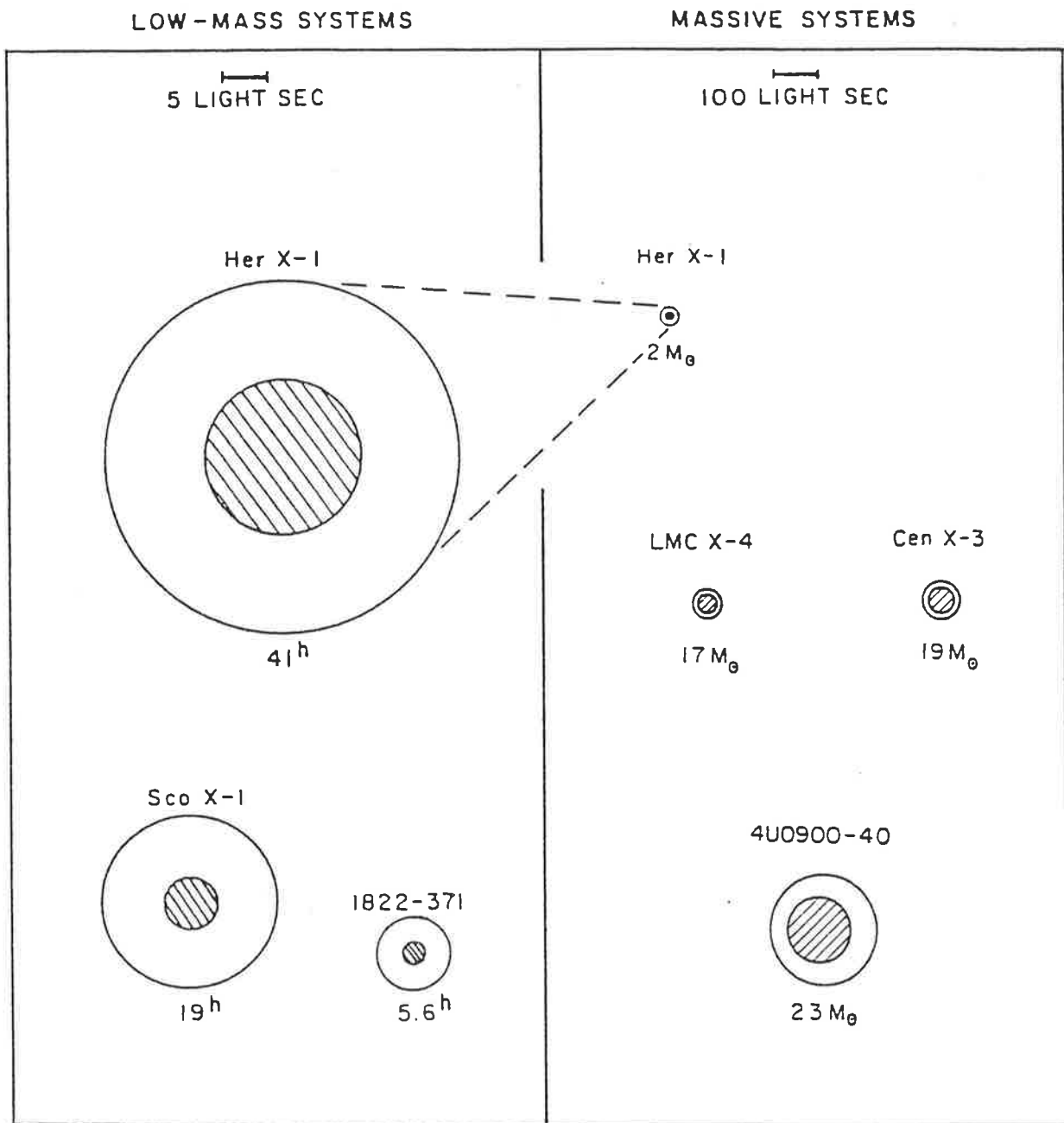


Figure 5.2. The classification and geometries of five of the six objects discussed in this chapter, with Her X-1 included for comparison. Cir X-1 is not shown as its geometry is not yet known. (Adapted from Bradt and McClintock (1983)). and Joss and Rappaport (1984)).

5.2 SEARCH FOR ULTRA-HIGH-ENERGY GAMMA-RAY EMISSION

FROM BINARY X-RAY SYSTEMS

5.2.1 VELA X-1

Vela X-1 (also identified as 3U0900-40) was discovered in rocket x-ray observations (see Chodil et al. 1967). Its binary nature was established by OSO-7 satellite observations which revealed an eclipsing binary with an orbital period of ~ 9 days (Ulmer et al. 1972). Uhuru satellite observations led to the identification of Vela X-1 with HD77581 (Hiltner et al. 1972), a B0 supergiant, which allowed optical measurements of the period and other orbital parameters to be made. The SAS-3 satellite revealed x-ray pulsations from Vela X-1 with a period of ~ 283 s (McClintock et al. 1976). Vela X-1 is observed to vary on time scales from seconds to days, with variability within each 283s cycle and also from cycle to cycle. Vela X-1 was not detected by the SAS-II or COS-B gamma-ray telescopes, although its proximity to the Vela pulsar, the brightest object in the sky at 100 MeV energies, does not rule out the possibility of it being a weak 100 MeV gamma-ray source.

Vela X-1 was detected at PeV energies with the Buckland Park array (Protheroe et al. 1984). An age cut was applied to the data to accept only showers with $s > 1.3$, arriving within a resolution cone of half angle 2° . Data from the three year period 1979-1981 were binned using the ephemeris of Nagase et al. (see Hayakawa

1981). An excess of events was discovered in the phase bin centred on $\phi = 0.63$, leading to a calculated luminosity ~ 0.01 that of Cyg X-3. The observation had a 0.01% probability of being due to a statistical fluctuation.

The BASJE (Bolivian Air Shower Joint Experiment) collaboration searched their data recorded during 1962-1967 for evidence of UHE gamma-ray emission from Vela X-1 (Suga et al. 1985). Both a muon-poor requirement and an age cut to select showers with $s \geq 1.0$ were employed to enhance any possible gamma-ray signal. An excess was seen at a phase of ~ 0.5 , though the large time difference between BASJE and Buckland Park observations does not allow a direct comparison of phase. The significance of the excess was $\sim 2\%$.

The Potchefstroom group in South Africa has also reported a detection of Vela X-1 with data recorded from 1979-1981 (van der Walt et al. 1987). Events from a $10^\circ \times 10^\circ$ box centred on Vela X-1 with $s > 1.3$ were analysed using the ephemeris of Nagase et al. The phase analysis revealed a peak, although at a phase of 0.13 - significantly different from the contemporaneous data of Protheroe et al. Van der Walt et al. claim a confidence level of 98.2%.

The Potchefstroom group has more recently observed Vela X-1 at TeV energies, and detected gamma-rays pulsed with the 283 s pulsar period (North et al. 1987). Observations were made on eleven nights during the period April 2, 1986 to May 10, 1986 using a gamma-ray telescope to detect showers above a threshold

energy of 1 TeV. The pulsed TeV light curve was approximately sinusoidal, and had a period of 282.805s, consistent with x-ray observations. The probability for a chance origin of the emission was calculated to be 7×10^{-4} . An isolated outburst was also observed from Vela X-1 during this period, on May 4, 1986. The outburst lasted 24 minutes, and in the first minute consisted of a 5.7σ deviation from the mean count rate. The outburst was also modulated with the 282.805s period, and was calculated to have a probability of 1.1×10^{-5} of being due to chance.

In searching for a simple explanation of the anomalous features of showers "produced by radiation from Cyg X-3 and other sources", Hillas (1987a) notes it is remotely possible that the claimed signals were all observed at large zenith angles, and that the age cuts employed may be effectively a zenith angle cut. This suggestion was examined with the 1979-1981 Buckland Park data set. Figure 5.3 shows the zenith angles of the events from the enhanced phases for Vela X-1 and LMC X-4, compared to the zenith angle distribution from off-source events in the same declination band. In both cases the zenith angles of events presumed to be due to gamma-rays are consistent with the background distribution. This possible explanation for the unexpected features of gamma-ray showers therefore appears unlikely.

The arrival times of the events at the enhanced phases for Vela X-1 and LMC X-4 were also examined. No tendency was observed for the events to arrive in a burst, or short period of time. In both cases the emission appears relatively constant over the three year period. (In the case of Vela X-1 a modulation is introduced by the proximity of the orbital period to 9 sidereal days.)

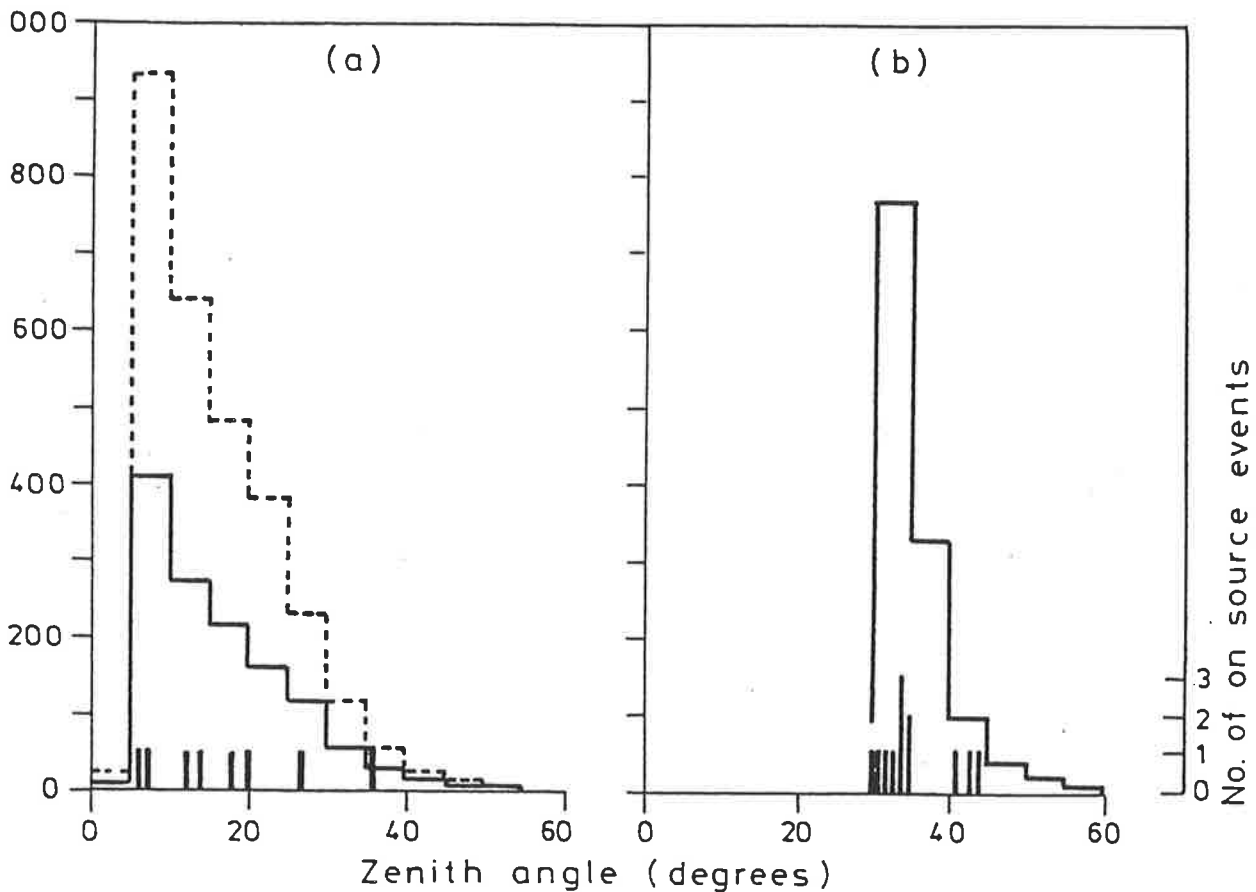


Figure 5.3. The zenith angle distributions of events from the enhanced phases of (a) Vela X-1 and (b) LMC X-4, compared with the zenith angle distributions for off-source events from the same declination band. In the case of Vela X-1, the dotted line includes all events, whereas the full line is for events with $s > 1.3$. Events of all ages were used in the case of LMC X-4. In both cases the zenith angle distribution of events attributed to gamma-rays does not appear to differ significantly from the background distribution.

The data collected in this experiment was then searched for evidence of ultra-high energy gamma-ray emission from Vela X-1. As for all sources considered in this chapter, a barycentric correction was first made to event arrival times. Following Protheroe et al. (1984), events in the present data set from within 2° of Vela X-1 were binned according to phase. As the orbital period of Vela X-1 is very close to nine sidereal days, fifty-four phase bins (the multiple of nine closest to the fifty bins of Protheroe et al. (1984)) were used in order to facilitate comparison of the on-source distribution with the background. In order to obtain the best estimate of the variation of the background with phase, 67 off-source circles from the same declination band were averaged. The ephemeris of Deeter et al. (1987) was adopted. Over the two years of this experiment it differs in phase from the ephemeris of Nagase et al. employed in previous analyses by less than ~ 0.1 (Protheroe 1987c).

Figure 5.4 shows the resulting phase distribution. No significant excess is seen at any of the phases reported previously, or at any other phase. No evidence for emission of UHE gamma-rays is found. Unlike all three previous observations, no use was made of an age cut.

The TeV observations of the 283 s pulse period of Vela X-1 (North et al. 1987) were made while this experiment was in progress. Events from Vela X-1 between 3rd April to 13th May were divided into three classes, those triggering (a) nine or more,

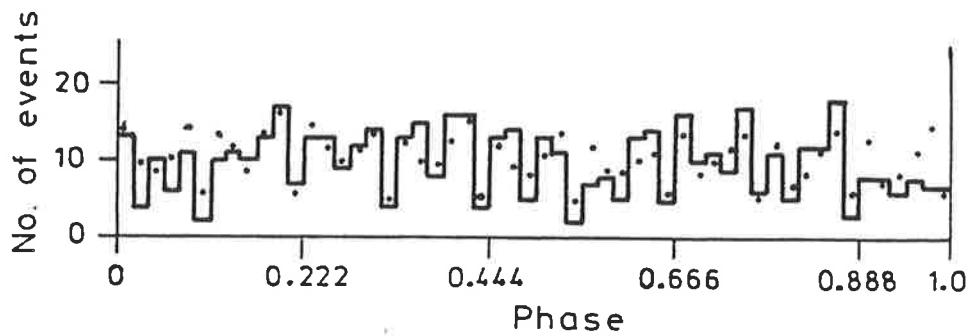


Figure 5.4. The phase distribution of events from the direction of Vela X-1. The dot in each bin corresponds to the average off-source value. The ephemeris of Deeter et al. (1987) is used. Fifty four bins are used, as this is an even multiple of nine and the orbital period of Vela X-1 is very close to nine sidereal days. No evidence for emission is found.

(b) seven or eight, and (c) four, five or six fast timing detectors. Events from within 2° of Vela X-1 were accepted for (a) and (b), although this was relaxed to 3° for (c), as the angular resolution for these events is not expected to be as good.

As the light curve obtained by North et al. was approximately sinusoidal, the Z_2^2 test was used as it is a more powerful test for sinusoidal-type light curves.

At the time of the outburst of 4th May, the zenith angle of Vela X-1 from Buckland Park was 88° . No events are therefore expected (or seen) to coincide with this burst. The period surrounding the burst, from May 2 to May 7 was examined. Table 5.1 shows the results of the Z_2^2 tests at the 282.805 s period detected by North et al. The most significant trial, resulting in a Z_2^2 of 7.13, corresponds to a probability of the distribution arising from random fluctuations of 13%. When the fact that the six trials were made is taken into consideration, this becomes even less significant. The energy spectrum of the emission modulated with the 282.805 S pulsar period must therefore cut-off before $\sim 4 \times 10^{14}$ eV.

5.2.2 LMC X-4

The first eight days of observing periods of the Large Magellanic Cloud by the UHURU satellite revealed three sources and possibly a fourth, variable source (Leong et al. 1971). The latter, seen on only one day, was confirmed in later UHURU

TABLE 5.1.

NUMBER OF FAST-TIMING DETECTORS TRIGGERED

	4-6	7-8	9-11
3 April - 13 May			
Number of events	125	41	35
Z_2^2 value	2.83	3.89	4.45
2 May - 7 May			
Number of events	16	6	8
Z_2^2 value	7.13	5.01	2.78

Results of the search for emission modulated with the Vela X-1 pulse period as measured by North et al. (1987). See text for details.

TABLE 5.2.

P	Z_{10}^2
0	23.98
1×10^{-9}	20.57
2×10^{-9}	33.51
2.75×10^{-9}	33.85
3×10^{-9}	33.80
4×10^{-9}	33.34
5×10^{-9}	32.04

Results of trial period derivatives added to the x-ray ephemeris of Mason et al. (1982) for events from the direction of 1822-37.1.

observations (Giacconi et al. 1972) and subsequently named LMC X-4. Photometric observations of the optical counterpart led to the discovery of a 1.4d periodic modulation (Chevalier and Ilovaisky 1977). This was subsequently confirmed in x-ray data (White et al. 1978). HEAO-1 data revealed that the x-ray flux was modulated with a 30.4d period (Lang et al. 1981). A 13.5s pulse period was discovered by the SAS-3 satellite, using data obtained during x-ray flares (Kelley et al. 1983). The 30.4d period was confirmed in optical photometric data by Ilovaisky et al. (1984) who interpreted it in terms of an x-ray heated, tilted, counter-rotating accretion disk.

LMC X-4 was first observed at UHE gamma-ray energies by Protheroe and Clay (1985a). Events were accepted within a 2.5° circle centred on the source. No age cut was used in this case, as the source could only be observed at large zenith angles. As the width of age distributions are found to increase with zenith angle, it was felt that the declination of the source would result in a significant overlap in the age distributions of cosmic-ray and gamma-ray showers.

A search for UHE gamma-rays modulated with the orbital period was performed over a range of periods centred on previously reported values. The Z_{10}^2 is used as it is powerful for narrow peaks in the phase distribution. These results are shown in Figure 5.5 and are not significant at even the 50% level for the optical and x-ray values of the period. This result does not directly contradict the earlier observation of Protheroe and Clay (1985a). The present data set is significantly shorter, and the variability

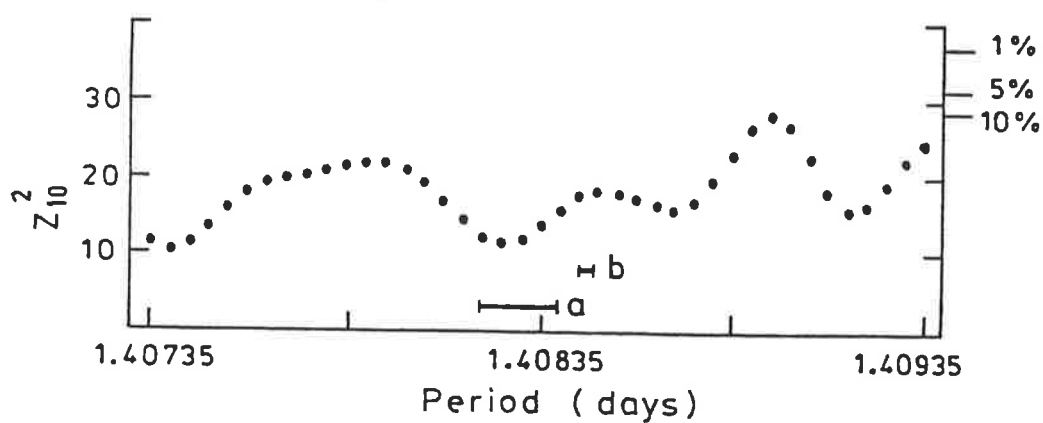


figure 5.5

Results of a period search performed on events from the direction of LMC X-4. Previous determinations of the orbital period by (a) Kelley et al. (1983) (X-ray) and (b) Ilovaisky et al. (1984) (optical) are shown.

of LMC X-4 at x-ray energies is well documented (e.g. Ilovaisky et al. 1984). Furthermore, as LMC X-4 is ~ 50 kpc away, gamma-rays of $E < 10^{15}$ eV are expected to be severely attenuated by interactions with the 2.7 K microwave background (Protheroe and Clay 1985a). The lower energy threshold of this experiment compared with that of the array during 1979-1981 and correspondingly higher background may conspire to hide any signal from LMC X-4.

Protheroe and Clay (1985b) also searched for the 30.4d periodicity in the 1979-1981 data set. Although the period 30.61 d exceeded the 1% critical value of Protheroe test, the period range of Ilovaisky et al. (1984) did not exceed the 10% critical value. The results of a similar period search with the present data are shown in Figure 5.6. The period 30.37 d is significant at the 2.3% level, and falls at the edge of the period range of Ilovaisky et al. (1984). However Exosat observations of LMC X-4 during 1983, when combined with earlier observations, give a period range which excludes 30.37 d (Pakull et al. 1985). The phase distribution at the 30.37 d period is shown in Figure 5.7. No significant peaks are evident in the distribution. Since no evidence for gamma-ray emission modulated with the 1.408 d period was found, this result is perhaps not surprising.

5.2.3 CIRCINUS X-1

Cir X-1 was first detected in rocket flights (Margon et al. 1971). Its binary nature was postulated by Jones et al. (1973) but it was not until 1976 that the orbital period of 16.59 d was discovered in x-ray data from the All-Sky Monitor (Kaluziński et al. 1976). This period has been confirmed by radio observations at

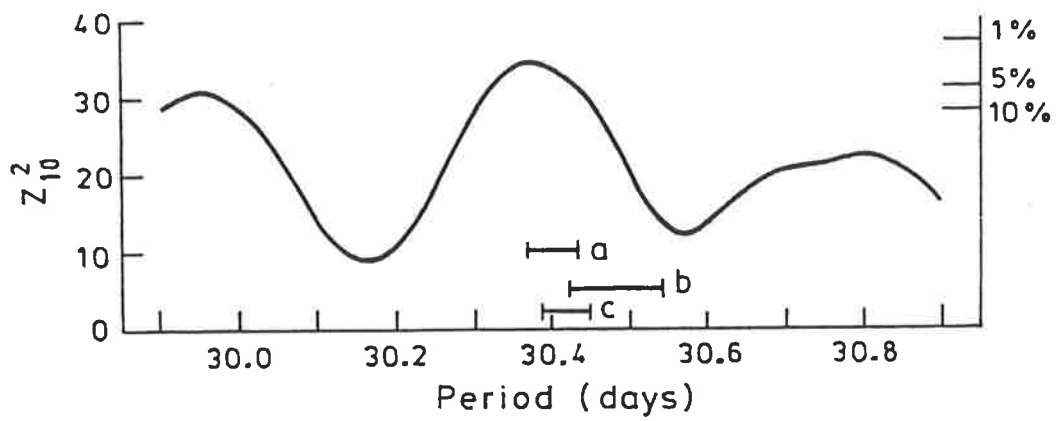


Figure 5.6. Results of a period search centred on the precession period of LMC X-4. Period determinations by (a) Leong et al. (1981) (x-ray) (b) Ilovaisky et al. (1984) (optical) and (c) Pakull et al (1985) (X-ray) are shown.

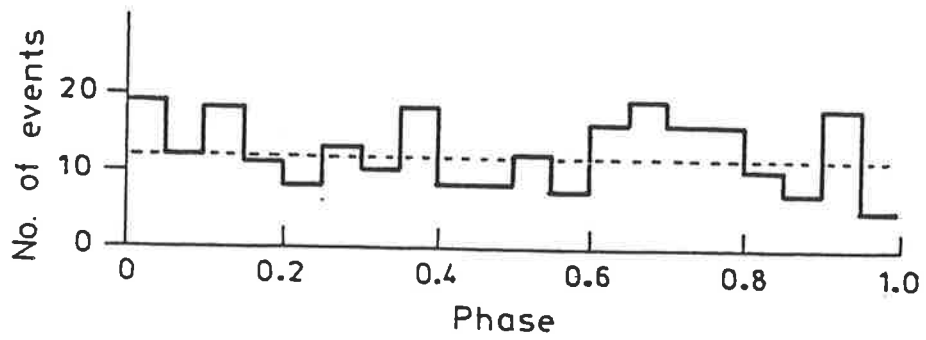


Figure 5.7 Phase distribution of events from the direction of LMC X-4 analysed with the most significant period from figure 5.6. No significant phase of emission is evident.

several wavelengths (Thomas et al. 1978). Cir X-1 is highly variable with significant variations on time-scales as short as several milliseconds (e.g. Dower et al. 1982). In this respect Cir X-1 is very similar to Cyg X-1, a possible black hole (e.g. Oda 1977). This led to the suggestion that the compact object of Cir X-1 may also be a black hole. However, the observation of type 1 x-ray bursts are interpreted as implying that the compact object is a neutron star (Tennant et al. 1986 a,b). Radio and optical identifications by Whelan et al. (1977) associated Cir X-1 with a massive binary system, however, more recent observations reveal that is a low mass system (Nicolson et al. 1980, Argue et al. 1984), which is also consistent with the observations of type 1 bursts (Tennant et al. 1986a). The distance to Cir X-1 has been established by radio observations to be 8-10 kpc (Goss and Mebold 1977). Radio observations also reveal that Cir X-1 is embedded in a nebula of steady radio emission (Haynes et al. 1986). This is not observed in most x-ray binaries. The extent of the nebula, estimated as several parsecs, is orders of magnitude greater than the scale of the binary stellar system. Haynes et al. suggest the nebula is the accumulation of energetic particles and plasma ejected during flaring activity.

Of the fourteen neutron star x-ray binary sources analysed by Protheroe and Clay (1985a) to search for UHE gamma-ray emission, only LMC X-4 exceeded the 1% critical value for the Protheroe test. Cir X-1 exceeded the 5% critical value, but as fourteen sources were examined this was not considered significant. A period search was performed on events triggering nine or more detectors from within 2.3° of the Cir X-1 using the Z_{10}^2 test. As Figure 5.8

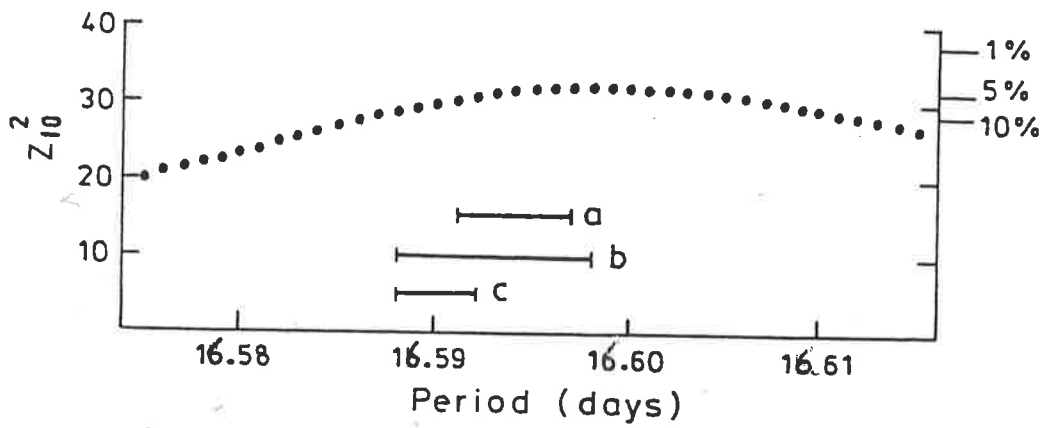


Figure 5.8 Results from a period search performed for events from the direction of Cir X-1. Periods obtained by (a) Kaluziński and Holt (refer to Thomas et al. 1978) (X-ray) (b) Haynes et al. (1978) - (radio 6 cm) (c) Haynes et al. (1978) (radio 2 cm) are shown for comparison.

illustrates, a period of 16.599 has a probability of 4.7% of being due to a random fluctuation, but is outside the range of periods determined at other wavelengths. The most recent x-ray period of Kaluziński and Holt (see Thomas et al. 1978) is significant at the 5.5% level.

In Figure 5.9 the phase distributions for both the 1979-1981 data set and the present data set are shown for the 16.594 d period. A significant peak at the same phase in both distributions would be strong evidence for the emission of UHE gamma-rays. The phase distribution of the 1979-1981 data set shows a peak at a phase of 0.85 ± 0.025 , however no corresponding peak is found in the more recent data. Thus no compelling evidence for emission is found.

5.2.4 CENTAURUS X-3

Centaurus X-3 was first observed in May 1967 during a rocket flight (Chodil et al. 1967). Pulsations with a 4.8 s period were discovered with the UHURU satellite (Giacconi et al. 1971). The 2.087 d orbital period was also found in UHURU data (Schreier et al. 1972). The stellar companion was optically identified as an O-type giant (Krzemski 1974), at a distance of 10 ± 1 kpc (Hutchings et al. 1979). The pulsation period of Cen X-3 was observed to decrease with a varying period derivative. This was interpreted as being due to the torques exerted on the neutron star by the accreting matter (e.g. Fabbiano and Schreier 1977). X-ray observations with the Vela satellite spanning seven years reveal

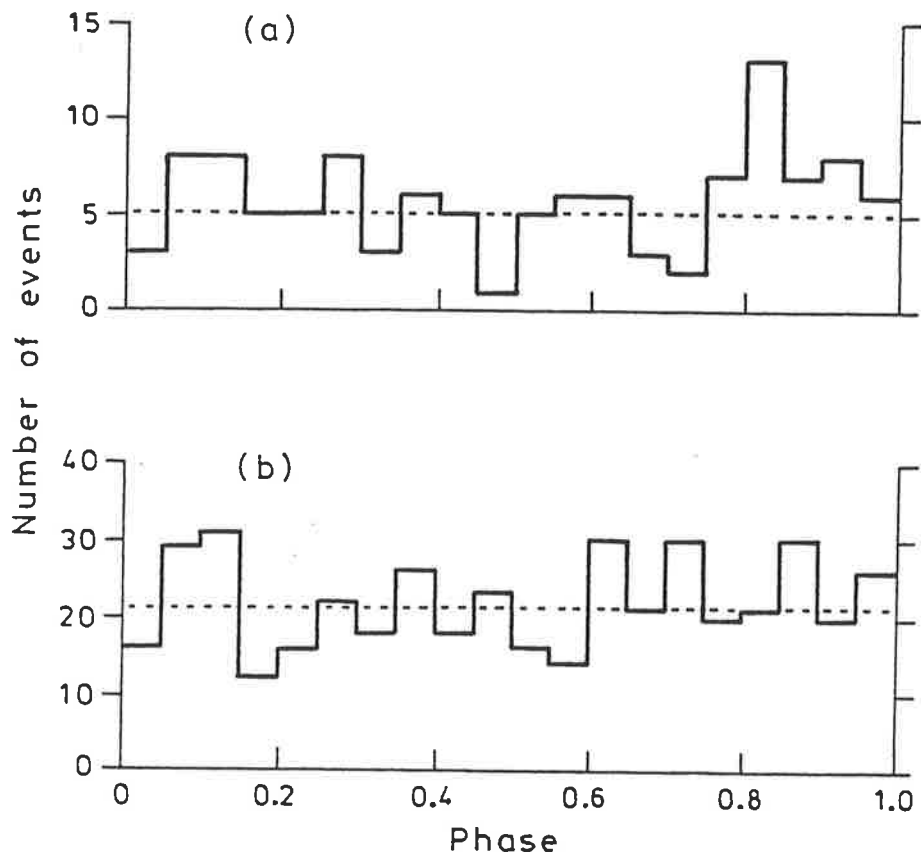


Figure 5.9

Phase distributions for events from the direction of Cir X-1, analysed using the ephemeris of Kaluziński and Holt (refer to Thomas et al. 1978).

(a) for the 1979-1981 data set

(b) for the present data set.

high-state activity which repeats on a characteristic but non-periodic timescale of 120-165 days (Priedhorsky and Terrell 1983). No evidence was found in the Vela data to support earlier claims of 26.6d or 43.0d precession periods.

Air shower data spanning five years from 1962 collected with the BASJE detector at Mt Chacaltaya was searched at the orbital period of Cen X-3. Showers were subjected to muon content and age cuts (see section 5.2.1.) which resulted in four events being accepted with a box 15° in right ascension and 10° in declination. The phase distribution revealed three events between phases 0.5-0.7. Although not statistically significant in itself, when coupled with the D.C. level the probability of the observation being due to a statistical fluctuation was claimed to be $\sim 10^{-3}$ (Suga et al. 1985).

As a result of this claimed detection by the BASJE collaboration (see also Suga et al. 1987), events from within 2.3° of Cen X-3 were examined. As the energy threshold of the Mt Chacaltaya array is $\sim 1 \times 10^{14}$ eV, two data sets from the present data were analysed: events triggering nine or more detectors, corresponding to an energy threshold of approximately 9×10^{14} eV and events triggering seven or eight detectors, with a threshold of $\sim 5 \times 10^{14}$ eV.

Figure 5.10 illustrates the results of period searches carried out on these two data sets. Neither is significant at the 5% level for the periods obtained at x-ray energies, and thus no evidence of emission of UHE gamma rays is found at these energies.

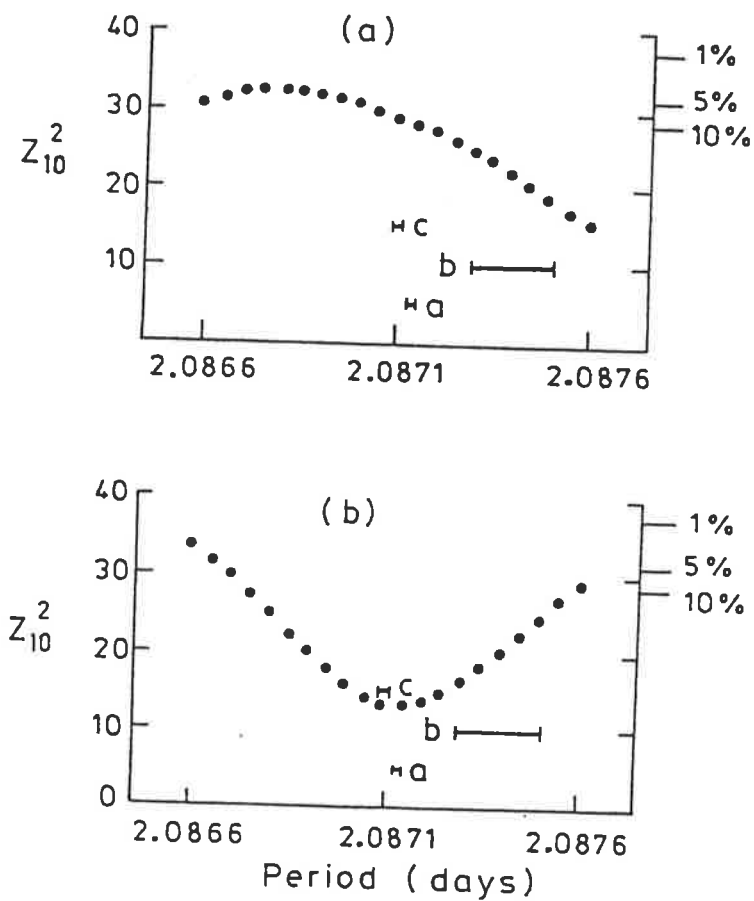


Figure 5.10 Period searches performed on events from the direction of Cen X-3 for events triggering (a) nine or more fast-timing detectors (b) seven or eight fast-timing detectors. Periods obtained by (a) Kelley et al. (1983) (X-ray) (b) Howe et al (1983) (X-ray) (c) Murakami et al. (1983) (X-ray) are shown.

5.2.5 SCORPIUS X-1

As mentioned in section 1.3.1 the first extra-solar x-ray source discovered was the strong source Sco X-1 (Giacconi et al. 1962). Sco X-1 was, with the exception of the Crab Nebula, the first stellar x-ray source identified in optical wavelengths. Sandage et al. (1966) found the companion star to be a red dwarf. The orbital period of Sco X-1 was first established by examining 1068 magnitudes obtained from blue plates taken between 1889 and 1974 (Gottlieb et al. 1975). The 0.787313 d period was confirmed by Cowley and Crampton (1975) and more recently by La Sala and Thorstensen (1985), both with optical observations. The orbital period has not been seen in x-ray observations (e.g. Priedhorsky and Holt 1987). This is assumed to be due to the high inclination of the system. The inclination of Sco X-1 is estimated to be $\sim 30^\circ$ (Crampton et al. 1976).

Observations of Sco X-1 have been made using an air shower array on Mt Chacaltaya. An excess of events was observed at phases 0.175 ± 0.025 of the orbital period during May 1986 (Inoue 1987). Data from the present experiment were examined to see if a similar excess was evident. Events from within 2.3° of Sco X-1 triggering (a) nine or more detectors and (b) seven or eight detectors were analysed with the same ephemeris as that used by Inoue. The resulting phase distributions are plotted in Figure 5.11. When subject to a Z_{10}^2 test the distributions have probabilities of being due to random fluctuations of 85% and 19% respectively.

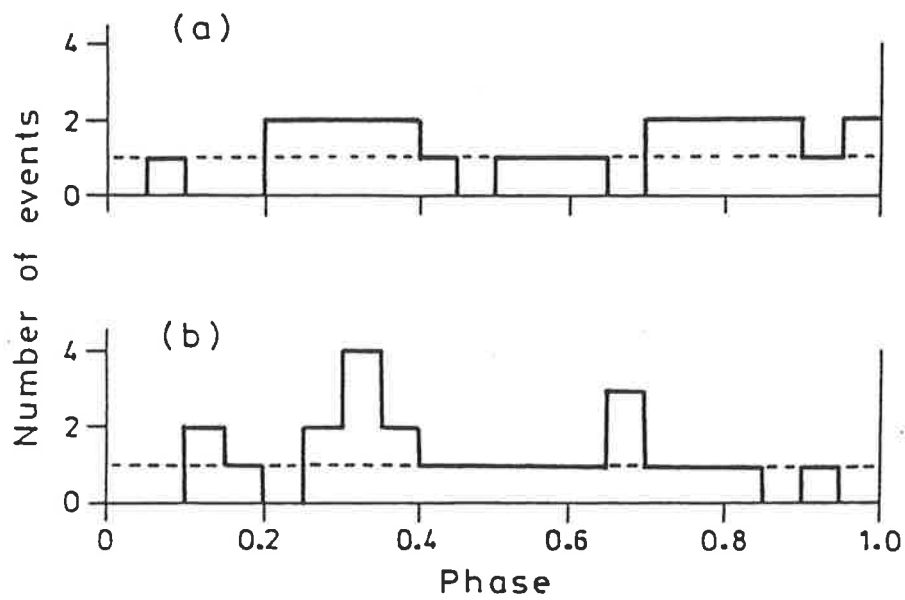


figure 5.11 Phase distributions for events from the direction of Sco X-1 triggering (a) nine or more fast-timing detectors, (b) seven eight fast-timing detectors, analysed with the ephemeris of Gottlieb et al (1975) (optical). Only events from May 1986 were used in this analysis (see text).

Neither of the distributions show any peak at the phase of the reported enhancement. The altitude and latitude of Mt Chacaltaya make the energy threshold for showers from the direction of Sco X-1 lower than that of Buckland Park. Also the Mt Chacaltaya data was subjected to muon and age cuts. The Buckland Park array was not operating between May 17 and May 26 1986, during which time several of the events were recorded at Mt Chacaltaya (Inoue 1987). The lack of observed x-ray variation at the orbital period is probably due to the fact that the accretion disk does not block the view of the neutron star from Earth. This would seem to require some form of particle beaming, such as proposed by Gorham and Learned (1986), to produce a flux of UHE gamma-rays at Earth.

5.2.6 1822-371

The first detection of 1822-371 was probably made during a rocket flight (Friedman et al. 1967), and its existence had been established by the time of the publication of the second UHURU catalogue (Giacconi et al. 1972). The optical counterpart of 1822-371 was discovered by Griffiths et al. (1978). The orbital period was detected at optical wavelengths (Mason et al. 1980, see also Charles et al. 1980) and confirmed by x-ray observations with the HEAO-1 and Einstein satellites (White et al. 1981). The x-ray light curve was empirically modelled by White and Holt (1982) using an accretion disk corona. This model was extended by Mason and Cordova (1982) to also explain the infrared, optical and ultraviolet emission from 1822-371. The model consists of an accretion disk with a large bulge at orbital phase 0.8, assumed to be due to the confluence of inflowing gas with the accretion disk,

and a second, smaller bulge at ~ 0.25 . The existence of such bulges is supported by three-dimensional calculations of stream-disk interactions (Livio et al. 1986). The accretion disk corona model is also successful in explaining observations of Cyg X-3 (Protheroe and Stanev 1987). 1822-37.1 is found to have many other properties similar to Cyg X-3 (White et al. 1981), making it a candidate for UHE gamma-ray emission.

A preliminary analysis of a search for UHE gamma-ray emission using the 1979-1981 ^{data} was presented by Ciampa et al. (1987). A more complete analysis, with and without an age cut is given in Figure 5.12. Theoretical arguments aside, an age cut is reasonable since 1822-37.1 is viewed at small zenith angles at Buckland Park. Neither distribution exceeds the 10% critical value of the Protheroe test. It is interesting to note, however, that the largest peak in the distributions corresponds to the position of the pre-bulge in the model of White and Holt (1982) illustrated in Figure 5.13. The significance of this peak is not as great in the phase distribution of the data with the age cut, as the adjacent bin has a negative variation from the mean of a similar magnitude.

A period search was performed on events triggering nine or more fast-timing detectors in the present data set. As illustrated in Figure 5.14, the peak of the distribution occurs at a period of 0.232114 d, just outside the range of published periods. The value of the Z_{10}^2 statistic for this period, 34.46, corresponds to a probability of the distribution arising from random fluctuations of 2.3%. The phase distribution of events at this period is plotted in Figure 5.15. Although it is apparent that there is a peak at

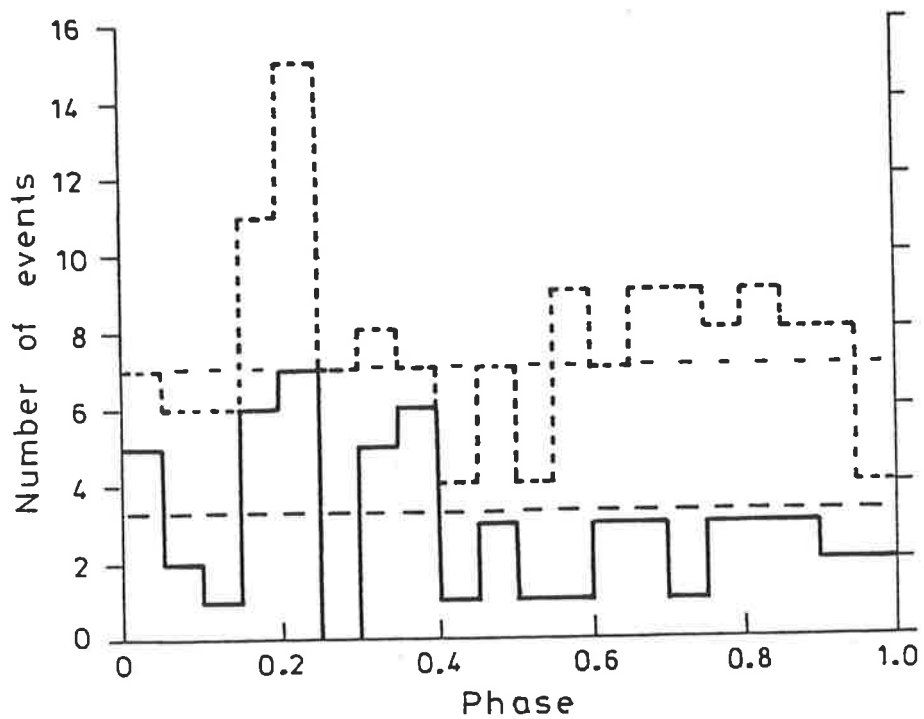


Figure 5.12 Full phase analysis of events from the direction of 1822-37.1 using the 1979-1981 data set, and the ephemeris of Mason et al. (1982) (x-ray). Full line corresponds to events with $s > 1.3$, large dashed line to background for these events. Small dashed-line is for events of all ages together with the background for these events.

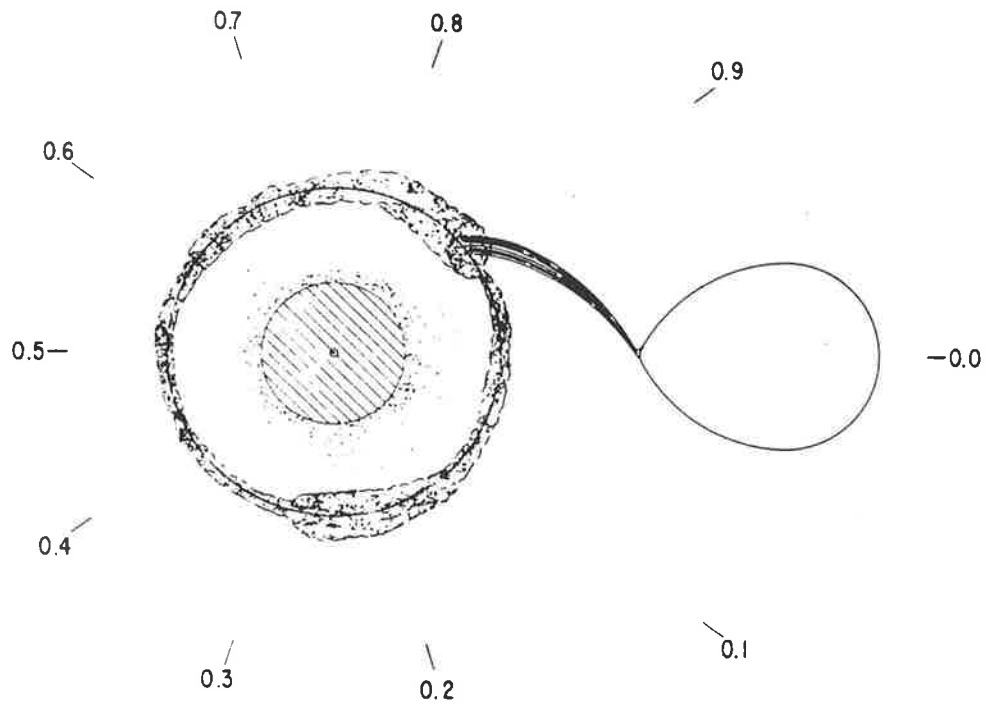


Figure 5.13 Idealized view of the possible appearance of the 1822-37.1 system. The hatched region represents the optically thick region of the accretion disk corona, and the dotted area represents the optically thin region. The binary phases are also indicated. (From White and Holt (1982)).

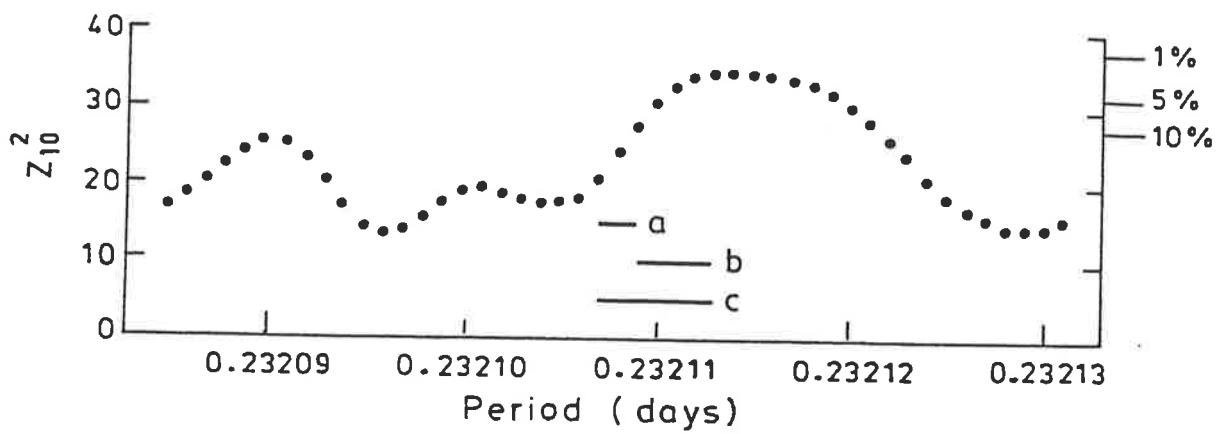


Figure 5.14 Results of a period search performed on events from the direction of 1822-37.1. Periods obtained by (a) Cowley et al (1982) (optical and X-ray) and Mason et al. (1982) (X-ray), (b) Mason et al. (1982) (optical), (c) White et al. (1981) (X-ray) are shown.

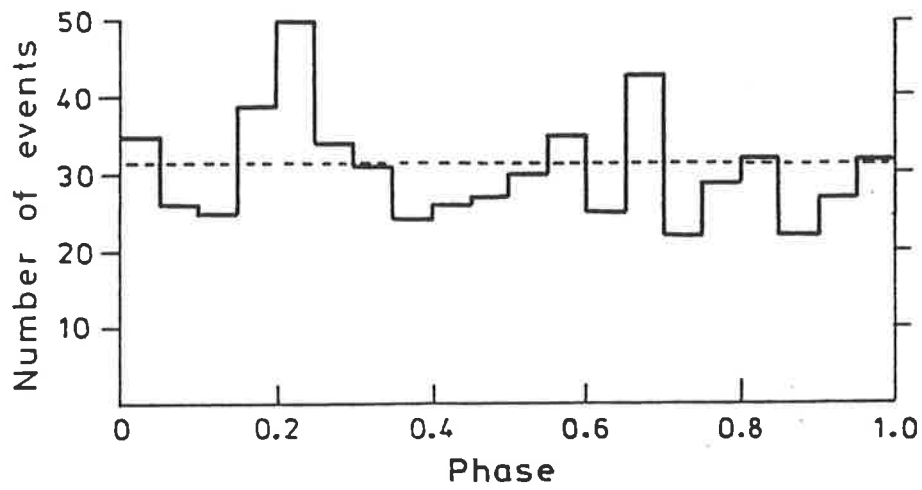


Figure 5.15 Phase distribution of events from the direction of 1822-37.1 with the most significant period from figure 5.14 (and the T_0 of Mason et al (1982) (X-ray)).

the phase 0.225 ± 0.025 - the same phase as the peak of Figure 5.12 - the two distributions are at mutually exclusive periods. Adopting the x-ray ephemeris of Mason et al. (1982), a range of period derivatives were trialled (table 5.2.). It is not surprising that the value 2.75×10^{-9} gives the most significant result as this corresponds to a period of 0.232114 d half-way through the present data set. Figure 5.16 shows the phase distribution obtained by adopting this period derivative. Although the value of the Z_{10}^2 statistic is similar, the peak of the distribution is no longer in accord with either the earlier data or the accretion disk corona model. No compelling evidence for the emission of UHE gamma-rays can thus be claimed.

5.3 SUMMARY

Six potential sources have been examined for evidence of ultra-high-energy gamma-ray emission during the two-year period June 1984 to June 1986. No positive signal has been found for any of the sources. Upper limits for the flux from these sources, calculated using the method of Protheroe (1984) are given in Table 5.3. Where two cuts have been applied to the data from a source, upper limits have been calculated for the two corresponding energy thresholds. Figure 5.17 shows the integral spectrum of Vela X-1 onto which has been added the upper limit obtained in this experiment.

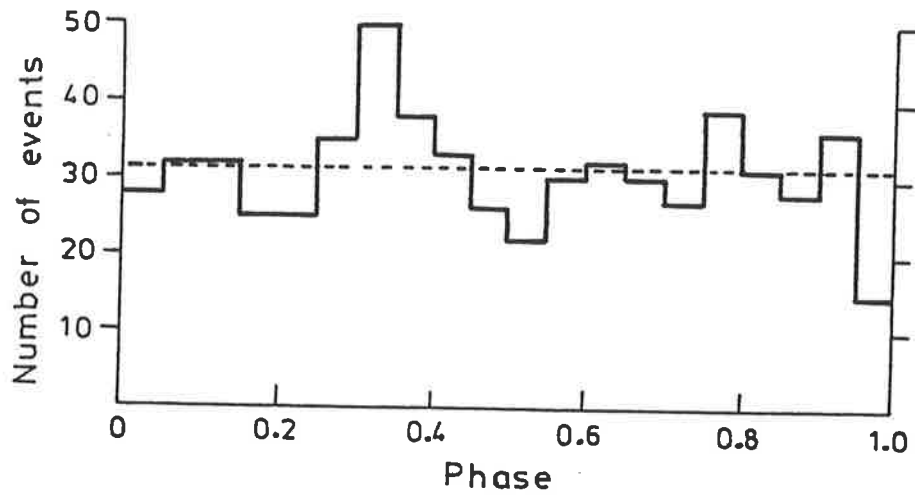


Figure 5.16 Phase distribution of events from the direction of 1822-37.1 analysed with the X-ray ephemeris of Mason et al (1982) with the addition of the most significant period derivative from Table 5.2.

SOURCE NAME	TYPE*	D (Kpc)	θ_c ($^{\circ}$)	α	β	N	N γ	Ref.	E _{TH}	** F γ	L	95% U.L. L (This data set)
0900-403 Vela X-1	1	1.4	10 $^{\circ}$ x10 $^{\circ}$ 2.0						(a)	1x10 ¹⁴	1.6x10 ⁻⁹	1.5x10 ³⁴
									(b)	8x10 ¹⁴	1.6x10 ⁻⁹	1.1x10 ³⁵
									(c)	3x10 ¹⁵	9.3x10 ⁻¹¹	2.2x10 ³⁴
0532-664 LMC X-4	1	50	2.5	0.015	556.7	535	38		(d)	9x10 ¹⁴	7.9x10 ⁻⁹	6.1x10 ³⁵
										8x10 ¹⁵	4.6x10 ¹¹	~ 10 ³⁸
1516-569 CIR X-1	2	10	2.3	0.043	423.4	439	57		(d)	5x10 ¹⁵	2.6x10 ⁻¹⁰	1.27 x 10 ³⁷
										2x10 ¹⁵	4.1 x 10 ⁻¹⁰	3.6x10 ³⁶
1119-603 CEN X-3	1	10	15 $^{\circ}$ x10 $^{\circ}$ 2.3						(a)	1x10 ¹⁴	1.8x10 ⁻⁹	1.0x10 ³⁶
									(d)	5x10 ¹⁵	1.2 x 10 ⁻¹⁰	6.1x10 ³⁶
										2x10 ¹⁵	3.7x10 ⁻¹⁰	3.3x10 ³⁶
1617-155 SCO X-1	2	0.7	2.3	0.043	803.9	815	69		(d)	7x10 ¹⁴	1.8x10 ⁻⁹	5.3 x 10 ³⁶
										4x10 ¹⁵	1.6x10 ⁻¹⁰	1.4x10 ³⁴
										1x10 ¹⁵	7.4x10 ⁻⁹	1.6x10 ³⁵
1822-371	2	2.5	2.1	0.043	628.9	614	44			9x10 ¹⁴	8.9x10 ⁻¹⁰	2.2x10 ³⁵
									(e)	3x10 ¹⁵	1.2x10 ⁻¹⁰	9.6x10 ³⁵
										142.2	153	36

- * 1) Massive system
2) Low mass system

(a) Suga et al. 1987;

(c) Protheroe et al. 1984;

(b) van der Walt et al. 1987;

(d) Protheroe et al. 1984

(e) Unpublished 1979-1981 data set.

Value for LMC X-4 has been corrected for cascading in 2.7K microwave background from this experiment.

** γ -ray flux is above the energy threshold, E_{TH}. Luminosity is per decade at 10¹⁵ eV assuming an E⁻² differential photon spectrum at the source.

Summary of results from this chapter. Upper Limits and subsequently derived intensities and luminosities from this experiment are given, as are results from previous experiments for comparison.

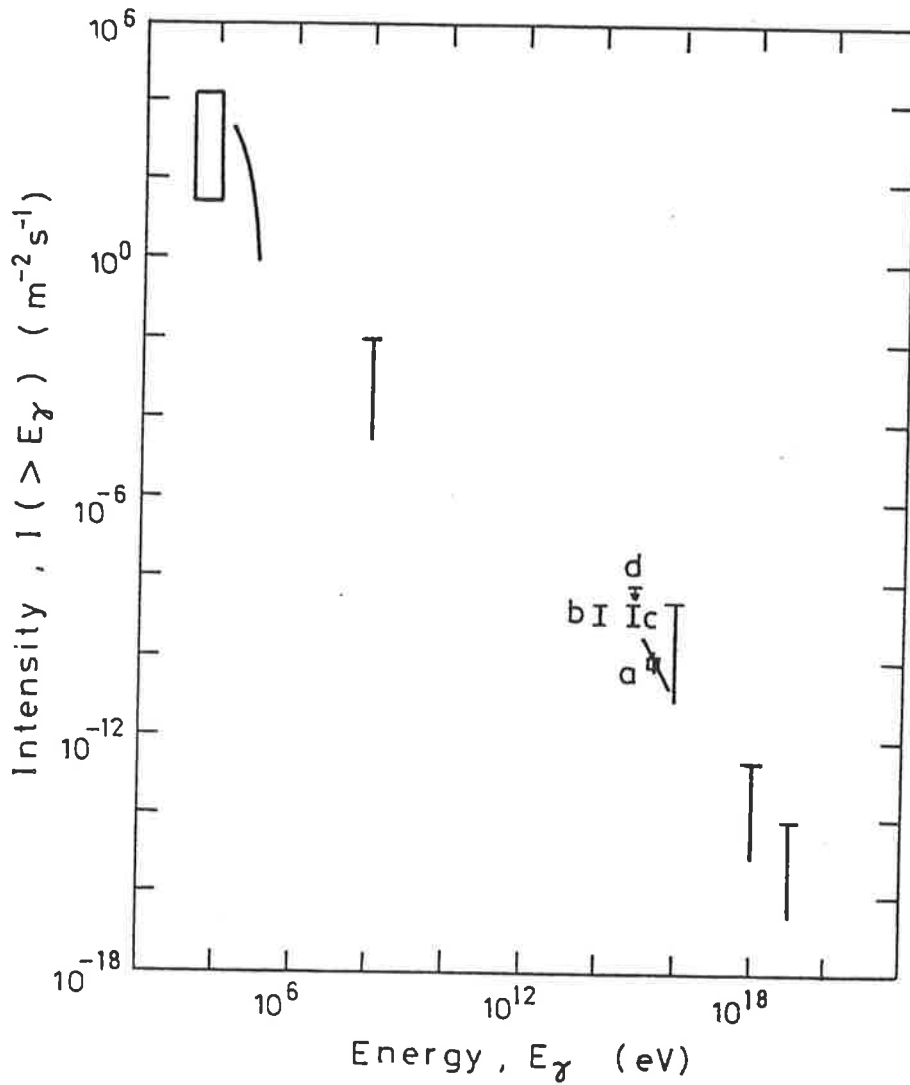


Figure 5.17

The integral spectrum of Vela X-1, adapted from Protheroe et al. (1984). The 100 MeV upper limit was obtained by the Cos B satellite (Swanenburg et al. 1981). The upper limits at 10^{16} , 10^{18} and 10^{19} eV were obtained from the data of Bray et al. (See Protheroe et al. (1984)). Values from the observations by (a) Protheroe et al. (1984.), (b) Suga et al. (1987) and (c) van der Walt et al. (1987) are shown, together with the upper limit obtained by this experiment (d).

CHAPTER 6

CONCLUSION

Ultra-high-energy gamma-ray astronomy is still in its infancy. Much remains to be learnt about gamma-ray initiated extensive air showers and the sources of ultra-high-energy gamma-rays. Six potential sources of ultra-high-energy gamma-rays were examined in this thesis. No compelling evidence for periodic modulation of extensive air shower arrival from the direction of any of these sources was found. The absence of any evidence of periodic ultra-high-energy gamma-ray emission is not necessarily in conflict with the previously reported detections of several of these sources.

The lack of any of periodicity in the x-ray emission from Sco X-1 illustrates that the inclination of the source is an important factor in determining whether any periodic modulation will be seen. It may seem that ultra-high-energy gamma-ray emission also depends on the inclination, or predilection, of the sources! However, other ultra-high-energy gamma-ray sources, most notably Cyg X-3, show variability in ultra-high-energy gamma-rays and at other wavelengths. Variability in the flux from ultra-high-energy gamma-ray sources is to be expected (e.g. Weekes 1985, Protheroe 1987b). It is interesting to note that in the case of Cyg X-3 the variability may have a 328 d periodicity (Neshpor and Zyskin 1986). It is possible that Vela X-1 also has a longer period modulation that has yet to be discovered.

During the author's candidature, a data set spanning two years has been collected. The size of the data set is over an order of magnitude larger than the previous data set recorded with the Buckland Park array, and there remains much useful analysis to be performed on this data. Other x-ray binary sources can be examined for evidence of ultra-high-energy gamma-ray emission, and the original purpose of infilling the array can be fulfilled with an anisotropy analysis of the present data. A full analysis of all events will allow the effect of an age cut in the analysis of events from potential ultra-high-energy gamma-ray sources to be examined. It is unfortunate that time did not allow such an analysis during my research.

APPENDIX A

The direction of an incident EAS is obtained from a least-squares fit of a plane to the shower front. This is iterated to include the variations from a horizontal plane of the detectors.

The fit is made by minimizing the function

$$\chi^2 = \sum_{i=1}^{11} \omega_i \left[\ell x_i + m y_i + (t_i - t_o) \right]^2 \quad (\text{A-1})$$

where

- x_i = x co-ordinate of the i th hut
- y_i = y co-ordinate of the i th hut
- t_i = relative observed time at i th hut
- t_o = timing offset
- ω_i = 1 if the detector was triggered
= 0 otherwise
- ℓ, m = direction cosines

As described in section 4.7, a timing offset is used so that the fitted shower front is not constrained to pass through any detector. The equation A-1 is minimized by taking partial derivatives

$$\begin{aligned} \frac{\partial \chi^2}{\partial \ell} &= 2 \sum \omega_i x_i \left[\ell x_i + m y_i + (t_i - t_o) \right]^2 \\ \frac{\partial \chi^2}{\partial m} &= 2 \sum \omega_i y_i \left[\ell x_i + m y_i + (t_i - t_o) \right]^2 \\ \frac{\partial \chi^2}{\partial t_o} &= - \sum \omega_i \left[\ell x_i + m y_i + (t_i - t_o) \right]^2 \end{aligned}$$

and setting these equal to zero:

$$\sum \omega_i l x_i^2 + \sum \omega_i m x_i y_i + \sum \omega_i (t_i - t_o) x_i = 0$$

$$\sum \omega_i l x_i y_i + \sum \omega_i m y_i^2 + \sum \omega_i (t_i - t_o) y_i = 0$$

$$\sum \omega_i l x_i + \sum \omega_i m y_i + \sum \omega_i (t_i - t_o) = 0$$

This is more conveniently represented in matrix form. If we let

$$XX = \sum \omega_i x_i^2$$

$$N = \sum \omega_i t_o$$

$$YY = \sum \omega_i y_i^2$$

$$XT = \sum \omega_i x_i t_i$$

$$XY = \sum \omega_i x_i y_i$$

$$YT = \sum \omega_i y_i t_i$$

$$X = \sum \omega_i x_i$$

$$T = \sum \omega_i t_i$$

$$Y = \sum \omega_i y_i$$

then

$$\begin{bmatrix} XX & XY & X \\ XY & YY & Y \\ X & Y & N \end{bmatrix} \begin{bmatrix} l \\ m \\ t_o \end{bmatrix} = \begin{bmatrix} XT \\ YT \\ T \end{bmatrix}$$

Simple matrix manipulation gives the result

$$l = (N.YY - Y^2) XT + (X.Y - XY.N) YT + (XY.Y - X.YY) T$$

$$m = (X.Y - XY.N) XT + (XX.N - X^2) YT + (XY.X - Y.XX) T$$

$$t_o = (XY.Y - X.YY) XT + (X.XY - XX.Y) YT + (XX.YY - XY^2) T$$

The third direction cosine is

$$n = \sqrt{1 - (l^2 + m^2)}$$

and the zenith and azimuth angles are

$$\theta = \tan^{-1} \left(\frac{\sqrt{1 - n^2}}{n} \right)$$

and

$$\phi = 90 - \tan^{-1} \left(\frac{m}{l} \right)$$

Once θ and ϕ are known, the values of t_i are adjusted to include the small differences arising from the fact that the detectors do not all lie in a plane. New values of θ and ϕ are then calculated. This process is iterated until convergence is reached.

REFERENCES

The abbreviation ICRC represents International Cosmic Ray Conference. Papers with more than seven authors are abbreviated to et al.

- Allan, H.R., 1971 Prog. Elem. Part. and Cosmic Ray Phys. 10, 170.
- Allkofer, O.C., Carstensen, K., Dau, W.D. and Jokisch, H. 1975 J. Phys. G: Nucl. Phys. 1, L151.
- Alvarez, L.W. and Compton, A.H. 1933 Phys. Rev. 43, 835.
- Anderson, C.D. 1933 Phys. Rev. 43, 368.
- Argue, A.N., Jauncey, D.L., Morabito, D.P. and Preston, R.A. 1984 Mon. Not. R. Ast. Soc. 209, 11P.
- Armitage, R., Blake, P.R., Nash, W.F., Saltmarsh, C.G., Sephton, A.J., Shelley, C.C. and Strutt, R.B. 1987 J. Phys. G: Nucl. Phys. 13, 707.
- Astley, S.M., Cunningham, G., Lloyd-Evans, J., Reid, R.J.O. and Watson, A.A. 1981 Proc. 17th ICRC (Paris) 2, 156.
- Auger, P., Maze, R. and Grivet-Mayer, T. 1938 C. R. Acad. Sci. (Paris) 206, 1721.
- Auriemma, G., Maiani, L. and Petrarca, S. 1985 Phys. Lett. 164B, 179.
- Baltrusaitis, R.M. et al. 1984 Phys. Rev. Lett. 52, 1380.
- Baltrusaitis, R.M. et al. 1985 Phys. Rev. Lett. 54, 1875.
- Barnhill, M.V., Gaisser, T.K., Stanev, T. and Halzen, F. 1985 Nature 317, 409.
- Battistoni, G. et al. 1985 Phys. Lett. 155B, 465.
- Bauer, T.H., Spital, R.D., Yennie, D.R. and Pipkin, F.M. 1978 Rev. Mod. Phys. 50, 261.
- Baym, G., Kolb, E.W., McLerran, L., Walker, T.P. and Jaffe, R.L. 1985 Phys. Lett. 160B, 181.
- Benecke, J. et al. 1969 Phys. Rev. 188, 2159.
- Berger, C.H. et al. 1986 Phys. Lett. 174B, 118.
- Berezinskii, V.S. and Ioffe, B.L. 1986 Sov. Phys. J.E.T.P. 63, 920.

- Bhat, P.N. et al. 1985 Proc. Workshop on Techniques in Ultra High Energy Gamma Ray Astronomy (La Jolla) ed. R.J. Protheroe and S.A. Stephens (University of Adelaide) p.1.
- Blackett, P.M.S. and Occhialini, G.P.S. 1933 Proc. R. Soc. A 139, 699.
- Bloomer, S.D., Linsley, J. and Watson, A.A. 1987 Proc. 20th ICRC (Moscow) 2, 445.
- Bower, A.J. et al. 1981 Proc. 17th ICRC (Paris) 9, 166.
- Bradt, H.V.D. and McClintok, J.E. 1983 Ann. Rev. Astron. Astroph. 21, 13.
- Braun, O. and Sitte, K. 1965 Proc. 9th ICRC (London) 2, 712.
- Buccheri, R. 1985 Proc. Workshop on Techniques in Ultra High Energy Gamma Ray Astronomy (La Jolla) ed. R.J. Protheroe and S.A. Stephens (University of Adelaide) p.98.
- Capdevielle, J.N. and Gawin, J. 1982 J. Phys. G: Nucl. Phys. 8, 1317.
- Cassé, M. and Paul, J. 1980 Ap. J. 237, 236.
- Chadwick, P.M. et al. 1985 Nature 318, 642.
- Chadwick, P.M., Dipper, N.A., Douthwaite, J.C., McComb, T.J.L., Orford, K.J. and Turver, K.E. 1987 in "Very High Energy Gamma Ray Astronomy" ed. K.E. Turver (D. Reidel) p. 115.
- Charles, P., Thorstensen, J.R. and Barr, P. 1980 Ap. J. 241, 1148.
- Chevalier, C. and Ilovaisky, S.A. 1977 Astron. Astroph. 59, L9.
- Chodil, G. et al. 1967 Phys. Rev. Lett. 19, 681.
- Chudakov, A.E., Zatsepin, V.I., Nesterova, N.M. and Dadykin, V.L. 1962 J. Phys. Soc. Japan 17, 106.
- Ciampa, D. and Clay, R.W. 1987 J. Phys. G: Nucl. Phys. (submitted).
- Ciampa, D., Clay, R.W., Corani, C.L., Edwards, P.G., Patterson J.R., and Protheroe, R.J. 1987 in "Very High Energy Gamma Ray Astronomy" ed. K.E. Turver (D. Reidel) p. 275
- Ciampa, D., Clay, R.W., Corani, C.L., Edwards, P.G. and Patterson, J.R. 1986 Proc. Ast. Soc. Aust. 6, 335.
- Clay, J. 1927 Proc. Roy. Acad. of Amsterdam 30, 1115.

- Clay, R.W. 1985a Proc. 19th ICRC (La Jolla) 9, 357;
1985b Private Communication,
1987 Aust. J. Phys. 40, 423.
- Clay, R.W. et al. 1985 Proc. 19th ICRC (La Jolla) 3, 414.
- Clay, R.W. and Ciampa, D. 1986 Aust. J. Phys. J. 39, 93.
- Clay, R.W. and Gregory, A.G. 1978 Nucl. Instr. Meth. 153, 467.
- Clay, R.W. and Gerhardy P.R. 1982 Aust. J. Phys. 35, 59.
- Corani, C.L. 1986 M.Sc. Thesis, University of Adelaide.
- Cowley, A.P., Crampton, D. and Hutchings, J.B. 1982, Ap. J. 255, 296
- Cowley, A.P. and Crampton D. 1975 Ap. J. 201, L65.
- Craig, M.A.B., Orford, K.J., Turver, K.E. and Weekes, T.C. 1981
Proc. 17th ICRC (Paris) 1, 3.
- Crampton, D., Cowley, A.P., Hutchings, J.B. and Kaat, C. 1976
Ap. J. 207, 907.
- Crookes, I.N. and Rastin, B.C. 1971 Proc. 12th ICRC (Hobart)
4, 1325.
- Crouch, P.C., Gerhardy, P.R., Patterson, J.R., Clay, R.W. and
Gregory, A.G. 1981 Nucl. Instr. Meth. 179, 467.
- Cunningham, G., Lloyd-Evans, J., Reid, R.J.O. and Watson, A.A.
1983 Proc. 18th ICRC (Bangalore) 2, 157.
- Dawson, B.R. 1985 Ph.D. Thesis, University of Adelaide.
- Dawson, B.R., Clay, R.W., Edwards, P.G. and Prescott, J.R. 1986
Il Nuovo Cimento 9C, 1125.
- De Beer, J.F., Holyoak, B., Wdowczyk, J. and Wolfendale, A.W.
1966 Proc. Phys. Soc. 89, 567.
- Deeter, J.E., Boynton, P.E., Lamb, F.K. and Zylstra, G. 1987
Ap. J. 314, 634.
- Dixon, H.E., Turver, K.E. and Waddington, C.J. 1974 Proc. R.
Soc. Lond. A 339, 157.
- Dower, R.G., Bradt, H.V. and Morgan, E.H. 1982 Ap. J. 261, 228.
- Dzikowski, T., Gawin, J., Grochalska, B. and Wdowczyk, J. 1983
J. Phys. G: Nucl. Phys. 9, 459.
- Edwards, P.G., Protheroe, R.J. and Rawinski, E. 1985 J. Phys.
G: Nucl. Phys. 11, L101.

- Efimov, N.N., Mikhailov, A.A. and Pravdin, M.I. 1983 Proc. 18th ICRC (Bangalore) 2, 149.
- Eichler, D. and Vestrand, W.T. 1984 Nature 307, 613.
- Eichten, E. et al. 1984. Rev. Mod. Phys. 56, 579.
- Elbert, J.W. and Gaisser, T.K. 1979 Proc. 16th ICRC (Kyoto) 8, 42.
- Engelman, J.J. et al. 1985 Astron. Astroph. 148, 12.
- Fabbiano, G. and Schreier, E.J. 1977 Ap. J. 214, 235.
- Fenyves, E.J. 1985 Proc. Workshop on Techniques in Ultra High Energy Gamma Ray Astronomy (La Jolla) ed. R.J. Protheroe and S.A. Stephens (University of Adelaide) p. 124.
- Fermi, E. 1951 Phys. Rev. 81, 683.
- Feynman, R.P. 1969 Phys. Rev. Lett. 23, 1415.
- Firkowski, R., Gawin, J., Zawadski, A. and Maze, R. 1961 J. Phys. Soc. 17A, 123.
- Friedman, H., Byram, E.T. and Chubb, T.A. 1967 Science 156, 374.
- Fowler, P.H., Walker, R.N.F., Mashedor, M.R.W., Moses, R.T., Worley, A. and Gay, A.M. 1987 Ap. J. 314, 739.
- Gaisser, T.K., Protheroe, R.J. and Stanev, T. 1983 Proc. 18th ICRC (Bangalore) 5, 174.
- Gawin, J., Maze, R., Wdowczyk, J. and Zawadski, A. 1968 Can. J. Phys. 46, S72.
- Gerhardy, P.R. 1983 Ph. D. Thesis, University of Adelaide.
- Gerhardy, P.R. and Clay, R.W. 1983 J. Phys. G: Nucl. Phys. 9, 1279.
- Giacconi, R., Gursky, H., Kellogg, E., Schreier, E. and Tananbaum, H. 1971 Ap. J. Lett. 167, L67.
- Giacconi, R., Murray, S., Gursky, H., Kellogg, E., Schreier, E. and Tananbaum, H. 1972 Ap. J. 178, 281.
- Giacconi, R. et al. 1962 Phys. Rev. Lett. 9, 439.
- Gorham, P.W. and Learned, J. 1986 Nature 323, 422.
- Gottlieb, E.W., Wright E.L. and Liller, W. 1975 Ap. J. 195, L33.
- Goss, W.M. and Mebold, U. 1977 Mon. Not. R. Ast. Soc. 181, 255.

- Greisen, K. 1956 Prog. Cosmic Ray Phys. 3, 1;
1960 Ann. Rev. Nucl. Sci. 10, 63;
1966 Phys. Rev. Lett. 16, 748.
- Griffiths, R.E. et al. 1978 Nature 276, 247.
- Grindlay, J.E. 1971 Smithsonian Ap. Obs. Spec. Rep. No. 334.
- Grindlay, J.E., Helmken, H.F., Hanbury-Brown, R., Davis, J. and Allen L.R. 1975 Ap. J. 201, 82.
- Hara, T. et al. 1983 Proc. 18th ICRC (Bangalore) 11, 281.
- Hartman, R.C., Kniffen, D.A., Thompson, D.J., Fichtel, C.E., Ogelman, H.B., Tumer, T. and Ozel, M.E. 1979 Ap. J. 230, 597.
- Hayakawa, S. 1969; Cosmic Ray Physics, Wiley-Interscience, New York, 1969
1981 Sp. Sci. Rev. 29, 221.
- Hayashida, N., Ishikawa, F., Kamata, K., Kifune, T., Nagano, M. and Tan, Y.H. 1981 Proc. 17th ICRC (Paris) 9, 9.
- Haynes, R.F. et al. 1978 Mon. Not R. Ast. Soc. 185, 661;
1986 Nature 324, 233.
- Hess, V.F. 1912 Physik. Zeitschr. 13, 1804.
- Hill, C.T. and Schramm D.N., 1984 Phys. Rev. D 31, 564.
- Hillas, A.M. 1975 Phys. Lett. 20C, 59;
1979 Proc. 16th ICRC (Kyoto) 6, 13;
1981 Proc. 17th ICRC (Paris) 13, 69;
1984a Nature 312, 50;
1984b Ann. Rev. Astron. Astroph. 22, 425;
1985 Proc. 19th ICRC (La Jolla) 3, 445;
1987a Proc. 20th ICRC (Moscow) 2, 362;
1987b Proc. 20th ICRC (Moscow) 6, 432.
- Hillas, A.M. and Lapikens, J. 1977 Proc. 15th ICRC (Plovdiv) 8, 460.
- Hiltner, W.A., Werner, J. and Osmer, P. 1972 Ap. J. 175, L19.
- Ho, C. and Arons, J. 1987 Ap. J. 314, 619.
- Hutchings, J.B., Cowley, A.P., Crampton, D., van Paradijs, J. and White, N.E. 1979 Ap. J. 229, 1079.
- Ilovaisky, S.A., Chevalier, G., Motch, C., Pakull, M., von Paradijs, J. and Lub, J. 1984 Astron. Astroph. 140, 251.
- Inoue, N. 1987 Private Communications
- Johnson, T.H. 1933 Phys. Rev. 43, 834.

- Jones, C., Forman, W., Tananbaum, H., Schreier, E., Gursky, H., Kellogg, E. and Giacconi, R. 1973 Ap. J. 181, L43.
- Jones, L.W. 1985 Proc. 19th ICRC (La Jolla) 9, 323.
- Joss, P.C. and Rappaport, S.A. 1984 Ann. Rev. Astron. Astroph. 22, 537.
- Kaluzienski, L.J., Holt, S.S., Boldt, E.A. and Serlemitsos, P.J. 1976, Ap. J. 208, L71.
- Kalmykov, N.N., Fomin, Y.A. and Khristiansen, G.B. 1973 Proc. 13th ICRC (Denver) 4, 2633.
- Kamata, K. et al. 1968 Can. J. Phys. 46, S72.
- Karakula, S., Osborne, J.L. and Wdowczyk, J. 1974 J. Phys. A 7, 437.
- Karakula, S. and Wdowczyk, J. 1963 Acta Phys. Pol. 24, 231.
- Kelley, R.L., Jernigan, J.G., Levine, A., Petro, L.D. and Rappaport, S. 1983 Ap. J. 264, 568.
- Kifune, T. et al. 1986 Ap. J. 301, 230.
- Kolhörster, W., Matthes, I. and Webber, E. 1938 Naturwiss. 26, 576.
- Kondo, Y., van Flandern, T.C. and Wolff, D.L. 1983 Ap. J. 273, 716.
- Kraushaar, W.L., Clark, G.W., Gamire, G.P., Helmken, H., Higbie, P. and Agogino, M 1965 Ap. J. 141, 845.
- Krzemski, W. 1974 Ap. J. 192, L135.
- Kuhlmann, J.D. and Clay, R.W. 1981 Proc. 17th ICRC (Paris) 6, 96.
- La Sala, J. and Thorstensen, J.R. 1985 Astron. J. 90, 2077.
- Lagage, P.O. and Cesarsky, C.J. 1983 Astron. Astroph. 125, 249.
- Lang, F.L. et al. 1981 Ap. J. 246, L21.
- Leong, C., Kellogg, E., Gursky, H., Tananbaum, H. and Giacconi, R. 1971 Ap. J. Lett. 170, L67.
- Liebing, D.F., Clay, R.W., Gregory, A.G., Patterson, J.R., Prescott, J.R. and Thornton, G.J. 1981 Proc. 17th ICRC (Paris) 6, 90.

- Linsley, J. 1963 Phys. Rev. Lett. 10, 146;
1983 Proc. 18th ICRC (Bangalore) 12, 135;
1985 Proc. 19th ICRC (La Jolla) 9, 475;
1987 Proc. 20th ICRC (Moscow) 2, 442.
- Livio, M., Soker, N. and Dgani, R. 1986 Ap. J. Phys. 305, 267.
- Lloyd-Evans, J., Coy, R.N., Lambert, A., Lapikens, J., Patel, M., Reid, R.J.O. and Watson, A.A. 1983 Nature 305, 784.
- Longair, M.S. 1981 "High Energy Astrophysics" (Cambridge University Press).
- Margon, B., Lampton, M., Bowyer, S. and Cruddace, R. 1971 Ap. J. 169, L23.
- Marshak, M.L. et al. 1985a Phys. Rev. Lett. 54, 2079;
1985b Phys. Rev. Lett. 55, 1965.
- Mason, K.O. and Cordova, F.A. 1982 Ap. J. 262, 253.
- Mason, K.O., Middleditch, J., Nelson, J.E., White, N.E., Seitzer, P., Tuohy, I.R. and Hunt, L.K. 1980 Ap. J. 242, L109.
- Mason, K.O., Murdin, P.G., Tuohy, I.R., Seitzer, P. and Branduardi-Raymont, G. 1982 Mon. Not. R. Ast. Soc. 200, 793.
- Maze, R., Wdowczyk, J., Wolfendale, A.W. and Zawadski, A. 1969 Phys. Rev. Lett. 22, 899.
- Maze, R. and Zawadski, A. 1960 Nuovo Cimento 17, 625.
- McClintock, J.E. et al. 1976 Ap. J. 206, L99.
- McComb, T.J.L., Protheroe, R.J. and Turver, K.E. 1979 J Phys. G: Nucl. Phys. 5, 1613.
- Meyer, J-P. 1985 Proc. 19th ICRC (La Jolla) 9, 141.
- Morrison, P. 1958 Nuovo Cimento 7, 858.
- Neshpor, Y.I. and Zyskin, Y.L. 1986 Soviet Astron. Lett. 12, 189.
- Nicolson, G.D., Feast, M.W. and Glass, I.S. 1980 Mon. Not. R. Ast. Soc. 191, 293.
- Nikolsky, S.I., Stamenov, J.N. and Ushev, S.Z. 1987 J. Phys. G: Nucl. Phys. 13, 883.
- Nishimura, J. and Kamata, K. 1951 Prog. Theor. Phys. 6, 628.

- North, A.R., Raubenheimer, B.C., De Jager, O.C., Van Tonder
A.J. and Van Urk, G. 1987 Nature 326, 567.
- Oda, M. 1977 Sp. Sci. Rev. 20, 757.
- Ostriker, J.P. and Gunn, J.E. 1969 Ap. J. 157, 1395.
- Oyama, Y. et al. 1986 Phys. Rev. Lett. 56, 991.
- Pakull, M., Brunner, H., Pietsch, W. Staubert, A., Beuermann,
K., van der Klis, M. and Bonnet-Bidaud, J.M. 1985 Sp. Sci
Rev. 40, 379.
- Penzias, A.A. and Wilson, R.W. 1965 Ap. J. 142, 419.
- Perkins, D.H. 1972 "Introduction to High Energy Physics".
(Addison-Wesley)
- Peters, B. 1961 Nuovo Cimento 22, 800.
- Prescott, J.R., Clay, R.W., Corani, C.L., Dawson, B.R.,
Gregory, A.G. and Patterson, J.R. 1983 Proc. 18th ICRC
(Bangalore) 6, 257.
- Priedhorsky, W.C. and Terrell, J. 1983 Ap. J. 273, 709.
- Priedhorsky, W.C. and Holt, J.J. 1987 Ap. J. Phys. 312, 743.
- Protheroe, R.J. 1984 Astr. Expr. 1, 33;
1985 Astr. Expr. 1, 137;
1987a in "Very High Energy Gamma Ray Astronomy"
ed. K.E. Turver (D. Reidel) p.91;
1987b Proc. 20th ICRC (Moscow) Rapporteur Paper
(in press);
1987c Private Communication.
- Protheroe, R.J. and Clay, R.W.
1984 Proc. Ast. Soc. Aust. 5, 586;
1985a Nature 315, 205;
1985b Proc. 19th ICRC (La Jolla) 1, 247.
- Protheroe, R.J., Clay, R.W. and Gerhardy, P.R. 1984 Ap. J. 280,
L47.
- Protheroe, R.J. and Patterson, J.R. 1984 J. Phys. G: Nucl.
Phys. 10, 841.
- Protheroe, R.J. and Stanev, T. 1987 Nature 328, 136.
- Ramana Murthy, P.V. 1987 in "Very High Energy Gamma Ray
Astronomy" ed. K.E. Turver (D. Reidel) p. 39.
- Rossi, B. 1933 Z. Phys. 82, 151.
- Rossi, B. and Greisen, K. 1941 Rev. Mod. Phys. 13, 240.

- Samorski, M. and Stamm, W.
1983a Ap. J. 268, L17;
1983b Proc. 18th ICRC (Bangalore) 11, 244.
- Sandage, A.R. et al. 1966 Ap. J. Phys. 146, 316.
- Schreier, E., Levinson, R., Gursky, H., Kellogg, E., Tananbaum, H., and Giacconi, R. 1972 Ap. J. Lett. 172, L79.
- Simpson, J.A. 1983 in "Composition and Origin of Cosmic Rays" ed. M.M. Shapiro (D. Reidel) p. 1.
- Skobelzyn, D. 1929 Z. Phys. 54, 686.
- Stanev, T., Gaisser T.K, and Halzen F. 1985 Phys. Rev. D. 32, 1244.
- Stenger, V.J. 1985 Nature 317, 411.
- Strong, A.W., Wdowczyk, J. and Wolfendale, A.W. 1974 J. Phys. A 7, 1489.
- Suga, K. et al. 1985 Proc. Workshop on Techniques in Ultra High Energy Gamma Ray Astronomy (La Jolla) eds. R.J. Protheroe and S.A. Stephens (University of Adelaide) p.48;
1987 Proc. 20th ICRC (Moscow) 1, 277.
- Swanenburg, B.N. et al. 1981 Ap. J. Lett. 243, L69.
- Tennant, A.F., Fabian, A.C. and Shafer, R.A.
1986a Mon. Not. R. Ast. Soc. 219, 871;
1986b Mon. Not. R. Ast. Soc. 221, 27p.
- Thomas, R.M., Duldig, M.L., Haynes, R.F. and Murdin, P. 1978 Mon. Not. R. Ast. Soc. 185, 29P.
- Thornton, G.J. and Clay, R.W.
1979 Phys. Rev. Lett. 43, 1622 (and Errata Phys. Rev. Lett. 45, 1463);
1981 Phys. Rev. D 23, 2090.
- Tomaszewski, A. and Wdowczyk, J. 1975 Proc. 14th ICRC (Munich) 8, 2899.
- Ulmer, M.P., Baity, W.A., Wheaton, W.A. and Peterson, L.W. 1972 Ap. J. 178, L121.
- van der Walt, D.J., Raubenheimer, B.C., De Jager, O.C., North, A.R., van Urk, G. and De Villiers, E.J. 1987 Proc. 20th ICRC (Moscow) 1, 303.
- Watson, A.A. 1984 Advances in Space Science ed. L. Koch-Miramond and M.A. Lee 4, 35;
1985 Proc. 19th ICRC (La Jolla) 9, 111.
- Wdowczyk, J. 1965 Proc. 9th ICRC (London) 2, 691.

- Wdowczyk, J. and Wolfendale, A.W.
1983 Nature 305, 609;
1984 J. Phys. G: Nucl. Phys. 10, 1453;
1987 J. Phys. G: Nucl. Phys. 13, 411.
- Weekes, T.C. 1985 in "New Particles 1985" eds. V. Barger, D. Cline and F. Halzen (World Scientific) p. 288.
- Whelan, J.A. et al. 1977 Mon. Not. R. Ast. Soc. 181, 254.
- White, G.M. and Prescott, J.R. 1968 Can. J. Phys. 46, S287.
- White, N.E. 1978 Nature 271, 38.
- White, N.E., Becker, R.H., Boldt, E.A., Holt, S.S., Serlemitsos, P.J. and Swank, J.H. 1981 Ap. J. 247, 994.
- White, N.E. and Holt, S.S. 1982 Ap. J. 257, 318.
- Winn, M.W., Ulrichs, J., Peak, L.S., McCusker, C.B.A. and Horton, L. 1986 J. Phys. G: Nucl. Phys. 12, 653.
- Wrotniak, J.A. and Yodh, G.B. 1985 Proc. 19th ICRC (La Jolla) 6, 56.
- Yen, E. 1974 Phys. Rev. D 10, 836.
- Yodh, G.B., Pal, Y. and Trefil, J.S. 1972 Phys. Rev. Lett. 28, 1005.
- Zatsepin, G.T. and Kuzmin, V.A. 1966 Sov. Phys. J.E.T.P. Lett. 4, 78.